



Spatio–Angular Microscopy

PhD Thesis

Martin Kielhorn

May 2013

## Abstract

Photobleaching and phototoxicity pose a problem in live cell imaging. Fluorescence imaging induces reactive oxygen species in observed organisms which can alter the behaviour of the sample. Hence, minimising the light exposure is an important goal.

We augment a widefield epifluorescence microscope with two spatial light modulators. By controlling the spatial excitation pattern and the angle of illumination, we can adapt the illumination to the specimen. In many cases, this technique will create exposures with reduced excitation of the out-of-focus fluorophores, resulting in better image quality and less phototoxicity.

My custom software is used to obtain an initial image stack of the specimen. Subsequent image sections are exposed with excitation patterns that account for the previous image stack. Depending upon the distribution of fluorophores, this adaptive exposure can considerably reduce photobleaching and phototoxicity.

# Preface

This thesis describes my work that I performed in the EU funded seventh framework program project Micro mirror enhanced micro-imaging (project number 2115597) at King's College London between June 2008 until May 2013.

The project was a collaboration of the following five institutions: In-Vision (Guntramsdorf, Austria) Institut Pasteur (Paris, France) Fraunhofer IPMS (Dresden, Germany) KLA-Tencor Corporation (Migdal Haemek, Israel) King's College London (London, United Kingdom).

With Fraunhofer taking over the most intricate task of developing a MEMS display for the visual spectrum whose properties I discuss in section 4.1.2. The company KLA-Tencor investigated this device for an application in semiconductor manufacture. Pasteur and King's developed a concept for an application in life sciences which I motivate in section 1.1 and introduce in chapter 3. The company In-Vision designed and built custom optics for a prototype device. My task at King's College London was to develop the control software for the prototype and to prepare the device for life science fluorescence imaging.

## Source Code Availability

Source code that has been developed during this project is available for download on <https://github.com/plops/mma>. It contains implementations for:

- illumination planning based on a raytracing algorithm (see sections 3.2.5 and chapter 5)
- moving the z—stage of a Zeiss Axiovert 200M microscope body
- controlling an Andor Clara camera using the Andor SDK version 2. Control software for the cameras following below was developed:
  - Photometrics Cascade II (interface to unsupported closed-source driver, only works on very old 32-bit Linux kernels)
  - mvBlueFox 102G using the SDK

- Logitech Pro 9000 using a generic Video4Linux interface
  - Andor sCMOS using Andor SDK version 3
- displaying patterns using a graphics card that supports OpenGL on a ForthDD SXGA ferroelectric LCoS spatial light modulator with DVI video input
- controlling a stand-alone ForthDD WXGA 3DM spatial light modulator controller using USB
- estimating the parameters of a rigid transformation between camera and a spatial light modulator (see section 4.3 and appendix C.1),
- controlling the micro mirror array by Fraunhofer IPMS using their SDK
- some specific image processing tools:
  - three-dimensional convolution and Fourier transforms
  - drawing of lines and ellipsoids in volumes
  - rasterization of triangles (for creating shadow maps in the pupil plane, see section 6.3)
  - calculation of optical transfer function for high NA objectives
  - localization of spherical nuclei in volumetric data (parts of the algorithm as described in Santella et al. (2010))

The main development was done using GNU Linux. However, portability was kept in mind and most of the code works in Microsoft Windows as well.

The drawing on the title page shows the beam path through at 100 $\times$  objective with a numerical aperture of 1.45. The design parameters of the objectives that I used in this project are hard to come by and I used data from a patent (Matthaei et al. 2003).

## Acknowledgements

It is my pleasure to thank all those who have made this thesis possible. First and foremost, I owe my deepest gratitude to my supervisor Rainer Heintzmann for giving me the opportunity to become part of his research group at King's College London and later in the Institute of Photonic Technology in Jena.

I owe my sincere thanks to Kai Wicker, Jakub Nedbal, Susan Cox, Daniel Appelt, Ondřej Mandula, Ronny Förster, Ivana Šumanovac, Eckhard Birkner, Kathrin

Klehs, Sapna Shukla, Walter Müller and all the other members of our group for valuable discussions, support and review of the manuscript.

My sincere thanks to the European Union Framework Programme 7 for the studentship on this project. I also thank Erhard Ipp, Günter Zöchling, Vincent Galy, QueeLim Ch'ng, Jörg Heber, Mark Eckert, Dirk Berndt, Joel Seligson, Jean-Yves Tinevez and Florian Rückerl for helpful collaboration.

Furthermore, I highly appreciate the input of Herbert Gross, Miroslav Grajcar, Edward Rosten, Christophe Rhodes, Paul Khuong, Nikodemus Siivola, Gabor Melis and Luís Oliveira. Occasionally, the expertise and insight of them steered me into right direction or greatly simplified problems I faced.

Finally, I wish to thank the authors and contributors to the following software projects: Linux, GCC, Emacs, SBCL (Rhodes 2008), Maxima (Maxima.sourceforge.net 2012), Micromanager (Edelstein et al. 2010), DIPimage (Diplib.org 2012), Wireshark (Wireshark.org 2012), Latex, Inkscape (Inkscape.org 2012), Gimp (Gimp.org 2011), ImageJ/Fiji (Abràmoff et al. 2004; Schindelin et al. 2012) and Blender (Blender.org 2012). These free software projects and their communities are invaluable to my work and greatly enhance my efficiency.

The work presented in this thesis is my own, unless I cite a reference.

M. K.

Jena, Germany

May 2013

# Contents

1. Introduction	12
1.1. Phototoxicity in life sciences and the model organism <i>C. elegans</i> .	13
1.2. Photophysical principles of phototoxicity . . . . .	17
1.3. Conventional microscopes . . . . .	20
1.3.1. Ray-optical description of a large-aperture lens . . . . .	20
1.3.2. Wave-optical theory for image formation in a fluorescence microscope . . . . .	22
1.3.3. Illumination in a widefield epifluorescence microscope . . . . .	28
1.3.4. Phototoxicity in conventional microscopes . . . . .	29
1.3.5. Conclusion . . . . .	30
1.4. Image detectors in widefield microscopy . . . . .	30
1.4.1. Introduction . . . . .	30
1.4.2. Photon shot noise and read noise . . . . .	31
1.4.3. Comparison chart for detector selection . . . . .	34
1.4.4. Calibration of the EM-CCD gain . . . . .	38
1.4.5. Conclusion . . . . .	38
2. Methods for controlling illumination patterns	40
2.1. Light sheet fluorescence microscopy . . . . .	40
2.1.1. Light sheet generation with cylindrical lens . . . . .	40
2.1.2. Light sheet generation using the detection objective . . . . .	42
2.2. Scanning techniques with improved light utilization . . . . .	43
2.2.1. Two-photon laser scanning fluorescence microscopy . . . . .	44
2.2.2. Controlled light exposure microscopy (CLEM) . . . . .	44
2.2.3. Fast beam steering . . . . .	45
2.3. Non-scanning techniques . . . . .	47
2.3.1. Intensity modulation . . . . .	47
2.3.2. Direct illumination . . . . .	49
2.3.3. Temporal focusing . . . . .	50
2.3.4. Phase modulation . . . . .	51

## Contents

3.	The concept of spatio-angular microscopy	54
3.1.	Motivation . . . . .	54
3.2.	An imaging protocol with spatio-angular illumination control . . . . .	58
3.2.1.	Description of an exemplary biological specimen . . . . .	58
3.2.2.	Preparation of living embryo samples . . . . .	58
3.2.3.	Sectioning through structured illumination . . . . .	59
3.2.4.	Computer model for the integration of a priori knowledge about the biological events . . . . .	59
3.2.5.	Illumination optimization by means of raytracing . . . . .	60
4.	Description of our prototype for spatio-angular illumination	63
4.1.	Description of the optical components . . . . .	63
4.1.1.	Ensuring homogeneous illumination . . . . .	63
4.1.2.	Fourier optical filter for contrast generation on pupil plane SLM . . . . .	67
4.1.3.	Relay optics between pupil plane and focal plane SLM . . . . .	73
4.1.4.	Contrast generation on focal plane SLM using polarization	74
4.1.5.	Variable telescope as tube lens . . . . .	74
4.2.	Electronic control of the component . . . . .	75
4.3.	Mapping between pixels of the focal plane SLM and camera pixels	76
4.3.1.	The rigid transform . . . . .	77
4.3.2.	Experimental example and image processing . . . . .	78
4.3.3.	Conclusion on the mapping transformation . . . . .	80
4.4.	Optical sectioning by structured illumination . . . . .	80
4.4.1.	Discussion and outlook on optical sectioning . . . . .	84
5.	Raytracing for spatio-angular microscopy	85
5.1.	Basic geometric algorithms . . . . .	86
5.1.1.	Intersection of a ray and a plane . . . . .	86
5.1.2.	Intersection of a ray and a sphere . . . . .	86
5.1.3.	Refraction at planar surface . . . . .	87
5.2.	Refraction through lenses . . . . .	89
5.2.1.	Refraction through a paraxial thin lens . . . . .	90
5.2.2.	Refraction through high aperture objective (illumination) . . . . .	91
5.2.3.	Reverse path through oil objective (detection) . . . . .	92
5.2.4.	Treatment of aberration (detection) . . . . .	95
5.3.	Sphere projection . . . . .	96

## Contents

5.4. Conclusion . . . . .	98
6. Experimental results with spatio-angular microscope	99
6.1. Measuring acceptance angle for three different embedding media .	99
6.2. Measuring the light distribution by bleaching a fluorescent gel .	101
6.3. Spatio-angular illumination of three-dimensionally distributed beads	104
6.4. Angular illumination and a higher concentration of beads . . . . .	108
6.5. Conclusion . . . . .	109
7. Discussion	110
7.1. Outlook . . . . .	115
A. EM-CCD camera calibration	116
A.1. Andor Basic code listing for automatic image acquisition . . . . .	116
A.2. Python code listing for the read noise evaluation . . . . .	120
B. Optical sectioning by structured illumination using the HiLo method	123
C. Mapping between focal plane SLM and camera	129
C.1. Rigid coordinate transformation . . . . .	129
C.1.1. Application of the rigid transform in OpenGL . . . . .	130
C.2. Image processing: Localizing bright spots on the camera . . . . .	131

# Nomenclature

- $\beta$  Transversal magnification of an objective  $\beta = f_{\text{TL}}/f$ , for Zeiss lenses the magnification  $\beta$  is written on the objective and the focal length of the tube lens is defined as  $f_{\text{TL}} = 164.5 \text{ mm}$ , page 15
- $\mathcal{E}$  Etendue, information capacity, light gathering capacity or space-bandwidth product; its value is related to the number of point spread functions that can be resolved in the field., page 24
- $\Omega$  Excitation dose in  $\text{J}/(\text{cm}^2 \text{stack})$ , page 11
- $\Phi_e$  Radiant flux of excitation light in watts, page 11
- $\mathbf{r} = (r_x, r_y, r_z)^T$  Three-dimensional spatial coordinate, page 17
- $\mathbf{r}_t = (r_x, r_y)^T$  Transversal two-dimensional spatial coordinate, page 17
- $\mathbf{v} = (v_x, v_y, v_z)^T$  Three-dimensional spatial frequency, page 17
- $\mathbf{v}_t = (v_x, v_y)^T$  Transversal two-dimensional spatial frequency, page 17
- $\tilde{u}(\mathbf{v})$  Fourier transform of scalar field as a function of spatial frequencies, page 17
- $D_{\text{field}}$  Diameter in the field of the objective. The size of the illuminated area in the specimen., page 66
- $F_n$  Excess noise factor, page 29
- $u(\mathbf{r})$  Scalar field as a function of spatial coordinates, page 17
- AOD Acousto-optic deflector, page 40
- AOM Acousto-optic modulator, page 40
- chief ray Ray from the periphery of the field through the center of the entrance aperture, page 16
- CLEM Controlled light exposure microscopy, page 34

## Contents

- DBS Dichromatic beam splitter, page 56
- DMD Digital micro mirror device, page 43
- DPSS Diode-pumped solid-state (laser), page 43
- EGFP Enhanced green fluorescent protein, page 43
- EM-CCD Electron multiplying charge-coupled devices, page 7
- entrance aperture Projection of the limiting aperture of the optical system into object space, page 16
- Ewald sphere Transfer function of free space, page 19
- fLCoS Ferroelectric liquid crystal on silicon device, a reflective spatial light modulator based on switching liquid crystals between two bistable states. It is a particularly fast technology., page 104
- GFP Green fluorescent protein, page 43
- HILO Technique for microscopy illumination: highly inclined and laminated optical sheet, page 36
- HiLo An image processing method to obtain optical sections from widefield fluorescence images with structured illumination., page 53
- I<sup>2</sup>M Image interference microscopy, a technique that collects light with two opposing objectives and thereby improves resolution., page 22
- IFTA Iterative Fourier transform algorithm, page 46
- LCoS Liquid crystal on silicon (display), page 43
- LED Light emitting diode, page 43
- marginal ray Axial ray through the periphery of the entrance aperture, page 16
- MLE-PAM Minimized light exposure programmable array microscope, page 43
- MMA Micro mirror array, page 43
- NA Numerical aperture, page 24
- OPM Oblique plane microscopy., page 36

## Contents

PAM Programmable array microscopy, page 43

PCF Phase contrast filter, page 47

SPIM Selective plane illumination microscopy, page 35

TIR Total internal reflection., page 36

TL tube lens, page 44

USB Universal Serial Bus., page 104

VCSEL Vertical-cavity surface-emitting laser, page 43

YFP Yellow fluorescent protein, page 43

# 1. Introduction

In this work I discuss a modification of a fluorescence microscope that minimizes the toxic effects of the excitation light by utilizing two spatial light modulators to control the angle and position of the excitation light in the specimen.

phototoxicity

In the following introductory chapter I describe what phototoxicity is and how it comes about. Then I give an example of how it influences biological observations in a developing *C. elegans* embryo and describe how this particular biological system can be used to evaluate and compare the phototoxicity of different microscopes.

cameras

Later in this chapter I give an overview of image formation in the widefield microscope and I describe its principle limitations regarding resolution and depth discrimination. Furthermore, I discuss the two most important current image detector technologies — electron multiplying charge-coupled devices (EMCCD) and scientific complementary metal–oxide–semiconductor (sCMOS).

Regardless of whether it is the picture of earth captured by an orbiting satellite, the x-ray motion picture of a running dog or the time-lapse recording of a blooming flower. Images capture our imagination and they are a good starting point to develop new models and theories. This is particularly true for microscopy. Only after people became aware of microorganisms by direct observation, medieval quack could finally be overcome and modern medicine based on the scientific method flourished instead.

labeling, switching

Even today — with electron microscopes, magnetic resonance tomography and sequencing machines — optical microscopy still is an indispensable tool for research of living organisms. Fluorescence microscopy is of particular importance because it enables the scientist to selectively label a particular type of molecule in living cells and observe how they perform their biological function. Besides localizing molecules it permits measurement of physical quantities inside of the sample. Fluorescent labels can be used to report membrane potentials or viscosity inside of cells. Furthermore, light can exert a controlling function by exciting compounds that locally release chemicals with a biological function, e.g.

## 1. Introduction

a double-caged glutamate (Pettit et al. 1997), or triggering genetically encoded ion channels, e.g. the protein channelrhodopsin-2 (Boyden et al. 2005). However, the excitation light may introduce unnaturally large amounts of energy into the specimen which is potentially deleterious. If the exogenous light harms the observed organism in any way, this effect is called phototoxicity. A number of techniques can reduce phototoxicity: Two photon excitation, controlled light exposure, selective plane illumination, highly inclined and laminated optical sheet, and oblique plane microscopy. I introduce them in chapter 2. These techniques have different pros and cons and not all are equally suited for a specific problem, e.g. selective plane illumination is very effective, but it needs two perpendicular lenses and can not be used for multiwell plates or to observe the liver of a living, adult mouse.

In this work I present an approach that makes use of modern display and camera technology. We only modify the microscope's illumination path, the space around objective lens and specimen remains as accessible as in any conventional widefield microscope.

### 1.1. Phototoxicity in life sciences and the model organism

#### *C. elegans*

The partner in our project who is responsible for decisions related to life sciences and biology is Institut Pasteur (Paris, FR). They work on infectious diseases.

In order to motivate the importance of phototoxicity, I would like to portray an elegant drug screening experiment which I have seen on one of my visits in Paris (Aulner et al. 2013). For this study, mice macrophages were grown in multiwell plates and infected with a pathogen of a hitherto poorly treatable tropical disease. Usually, large vacuoles form in the infected cells, inside of which the pathogens proliferate. However, for this essay, a chemical from a compound library is added to the culture medium which can potentially harm or kill the pathogens. After an incubation period of a few days, the nuclei and vacuoles in the host cells are labeled with fluorescent dyes (the pathogens are genetically modified to express the fluorescent protein DSRed2) and an automatic spinning disk microscope (Opera QEHS, PerkinElmer Technologies, MA, USA) acquires images of each cell. The pathogens are counted by automatic image analysis and potential remedies among the compounds can thus be identified. In addition, analyzing the shape of the host cell nuclei can help to identify compounds that harm the host cell.

## 1. Introduction

Such studies of diseases are still in their infancy, but they have the potential to reduce the cost of drug discovery with the benefit that diseases will be examined whose cures are not expected to produce significant earnings. Furthermore, the cells of one animal can be used to investigate many different compounds.

In the described study, the images were acquired only once after the experiment. Even better insights are to be expected with real-time monitoring and kinetic studies, but in those cases one must also consider phototoxicity to prevent that the specimen is harmed by the excitation light before any effect of chemical compounds is visible.

As part of our collaboration, the Institut Pasteur developed a biological test system that is relatively easy to maintain (Stiernagle 2006), safe in use and allows the comparison of phototoxicity between different microscopes (Tinevez et al. 2012). The basis of this system are embryos of the small invertebrate *C. elegans*. The adult form is approximately 1 mm long. Their anatomy and development are comparatively simple and have been well characterized (Sulston and Horvitz 1977; Durbin 1987).

We use embryos of a genetically modified strain<sup>1</sup> that expresses eGFP tagged histones (enhanced green fluorescent protein, excitation maximum 488 nm, emission maximum 509 nm). Histones are incorporated into the chromatin during cell divisions, i.e. the nuclei of our worms fluoresce green. The mother worm passes a sufficient amount of these proteins into the egg. In the beginning of its development the embryo entirely relies on this reserve of histones. Only in a much later stage — certainly not during the first few hours, that we observe — it will form its own histones.

Figure 1.1 compares time-lapse experiments on three different *C. elegans* embryos with varying excitation intensities. The lineage tree of two developing *C. elegans* embryos is the same. With all other factors being equal, particularly if the temperature is constant at  $21 \pm 1^\circ\text{C}$ , two different embryos will develop at the same speed from egg to fertile adult in three and a half days. At the beginning of the experiment, embryos are removed from their mothers at an identical stage, before any cellular divisions have occurred. Then a z-stack of the egg with 41 slices and one micron z-sampling is obtained every two minutes.

The columns in Figure 1.1 depict three different embryos whose development was imaged according to this protocol for two hours and 38 minutes with different excitation powers. The figure displays the maximum intensity projections of the z-stacks. In order to make the cell nuclei visible in all images, I normalized the

---

<sup>1</sup>Our strain has WormBase ID AZ212 (Praitis et al. 2001; Gallo et al. 2008).

## 1. Introduction

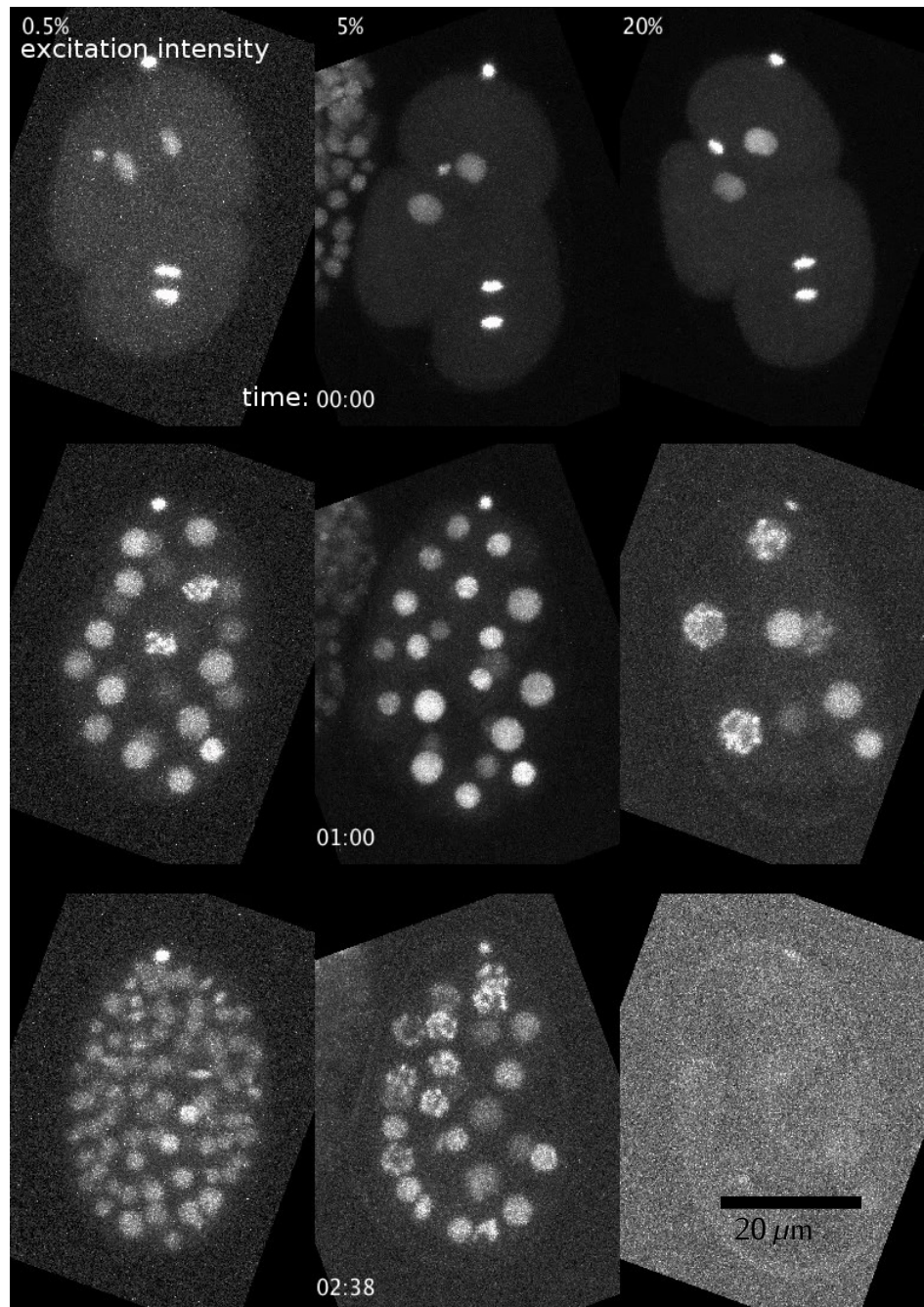


Figure 1.1.: Phototoxic effects while imaging the embryonal development of three *C. elegans* embryos (strain AZ212, histone-2B tagged with eGFP) with different excitation intensities. The embryo with lowest excitation dosage (left) develops fastest. The embryo with the highest dosage (right) ceases development and nearly all fluorophores are bleached after the experiment. Images by J.-Y. Tinevez using a Zeiss LSM700 confocal microscope (Institut Pasteur, Paris, FR).

## 1. Introduction

data to the same range. As can be guessed from the photon shot noise, the upper left image contains the least number of fluorescence photons, and the upper right the most.

An analysis of the time-lapse data show that one hour into the experiment the embryo with the highest excitation dose (right) has stopped developing and its fluorophores are strongly bleached. Some cells even turned apoptotic and went into programmed cell death. After two hours and 38 minutes the experiment was stopped and the embryo which was exposed to the lowest dose (left) has developed the largest number of cells. The middle embryo ceased developing while the right embryo died even earlier and nearly all its fluorophores are bleached at the end of the experiment.

In Figure 1.2 I reproduce quantitative data from Tinevez et al. (2012). Each data point in this graph corresponds to a two hour time-lapse imaging experiment of a *C. elegans* embryo in a widefield microscope. From a very low excitation up to a certain threshold dose the development is not affected by the light and approximately 50 cells develop during the two hours.

For a dose above the threshold the development is slowed due to phototoxicity and the number of cells at the end of the experiment decreases.

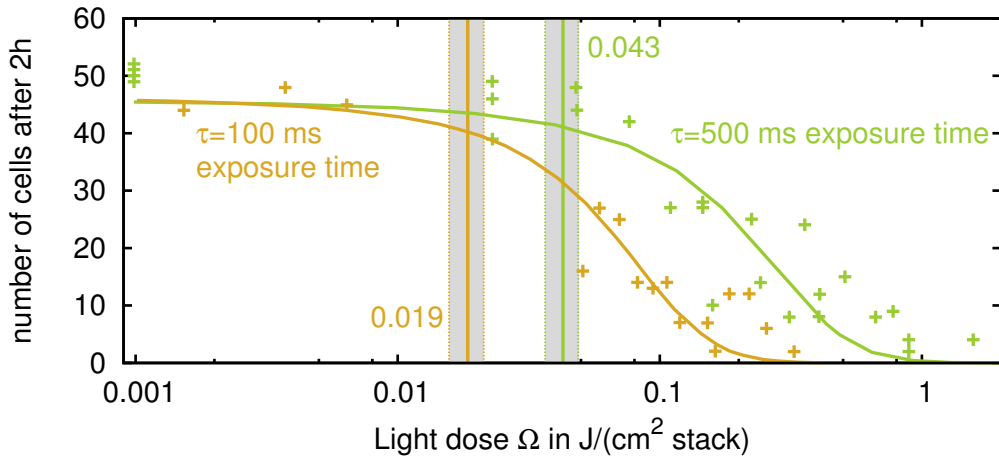


Figure 1.2.: Longer exposure times are less phototoxic. Each data point corresponds to one embryo that developed under a particular excitation dose for two hours. The solid lines are sigmoidal fits to the data. Also indicated are the two phototoxicity thresholds given by the inflection point of the sigmoid and their 95% confidence intervals. This data was provided by J.-Y. Tinevez (Institut Pasteur, Paris, FR) and is also published in Tinevez et al. (2012).

The orange data points in the diagram correspond to a per slice integration

## 1. Introduction

time  $\tau$  of 100 ms and for the green data the integration time is five times higher. The dose  $\Omega$  on the  $x$ -axis is calculated as

$$\Omega = \frac{\Phi_e n \tau}{A}, \quad (1.1)$$

with integration time  $\tau$ , area  $A$  of the illuminated field, the number of slices  $n = 41$  and radiant flux  $\Phi_e$  of the excitation light, as measured in the pupil.

Naively one would assume that it should not make any difference if the excitation light dose is administered with 100 ms or 500 ms exposures but these data show that a longer exposure time and low intensity are less phototoxic.

These results agree with an earlier study in tobacco plants (Dixit and Cyr 2003). They investigate cell death a few days after illumination and find that there is a threshold dose below which no phototoxicity can be detected, and that this threshold decreases with light intensity. Dixit and Cyr show that the damage is caused by reactive oxygen species and they explain the shift of the phototoxicity threshold by the limited capacity of the cells' scavenging system for those radicals. They also predict the existence of redox-sensitive checkpoints in the mitotic division cycle.

In summary this section describes how to measure phototoxicity with biological specimen. The next section gives an overview of the underlying photophysics and the rest of this work describes our attempt to build a microscope with reduced phototoxic footprint.

## 1.2. Photophysical principles of phototoxicity

Here I give a short overview of fluorescence of molecules in order to introduce the terms photobleaching and phototoxicity.

A fluorophore is a molecule that can absorb and subsequently emit light. During the absorption of a photon the molecular orbital transitions from the electronic ground state  $S_0$  to an excited state  $S_1$ . The lifetime of the excited state  $S_1$  is in the order of a few nanoseconds. A Jablonski diagram, as depicted in Figure 1.3, summarizes information about the energy levels of a molecule and possible transition processes.

The majority of known stable and bright fluorophores absorb and emit in the wavelength range between 300 nm and 700 nm. Photons at the high energy end of this range can excite molecules into higher energy levels  $S_n$ , ( $n > 1$ ) than the first excited state; these states are unstable and hardly return to the ground

energy levels

## 1. Introduction

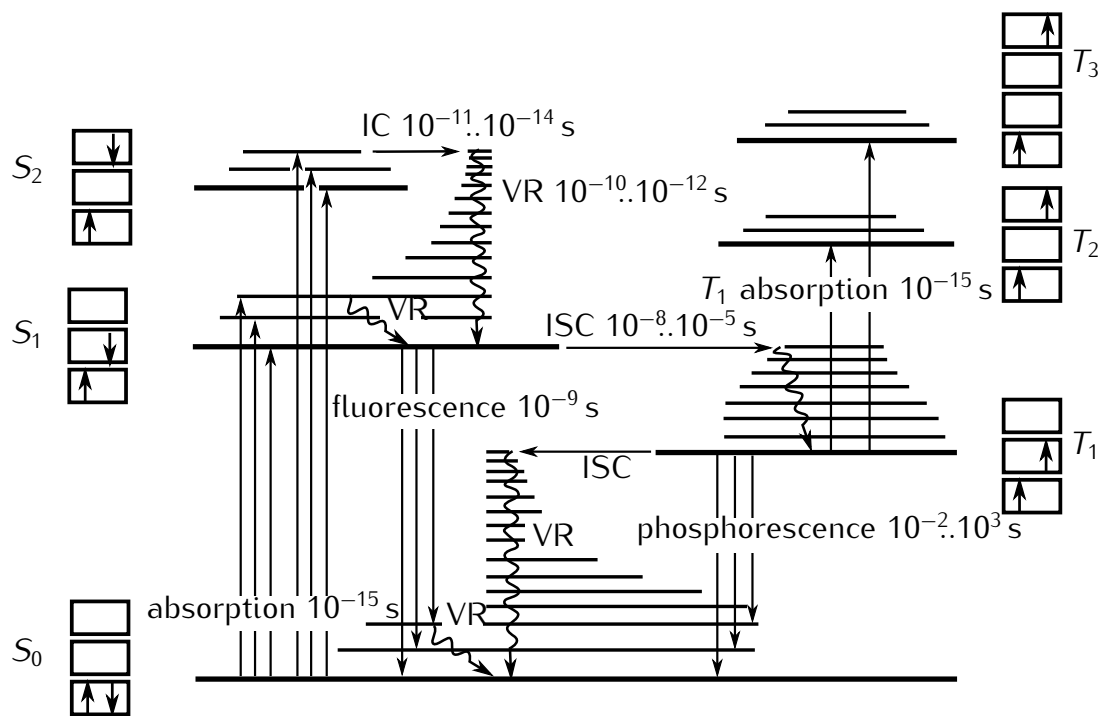


Figure 1.3.: The Jablonski energy level diagram of an illustrative fluorescent molecule. The boxes depict orbitals, up and down arrows symbolize the spin of the outer electrons. Fat horizontal lines represent electronic states. Thinner lines indicate vibro-rotational states. Various processes are shown with their typical time scales. VR = vibro-rotational relaxation, ISC = intersystem crossing, IC = internal conversion (inspired by Haken and Wolf 2006).

state  $S_0$ . On the other side of the spectrum: a molecule that absorbs in the near-infrared ( $> 700\text{ nm}$ ) has a low-lying excited singlet state  $S_1$  and therefore potentially increased reactivity and a high probability for a non-radiative transfer back into the ground state  $S_0$  (Sauer et al. 2011).

The term *Stokes' shift* describes the frequency shift between the absorbed and emitted photon; the energy difference is lost as heat to the fluorophore molecule and surrounding solvent. For the practical implementation of fluorescence microscopes this is significant, as it enables to separate excitation and emission light with a dichromatic beam splitter.

The excitation probability of a fluorescence molecule depends on the orientation of its dipole axis relative to the plane of vibration of the excitation field. Especially if the molecule is not rigidly bound to a bigger structure or embedded in a viscous solvent it will reorient its dipole during the fluorescence lifetime and emit the fluorescence photon in a random direction. We use this in the next section to

## 1. Introduction

describe image formation in the fluorescence microscope.

The triplet states  $T_n$  play an important role in photobleaching. Pure electronic absorption of one photon has no effect on the spin of an electron and therefore the transition from singlet states  $S_n$  into the triplet state  $T_n$  should not occur. However, interaction with the nuclei can mediate this spin transition. Therefore, in fluorophores this transition has a small probability, resulting in long lifetimes of the triplet state  $T_1$ .

Deschenes and Bout (2002) show that excitation of higher triplet states  $T_n$  is the predominant reactive process for photobleaching in vacuum. In particular they measured that one rhodamine 6G molecule *in vacuum* can emit more than  $1 \times 10^9$  photons before it bleaches, if the excitation intensity is low enough ( $\sim 1 \text{ W/cm}^2$ ) to prevent decay over triplet states.

In normal atmosphere the prolonged lifetime of the triplet state  $T_1$  makes it highly likely for the fluorophore to react with molecular oxygen  $O_2$ . Oxygen is abundant and has a triplet ground state  $^3\Sigma$  with two unpaired electrons of parallel spin in its  $\pi^*$ -orbitals (see Figure 1.4).

(Bernas et al. 2004)

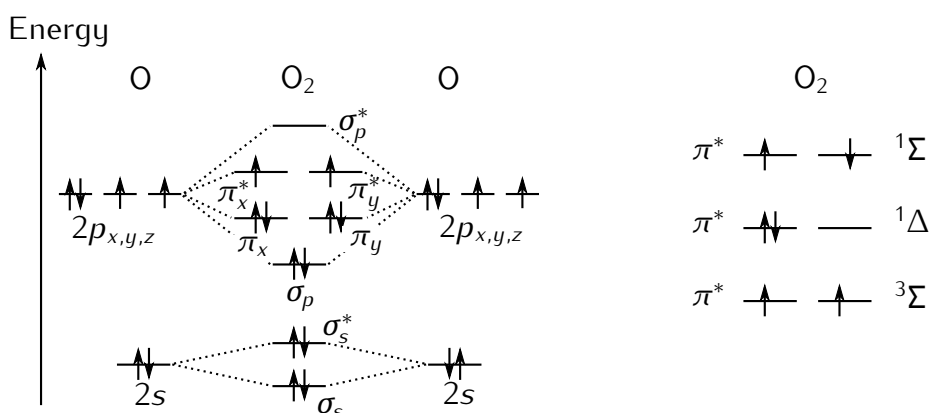


Figure 1.4.: **left:** Schematic that depicts how the orbitals of the oxygen molecule are formed from the atomic orbitals. **right:** Molecular oxygen has the lowest energy in its triplet state  $^3\Sigma$  where the spins of the two outer  $\pi^*$ -electrons are parallel. Inspired from van de Linde (2011).

If a ground-state oxygen molecule comes into physical contact with a  $T_1$  fluorophore, the energy of the latter can be transferred by an electron exchange energy transfer mechanism in which the orbitals directly interact with each other (Haken and Wolf 2006, p. 438 and van de Linde 2011).

During this reaction, which is also known as triplet-triplet annihilation, two forms of singlet oxygen form in competition: The lower energy state  $^1\Delta$  and the

## 1. Introduction

short-lived, higher energy state  ${}^1\Sigma$  that immediately ( $T_{1/2} \sim 10^{-9}$  s) sends out a 1268 nm photon and decays into  ${}^1\Delta$ .

The resulting singlet oxygen  ${}^1\Delta$  is very reactive. In a typical specimen it diffuses only a few tens of nanometres until it reacts with another molecule.

Nowadays many methods are known to reduce photobleaching: Substitute oxygen with noble gases or remove it enzymatically (Sauer et al. 2011, p. 89), depopulate the triplet state by adding reducing as well as oxidizing agents to the solvent (Vogelsang et al. 2008) or couple a triplet quencher directly to the fluorophore (Sauer et al. 2011, p. 19). For fixed samples it helps to change the solvent or polymer.

In living specimen these techniques may reduce photobleaching, but they can also have a detrimental effect on the biological system itself. Removing oxygen will quite certainly have a negative effect. In order to reduce phototoxicity it makes sense to think about the light management in the microscope.

### 1.3. Conventional microscopes

The widefield fluorescence microscope does not excite fluorophores of the specimen in an optimal way. In this section I outline how these microscopes work and explain how out-of-focus blur severely limits their performance. I introduce the terms point spread function, optical transfer function and etendue.

#### 1.3.1. Ray-optical description of a large-aperture lens

A microscope, is a device that collects light coming from one plane and forms a magnified image on a camera. Figure 1.5 b) shows a schematic representation of the detection path of a widefield microscope.

The main components are an objective lens with focal length  $f$  and a tube lens TL1 with focal length  $f_{TL} > f$ . Sample, lenses and camera are arranged in double-telecentric configuration, i.e. the sample is located in the front focal plane of the objective, the tube lens is at distance  $f_{TL}$  behind the pupil (i.e. the back focal plane of the objective) and the camera is in the focal plane behind the tube lens.

Light from the sample is collimated by the objective lens and re-imaged by the tube lens. The lateral magnification  $\beta$  is given by the ratio of the focal lengths of

## 1. Introduction

the two lenses:

$$\beta = \frac{\overline{O'P'}}{\overline{OP}} = \frac{f_{\text{TL}}}{f}. \quad (1.2)$$

Note that in Figure 1.5 b) I represent the objective lens as a single element. This is a simplification.

In the paraxial limit ray-tracing calculations for a thick lens or even several consecutive lens elements can be simplified by bending the ray only at one place — at the principal plane.

perfect imaging and high-aperture

Microscope objectives must collect light from a large aperture in order to produce a high resolution image. This is a fact I will support shortly using the wave-optical model. Unfortunately, the large ray angles in the objective prevent its simplified description using principal planes, but an analysis using the eikonal theory (Haferkorn and Richter 1984) shows that an optical system that fulfills the Abbe sine condition allows perfect imaging even for widespread ray bundles.

$$\beta = \frac{n \sin \alpha}{n' \sin \alpha'} \quad (\text{Abbe sine condition}) \quad (1.3)$$

with the object-sided collection half-angle  $\alpha$  and refractive index  $n$ , the corresponding parameters  $\alpha'$  and  $n'$  on the image side and the magnification  $\beta$ .

This condition ensures that the focal length, a quantity which is usually defined only for paraxial rays, is equal for all angles. This in turn means that such a lens carries out a Fourier transform from the front to the back focal plane with linear scaling. Note that a lens with a non-linear distortion in the back focal plane, such as given by the concept of a thin lens used at large angles, will fail to produce an image that is similar to the object.

aplanatic sphere

It turns out that ray bending in a high-aperture lens system that fulfills the Abbe sine condition can be simplified to a one bend at a single surface, quite similar to the utilization of principal planes in paraxial optics. For a high-aperture system this surface is no longer a plane. Instead it is a sphere with radius  $nf$  and called *aplanatic sphere*. The refractive index  $n$  accounts for an immersion medium on the object side. I depict the aplanatic surface as two circle segments with a bold red curve on each of the lenses in Figure 1.5 b).

In addition to the Abbe sine condition, microscope lenses are also corrected for spherical aberration and linear coma (Gross et al. 2005). Then the coma rays are symmetric around the chief ray, the wavefront and point spread function are approximately invariant for small field sizes (in first order). This ensures that the

## 1. Introduction

imaging conditions are invariant for small regions of the field plane and allows expression of the image formation with linear systems theory.

Figure 1.5 c) shows the illumination of a widefield fluorescence microscope with a laser. A dichromatic beam splitter (BS) separates illumination and returning fluorescence light.

### 1.3.2. Wave-optical theory for image formation in a fluorescence microscope

In the following section I will describe how the image on the camera is formed. For this one has to use wave theory because close to the image rays intersect, invalidating ray-optical predictions. As both wave-optical and ray-optical theory, are very much related, one can give a useful interpretation of the aplanatic surface for wave optics.

The underlying Maxwell equations and the wave equation are linear and we can represent propagating solutions (evanescent solutions are neglected) of the wave equation as a superposition of the elementary solution — the monochromatic, plane waves described by wave vector  $\mathbf{k}$ :

$$u(\mathbf{r}, t) = u \exp(i(\mathbf{k}\mathbf{r} - \omega t)), \quad \mathbf{r} = (r_x, r_y, r_z), \quad \mathbf{k} = (k_x, k_y, k_z), \quad |\mathbf{k}| = 2\pi \underbrace{n/\lambda_0}_{1/\lambda}, \quad (1.4)$$

with the coordinate  $\mathbf{r}$ , vacuum wavelength  $\lambda_0$ , refractive index  $n$  and wavelength  $\lambda$  in the immersion medium.

The accurate treatment of high-aperture optics would in fact require a vectorial calculation of the image for a fluorophore with a particular dipole orientation. Subsequently these images should be averaged to account for random fluorophore orientations, but as I do not need quantitative expressions, I limit myself to the simpler scalar problem which provides qualitatively similar results.

Assuming that the excited fluorophores in the sample give rise to a monochromatic electromagnetic field — I simplify the problem by omitting the complication that fluorophores emit photons in a wavelength range — then using the spatial frequency vector  $\mathbf{v} = \mathbf{k}/(2\pi)$  we can expand the three-dimensional, stationary field amplitude distribution  $u(\mathbf{r})$  into its spatial frequency spectrum  $\tilde{u}(\mathbf{v})$ :

$$u(\mathbf{r}) = \mathcal{F}(\tilde{u}(\mathbf{v})) := \int_{-\infty}^{\infty} \int_{-\infty}^{\infty} \int_{-\infty}^{\infty} \tilde{u}(\mathbf{v}) \exp(2\pi i \mathbf{r} \cdot \mathbf{v}) d^3 v \quad (1.5)$$

## 1. Introduction

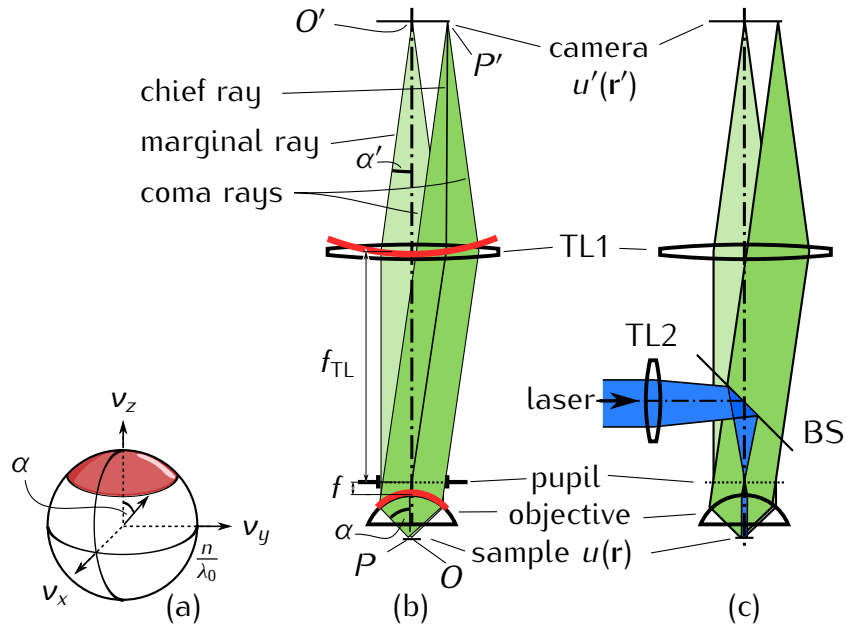


Figure 1.5.: a) Segment of the three-dimensional frequency spectrum of the light from the sample that is collected by the objective lens is highlighted in red on the Ewald sphere. b) Schematic of the detection path of a modern microscope. The sample is in the front focal plane of the objective. The detection tube lens TL1 forms a magnified image on the camera. The image points are denoted by \$O'\$ and \$P'\$. The aplanatic spheres for objective and tube lens are indicated in red. c) Parallel laser epifluorescence excitation. The excitation tube lens TL2 focuses a laser into the pupil of the objective. The beam is reflected by a dichromatic beam splitter (BS) towards the objective. An extended area in the specimen is illuminated. Fluorescence light returns through the objective, is transmitted through BS and forms an image on the camera.

$u(\mathbf{r}) :$	$\mathbb{R}^3 \rightarrow \mathbb{C}$	field distribution in sample space
$u'(\mathbf{r}') :$	$\mathbb{R}^3 \rightarrow \mathbb{C}$	field distribution in image space
$S(\mathbf{r}) :$	$\mathbb{R}^3 \rightarrow \mathbb{R}$	distribution of fluorophores in sample space
$I'(\mathbf{r}') :$	$\mathbb{R}^3 \rightarrow \mathbb{R}$	intensity distribution in image space
$\tilde{u}(\mathbf{v}) :$	$\mathbb{R}^3 \rightarrow \mathbb{C}$	spatial frequency spectrum of field in sample space
$a(\mathbf{r}) :$	$\mathbb{R}^3 \rightarrow \mathbb{C}$	amplitude point spread function
$\tilde{a}(\mathbf{v}) :$	$\mathbb{R}^3 \rightarrow \mathbb{C}$	amplitude transfer function, generalized aperture
$h(\mathbf{r}) =  a(\mathbf{r}) ^2 :$	$\mathbb{R}^3 \rightarrow \mathbb{R}$	intensity point spread function
$\tilde{h}(\mathbf{v}) :$	$\mathbb{R}^3 \rightarrow \mathbb{C}$	optical transfer function

Table 1.1.: Overview of the functions that are used in this section.

Where  $\mathcal{F}$  denotes the Fourier transform operation. I will use several functions in this section. See Table 1.1 for a listing of their names.

## 1. Introduction

Since we have assumed a monochromatic field and the length  $|\mathbf{v}|$  of the spatial frequency vector is the inverse of the wavelength ( $n/\lambda_0$ ), in the material of refractive index  $n$ , the support (denoted 'supp') of this spectrum  $\tilde{u}(\mathbf{v})$  is limited to the surface of a sphere of radius  $n/\lambda_0$ :

$$\text{supp } \tilde{u}(\mathbf{v}) = \{\mathbf{v} \in \mathbb{R}^3 : |\mathbf{v}| = n/\lambda_0\}. \quad (1.6)$$

This sphere is the transfer function of free space, and is also called Ewald sphere (see Figure 1.5 a)). Scaling the Ewald sphere with  $f\lambda_0$  gives the aplanatic surface of the lens. Note that the  $x$ -component of the marginal ray (in the  $xz$ -plane) corresponds to the spatial frequency component  $v_x = n \sin \alpha$  in object space and  $v'_x = n' \sin \alpha'$  with  $n' = 1$  in image space. The transversal spatial frequency components are related due to the Abbe sine condition (1.3):

$$\beta = v_x/v'_x, \quad \beta = v_y/v'_y. \quad (1.7)$$

The transfer function  $\tilde{a}(\mathbf{v})$  of the lens is defined by complex values on the Ewald sphere (McCutchen 1964):

$$\tilde{a}(\mathbf{v}) = \exp \left( 2\pi i \frac{n}{\lambda_0} W(\mathbf{v}_t) \right) \delta \left( \frac{n}{\lambda_0} - |\mathbf{v}| \right) \text{step}(|\mathbf{v}| \cos(\alpha) - v_z), \quad (1.8)$$

$$\text{step}(x) = \begin{cases} 1 & x \geq 0 \\ 0 & x < 0 \end{cases}, \quad (\text{Heaviside step function}) \quad (1.9)$$

with the Dirac delta function  $\delta$ , transversal spatial frequency vector  $\mathbf{v}_t = (v_x, v_y)^T$  and the wavefront error  $W(\mathbf{v}_t)$ . McCutchen calls the three-dimensional function  $\tilde{a}(\mathbf{v})$  the generalized aperture.

For this discussion I set  $W(\mathbf{v}_t) = 0$ , i.e. there is no wavefront aberration and the lens is diffraction limited. Furthermore, The Heaviside step function limits the size of the calotte (or cap) of the Ewald sphere that is defined by the acceptance angle  $\alpha$  of the objective.

Just as the objective lens, the tube lens can be described by its generalized aperture but I assume that the tube lens maintains a diffraction limited wavefront of the full angular range. For this discussion, the full microscope is readily described by the generalized aperture of just its objective lens.

Multiplication of the emission angular frequency spectrum  $\tilde{u}(\mathbf{v})$  with the generalized aperture  $\tilde{a}(\mathbf{v})$  gives the angular frequency spectrum of the amplitude in

## 1. Introduction

the image plane:

$$\tilde{u}'(\mathbf{v}') = \tilde{u}'(\mathbf{v}/\beta) = \tilde{u}(\mathbf{v}/\beta) \cdot \tilde{a}(\mathbf{v}/\beta). \quad (1.10)$$

Note that I use the transversal magnification  $\beta$  to scale the arguments of the functions, so that the result is given in image space spatial frequencies<sup>2</sup>.

According to the convolution theorem this multiplication in frequency space corresponds to a convolution in the domain of spatial coordinates  $\mathbf{r}$  of the field distribution  $u(\mathbf{r})$  and an amplitude point spread function  $a(\mathbf{r}) = \mathcal{F}(\tilde{a}(\mathbf{v}))$  that describes the imaging of the objective lens:

$$u'(\mathbf{r}') = u'(\beta\mathbf{r}) = (u \otimes a)(\mathbf{r}) = \int_{-\infty}^{\infty} \int_{-\infty}^{\infty} \int_{-\infty}^{\infty} u(\boldsymbol{\varrho}) a(\mathbf{r} - \boldsymbol{\varrho}) d^3\boldsymbol{\varrho} \quad (1.11)$$

where  $\boldsymbol{\varrho}$  is a spatial coordinate and the lateral magnification  $\beta = \mathbf{r}'/\mathbf{r}$  transforms between image space  $\mathbf{r}'$  and object space  $\mathbf{r}$ . This result shows that the three-dimensional amplitude distribution of the image is linearly related to the amplitude distribution in the sample. A stack of images is obtained by translating the sample in  $z$ .

A focal plane detector can only measure the intensity  $I'$  which depends non-linearly on the amplitude of the field  $u'$ . However, the fluorophores act as independent sources and their phases vary randomly with respect to each other. Each fluorophore gives rise to its coherent image  $h(\mathbf{r}')$  (Goodman 1968):

$$h(\mathbf{r}') = |a(\mathbf{r}')|^2. \quad (1.12)$$

The three-dimensional intensity distribution  $I'(\mathbf{r}')$  in image space can then be obtained by incoherently adding the individual images of the fluorophores:

$$I'(\mathbf{r}') = \int_{-\infty}^{\infty} \int_{-\infty}^{\infty} \int_{-\infty}^{\infty} S(\boldsymbol{\varrho}) h(\mathbf{r}' - \boldsymbol{\varrho}) d^3\boldsymbol{\varrho} = (S \otimes h)(\mathbf{r}') \quad (1.13)$$

where  $S(\boldsymbol{\varrho})$  represents the three-dimensional fluorophore distribution and  $\boldsymbol{\varrho}$  is the spatial coordinate in image space.

It is useful to discuss the Fourier transform of the intensity point spread function  $h$ . This is the three-dimensional optical transfer function of the microscope and

---

<sup>2</sup>Unfortunately, my notation is slightly problematic here. I assume that  $z$ -sampling occurs by stepping the sample through the object space while the camera is fixed in the focal plane of the tube lens. Therefore,  $r'_z$  has to be interpreted as a  $r_z$  position in sample space which does not correspond to a physical position outside the image plane.

## 1. Introduction

describes how well different object frequencies are transmitted:

$$\tilde{h}(\mathbf{v}') = \mathcal{F}(a(\mathbf{r}') a^*(\mathbf{r}')) = \tilde{a}(\mathbf{v}') \otimes \tilde{a}^*(-\mathbf{v}'). \quad (1.14)$$

The product of the amplitude point spread function  $a(\mathbf{r}')$  and its complex conjugate corresponds to an auto-correlation of the amplitude transfer function in spatial frequency space. Note that the complex conjugation of the second factor  $a^*(\mathbf{r}')$  results in an inversion of the argument of  $\tilde{a}^*(-\mathbf{v}')$ .

This expression allows a geometric interpretation of the support of the optical transfer function  $\tilde{h}(\mathbf{v}')$  (Gustafsson et al. 1995). Equation (1.14) describes a convolution of two spherical caps whose open sides are facing each other. The entire covered volume somewhat resembles a torus with vanishing internal diameter. Figure 1.6 depicts a  $v_x v_z$ -cross-section for two different aperture angles  $\alpha$ . The

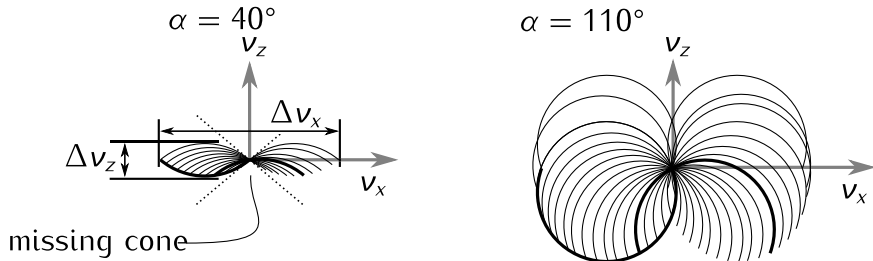


Figure 1.6.: Schematic depicting  $v_x v_z$ -cross sections of the support of optical transfer function  $\tilde{h}$  for microscope objectives with different collection angles. **left:** Objectives, that only collect light that is directed into one half space, have the missing cone problem. **right:** Optical transfer function for fictional objective with larger collection angle and no missing cone.

lateral  $\Delta v_x$  and axial  $\Delta v_z$  extent of the optical transfer function can be expressed in terms of wavelength  $\lambda_0$ , immersion index  $n$  and aperture angle  $\alpha$ :

$$\Delta v_x = \begin{cases} 4n \sin(\alpha)/\lambda_0 & 0 \leq \alpha \leq \pi/2 \\ 4n/\lambda_0 & \pi/2 < \alpha < \pi \end{cases}, \quad \Delta v_z = 2 \frac{n}{\lambda_0} (1 - \cos \alpha), \quad (1.15)$$

resolution of an objective

allow to give lower bounds for the smallest periodic structure that can still be resolved using a well corrected objective:

$$\Delta d_x = \frac{2}{\Delta v_x} = \frac{\lambda_0}{2n \sin \alpha}, \quad \Delta d_z = \frac{2}{\Delta v_z} = \frac{\lambda_0}{n(1 - \cos \alpha)}. \quad (1.16)$$

In order to sample the bandwidth limited signal in the image plane correctly,

## 1. Introduction

the pixel pitch  $p_x$  of the camera must be smaller than half of the resolution:  $p_x < \beta\Delta d_x/2$  (Nyquist criterium). A similar relation holds true for the  $z$ -sampling:  $p_z < \Delta d_z/2$ . Too large a sampling period will result in aliasing artifacts.

Note that the axial resolution  $\Delta d_z$  is substantially worse than the lateral resolution  $\Delta d_x$  in normal microscope with a collection aperture  $\alpha < \pi/2$  that is restricted to only one half-space.

Additionally the optical transfer function of such a microscope is empty in a cone shaped region around the axis above and below the origin. This means that in a conventional widefield microscope it is impossible to bring into focus a (defect-free) fluorescent plane because low spatial frequencies do not attenuate with defocus (Neil et al. 1997). This effect is also called “missing cone problem” (Streibl 1984).

It is instructive to look at a microscope, that is not hampered by the missing cone problem: In image interference microscopy ( $I^2M$ ) two opposing microscope objectives collect light from the sample and the two detection beam paths are brought to interference using a beam splitter on a focal plane detector. This configuration substantially increases the collection angle, improves the  $z$ -resolution and fills the missing cone but puts stringent requirements on the optical path difference between the two interferometer arms, i.e. this device is very sensitive to sample-induced aberrations and in practice, with fluorophores that emit in a broad wavelength range, this method only works for samples which are only a few microns thick (Gustafsson et al. 1999).

Light from the focal plane interferes constructively on the detector, light emitted at  $\lambda/4$  distance away from the focal plane interferes destructively, light that is emitted at several wavelengths distance from the focal plane contributes as an incoherent sum to the detected signal. Therefore, a  $z$ -stack of a fluorescent plane captured with two opposing lenses compared to just one lens will give a signal that is four times as bright in focus, shows damped oscillations (because of the finite spectral band emitted by the fluorophores) when moving away from focus and has twice the brightness out-of-focus. This means the axial location of the fluorescent plane can be measured in  $I^2M$  but there is still background signal (Gustafsson et al. 1995).

The reason for this background signal is conservation of energy from plane to plane. A light ray that started in a certain object point does not stop in the corresponding image point. Therefore, most out-of-focus light is added incoherently as a background to the detected signal.

Structured illumination can be used to remove this out-of-focus light. Two major

## 1. Introduction

incarnations of this technique are in current use. On the one hand there is the confocal microscope in which mechanically scans a single point spread function over the focal plane. This approach allows blocking out-of-focus light optically. The concept was invented by Minsky in the late fifties (Minsky 1961), the first confocal microscope with a laser was built in the early seventies (Davidovits and Egger 1971) and was commercialized after breakthroughs regarding the scanning mechanics in the late eighties Amos et al. (1987). Due to the excellent quality of its images and the ease of use the confocal microscope became a standard tool for biology and life sciences.

optical sectioning  
using structured  
illumination

On the other hand there is an approach where a pattern with a significantly larger proportion of illuminated area is projected into the focal plane. Images are then captured with a camera. Several such exposures (at least two) can then be computationally processed to separate in- and out-of-focus light (Neil et al. 1997). Advantages of this method are that it requires no mechanical scanning and therefore can be much faster. Furthermore, camera sensors have a higher quantum efficiency than the photomultiplier tubes that were typically found in confocal systems, although this difference disappears when avalanche photodiodes are used. A significant disadvantage, however, is that the out-of-focus light is always measured with the detector. Its accompanying photon shot noise reduces the quality of the signal (see section 1.4.2). Therefore, this method is particularly problematic in thick fluorescent samples with much more out-of-focus than in-focus light. The confocal microscope is in this sense the better tool because its picture quality is independent on the fluorophore distribution in the specimen.

### 1.3.3. Illumination in a widefield epifluorescence microscope

As mentioned in section 1.2, fluorescence photons are essentially emitted in all directions (nearly) independent of the original illumination direction. Therefore it is possible and convenient to use the objective for excitation as well as detection. This mode of microscopy is called epifluorescence (Greek:  $\varepsilon\pi\iota$ ; on, above). In this configuration usually only a small percentage of the excitation light returns due to scattering or reflection. This simplifies the separation of fluorescence light from excitation light.

The blue beam in Figure 1.5 c) depicts a collimated laser that is focused into the pupil of the objective by tube lens TL2. The beam is reflected at a dichromatic beam splitter (BS). This is a glass plate that has been coated with dielectric layers. The refractive index, thickness and sequence of the layers are designed so

## 1. Introduction

that the excitation light is reflected towards the objective. Excitation light, that is scattered or reflected in the sample and returns through the objective is reflected towards the light source. However, lower energy fluorescence light returning from the objective is transmitted towards the camera. Behind the objective the beam is collimated and illuminates the specimen. The field of view is the demagnified diameter of the laser beam before TL2.

### Non-uniformity due to coherent interference

Note that tiny dirt particles in the excitation beam path can cause coherent interference and produce unwanted non-uniformities in the illumination. As a remedy the spatial coherence of the laser is sometimes reduced. Incoherent light emitting diodes, mercury or xenon arc lamps are often used instead of lasers. In the latter case a band pass filter selects the useful part of the spectrum of the excitation lamp upstream of the dichromatic beam splitter.

### The space-bandwidth product of a microscopic lens

etendue

A useful quantity in optics is the etendue  $\mathcal{E}$ . For a microscope objective its value is related to the number of point spread functions that can be resolved in the field. Therefore this quantity is also called information capacity, light gathering capacity or space-bandwidth product. For a high-aperture lens, the etendue is given by

$$\mathcal{E} = \frac{\pi}{4} (D_{\text{field}} \text{NA})^2, \quad (1.17)$$

with the numerical aperture NA and the field diameter  $D_{\text{field}}$ . The typical image diameter for Zeiss microscopes is 25 mm. For a  $63\times$  oil-immersion objective with  $\text{NA} = 1.4$  this corresponds to a field diameter of  $D_{\text{field}} = 0.4$  mm and an etendue of  $\mathcal{E} = 0.27 \text{ mm}^2/\text{sr}$ , where 'sr' denotes steradian, the SI unit of solid angle.

#### 1.3.4. Phototoxicity in conventional microscopes

When imaging living specimen we should distinguish between useful and unnecessary excitation. Taking into account the detection capabilities of objective lenses we should maximize the ratio of in-focus to out-of-focus fluorescence. The epifluorescent widefield and confocal microscope surely do not represent an optimum in this regard.

## 1. Introduction

In the next chapter on page 40 I will introduce other microscopy techniques that are more considerate of where to deposit excitation power within the specimen.

### 1.3.5. Conclusion

In this section I introduced a theoretical model that describes image formation in a widefield microscope. For well-corrected, diffraction-limited lenses this process is linear in intensity and three-dimensionally shift-invariant. In order to predict the image of a three-dimensional sample it is sufficient to know the image of a single point source.

By investigating this point spread function and its Fourier transform it is possible to give the simple relationships in equations (1.16) for the best possible resolution. Furthermore, I describe the missing cone problem, a limitation inherent in all lenses that only collect light from one half-space.

## 1.4. Image detectors in widefield microscopy

I describe the operation of CCD, EM-CCD and sCMOS focal plane detectors.

Then I utilize a simple noise model to compare different camera models and describe a simple method to calibrate cameras so that their data is represented in the standardized unit of effective photoelectrons.

### 1.4.1. Introduction

detection

Nowadays, all widefield microscopes use silicon-based cameras to measure and digitize the intensity distribution in the intermediate image plane. The semiconductor surface is patterned with a two-dimensional array of PIN photodiodes that generate and collect an intensity-dependent amount of free charge carriers when their depletion region is exposed to photons in the visible range.

quantum efficiency  
and back-thinning

Modern detectors can have a very high probability of a photon being absorbed and contributing to final signal (quantum efficiency  $Q_E$ ). For the most light sensitive devices even the backside of the silicon substrate is removed until the diodes can be exposed from the backside. In this way, the diodes can cover the entire surface and the fill factor is not reduced due to opaque wires running over the surface. Such detectors are called 'back-thinned' and can achieve a quantum efficiency of up to 95% for green light.

There are basically two different technologies to measure and digitize the charge that was collected in the photodiodes of focal plane arrays:

## 1. Introduction

Charge-coupled  
devices (CCD)

charge amplifier

active-pixel sensor

In the passive-pixel sensor columns of diodes form a linear row of capacitors. By applying a sequence of different voltages of up to 6 V to each of three adjacent capacitors the charge can be transported line by line out of the sensor — therefore, this technology is known as charge-coupled device (CCD). An additional row of similar capacitors (denoted horizontal shift register) on one side of the array pushes the carriers into a charge amplifier. This consists of a capacitor (the read node) and a field-effect transistor that amplifies the voltage across the read node. This voltage  $U$  linearly depends on the charge  $Q$  with  $U = Q/C$ . Camera sensor are designed to minimize the capacitance  $C$  of the read node to maximize sensitivity (Pawley 2006).

In the active-pixel sensor (e.g. sCMOS) each individual photodiode is surrounded by its own transistors for readout and reset. The two-dimensional array is addressed with an access enable wire which is shared by pixels of a line and an output wire, which is shared by pixels of a column. In the simplest case (with three in-pixel transistors) start of integration and readout occurs one line at a time (rolling shutter).

When I started this work in 2008, passive CCD sensors were state of the art detectors for fluorescence microscope with regards to sensitivity and speed. Now, however, faster and cheaper active-pixel sensors that provide comparable or better noise performance, become commercially available.

In the next section I will deal with various noise sources that affect the signal of focal plane detectors. This is relevant when comparing the performance of cameras from different manufacturers or to determine the optimal parameter settings for one particular experiment. Furthermore, it is possible to use the photon shot noise to calibrate cameras (or any other intensity detector) and convert their measurements to effective photoelectrons. This allows the comparison of images of different microscope systems (confocal, spinning disk or widefield) or and facilitates the use of sophisticated noise reduction algorithms.

### 1.4.2. Photon shot noise and read noise

Photon shot noise

Fluorescence photons arrive at the detector independently of each other. This random process leads to fluctuations in the number of the detected photons and can be described by the Poissonian probability mass function (denoted as 'pois'):

$$\text{pois}(k; \lambda) = \frac{\lambda^k \exp(-\lambda)}{k!}, \quad \lambda \in \mathbb{R}, \quad k = 0, 1, 2, \dots \quad (1.18)$$

## 1. Introduction

Note that in this particular equation the quantities have a different meaning than in other parts of this work. The variable  $k$  describes the number of measured photons and the real number  $\lambda$  is the average number of photons that reach the detector during the integration time. Figure 1.7 displays the discrete detection probabilities for three different values of  $\lambda$ . For large  $\lambda > 10$  photons, the shape of the Poisson distribution is excellently approximated by the normal distribution with mean and variance  $\lambda$ .

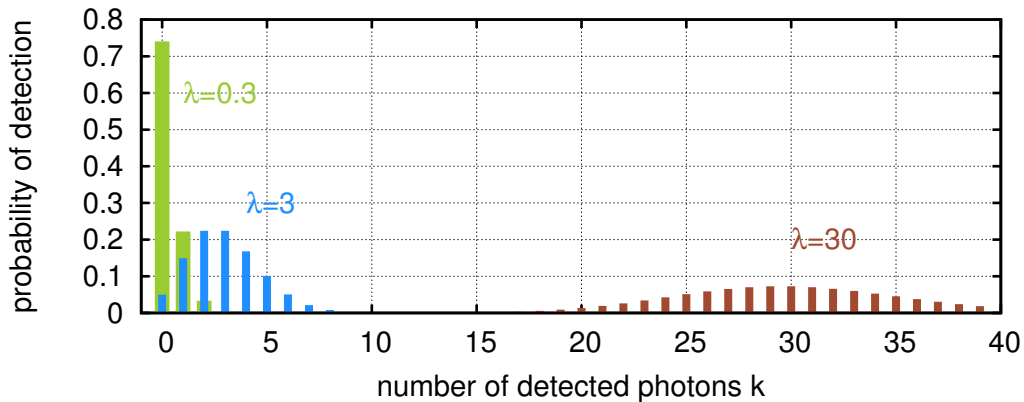


Figure 1.7.: Poissonian probability mass function  $\text{pois}(k; \lambda)$  for three photon fluxes with different average photon numbers  $\lambda$ .

We can calibrate every detector in order to specify the measurement in the unit of “effective” photoelectrons. For this, we utilize the property of the Poisson distribution that the variance  $(\Delta I)^2$  of an intensity measurement (in the unit of photoelectrons, denoted as  $e^-$ ) is equal to the average intensity  $\langle I \rangle$ :

$$(\Delta I)^2 = \langle (I - \langle I \rangle)^2 \rangle = \langle I \rangle. \quad (1.19)$$

detector gain calibration

For the calibration of a detector, twenty images of a defocused fluorescent object (see left image in Figure 1.8) are acquired. From the twenty images the variance of the intensity is determined for each pixel. Then all occurring intensities are collected into 100 bins. The average intensity variance of each bin is then plotted against the intensity (see right image in Figure 1.8). The data lie on a straight line. From its slope we calculate the gain to convert the arbitrary analog-to-digital units into the number of effective photoelectrons. If the data is plotted in this unit, the slope of the line is one, according to equation (1.19). The smooth light distribution in the input images ensures a good coverage for each data point in the variance-intensity plot and a bit of protection against drift.

measuring read noise

To determine the quality of a detector we ensure that no light falls on the

## 1. Introduction

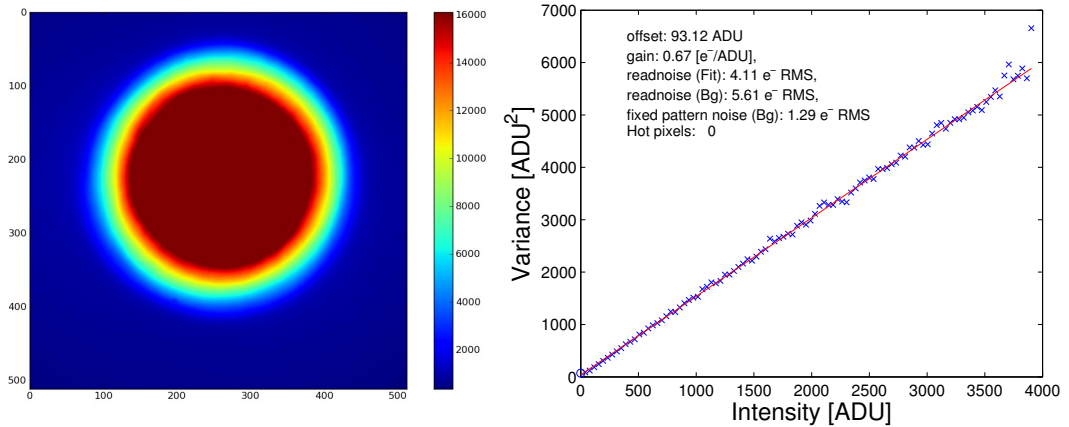


Figure 1.8.: **left:** Image of a defocused area on a fluorescent plane sample. This is used for calibrating the detector. **right:** Result of a detector calibration. Using the slope of the curve the arbitrary analog-to-digital units are converted into effective photoelectrons. The point of interception at the  $y$ -axis gives the detector read noise.

detector and create twenty dark images. For an ideal, noise-free detector these images would contain zero everywhere. In a real CCD sensor the variance of the values in the dark images reflect the readout noise  $N_r$  and the mean estimates the offset. Using the calibration gain, the readout noise can be specified as photoelectrons/pixel ( $e^-/\text{px}$ ).

The analysis for the right diagram in Figure 1.8 gave a readout noise of  $5.6 e^-/\text{px}$ . For the evaluation I used the function `cal_readnoise` of the DIPimage toolbox for Matlab (Lidke et al. 2005). In Appendix A.2 I list an alternative Python implementation of this algorithm.

The major source for readout noise is the charge amplifier. Its noise is added uniformly to every image pixel. For readout frequencies above 1 MHz the readout noise increases with the square root of the read speed (Pawley 2006). Until a decade ago this limited the readout speed of scientific CCD cameras. Then a new type of sensor was developed — the electron-multiplying CCD (EM-CCD) (Mackay et al. 2001).

This device contains an additional sequence of capacitors (denoted multiplication registers), which are operated with a high voltage (up to 46 V). The field accelerates electrons and they can generate more charge carriers by a process called impact ionization. This is a statistical process and for every electron going through a multiplication register, there is an average probability  $p$  that it creates another electron. This probability is quite low ( $p < 1.3\%$ ) but after a sequence of 536

electron-multiplying  
CCD

## 1. Introduction

registers the gain  $M = (1 + p)^{536} \approx 1015$  is so high, that even readout noise at 17 MHz readout speed can be neglected.

This amplification process consumes a lot of energy and requires an elaborate cooling scheme of the detector chip as the gain is temperature dependent.

Unfortunately, the statistical nature of impact ionization leads to an uncertainty in gain and therefore introduces a new noise source. As a gain this noise acts multiplicatively on the signal. Robbins et al. (2003) analyzed the amplification process and shows that the multiplicative noise, which is also called excess noise, has the effect of halving the apparent quantum efficiency of the detector.

Note that for very low light conditions with a minute probability to detect more than one photon per pixel, the EM-CCD can be run with maximum gain as a binary detector in photon counting mode. In this mode the excess noise has no effect whatsoever; but other noise sources become important.

### 1.4.3. Comparison chart for detector selection

Now I will introduce a comparison chart that I first saw in Hamamatsu (2012a). It is based on a single equation for the signal-to-noise ratio SNR and, if the detector parameters, such as readout noise and quantum efficiency, are known, a quantitative estimate of the expected quality of the data can be made.

Shot noise defines the fundamental limit for the signal-to-noise ratio in photo detectors (Sheppard et al. 2006). As already mentioned above, the expected noise for a signal of  $S$  photons is  $\sqrt{S}$ . Assuming the contributions to a detector pixel are  $S$  signal photons, perturbed by an additional number of  $I_b$  photons background light. The signal-to-noise  $\text{SNR}_{id}$  ratio for an ideal, noise-free detector is:

$$\text{SNR}_{id} = \frac{S}{\sqrt{S + I_b}}. \quad (1.20)$$

A conventional detector with reduced quantum efficiency  $Q_E \in [0, 1]$  and additive, Gaussian readout noise with standard deviation  $N_r$  (in e<sup>-</sup>/px) can only produce a worse signal-to-noise ratio:

$$\text{SNR}_{add} = \frac{Q_E \cdot S}{\sqrt{Q_E(S + I_b) + N_r^2}}. \quad (1.21)$$

This equation can be adapted for the electron-multiplying CCD. There, the readout noise is reduced because of the gain  $M$  but the influence of the shot noise is

excess noise reduces quantum efficiency

## 1. Introduction

doubled due to the excess noise factor  $F_n = \sqrt{2}$ .

$$\text{SNR} = \frac{Q_E \cdot S}{\sqrt{F_n^2 \cdot Q_E \cdot (S + I_b) + (N_r/M)^2}} \quad (1.22)$$

This equation permits comparison between all the cameras that I can use for my experiments. Table 1.2 lists parameters from their datasheets and the three diagrams in Figure 1.9 shows curves of the relative signal-to-noise ratio  $\text{SNR}/\text{SNR}_{id}$  for three different amounts of background light  $I_b$ .

When choosing the parameters I attached particular importance to the noise performance, even if that comes with a loss in readout speed.

camera type	$f_{\text{read}}$ [MHz]	$QE$	$N_r$ [e <sup>-</sup> /px]	$F_n$	$M$	model
back-thinned CCD	1	0.95	5.3	1	1	E2V CCD97
EM-CCD	1	0.95	15.0	$\sqrt{2}$	80	E2V CCD97
EM-CCD single photon	17	0.95	89.0	1	1000	E2V CCD97
sCMOS global shutter	200	0.52	2.3	1	1	Fairchild CIS2521F
sCMOS rolling shutter	140	0.72	1.3	1	1	Hamamatsu FL-400
back-thinned sCMOS	—	0.95	0.7	1	1	— <sup>3</sup>
interline CCD	20	0.62	6.5	1	1	Sony ICX285
interline CCD	1	0.62	2.4	1	1	Sony ICX285

Table 1.2.: Camera parameters for the curves in Figure 1.9.

For a very large number of photons the detector with the highest quantum efficiency  $QE$  wins (back-thinned CCD, green line):

$$\lim_{S \rightarrow \infty} \frac{\text{SNR}}{\text{SNR}_{id}} = \frac{\sqrt{Q_E}}{F_n}. \quad (\text{high light limit}) \quad (1.23)$$

For detectors with readout noise, there is a number  $S_n$  of signal photons below which the readout noise dominates:

$$S_n = \frac{N_r^2}{M^2 F_n^2 Q_E} - I_b. \quad (\text{photon shot noise limit}) \quad (1.24)$$

I indicate both limits in Figure 1.9 using different line types. The line is dotted in the region where the readout noise dominates, followed by a thick solid line where both photon shot noise and readout noise contribute. A thin line indicates the region where the relative SNR is within 95% of the high light limit and the

<sup>3</sup>Back-thinned sCMOS are not available at the time of writing.

## 1. Introduction

sensor's quantum efficiency becomes the parameter that defines the performance.

interpretation of  
EM-CCD in Figure 1.9

The first thing I want to look at is the EM-CCD. For a high gain of  $M = 20$  the curve is horizontal and the sensor differs from the ideal detector only in terms of a reduced apparent quantum efficiency. In a low background environment  $I_b = 0.3$  the electron multiplying mode is only advantageous for signals with less than 30 photons per pixel. For a higher background  $I_b = 30$  electron multiplication does not improve noise performance — but note that in this mode the sensor could be read out at a 10 times higher speed.

In a low background environment and low signal level the EM-CCD comes very close to the ideal detector, when it is run in photon counting mode as indicated by the blue-green line in the top left. In this case, however, an effect which was neglected in equation (1.22) becomes important. The impact ionization which is used to advantage in the multiplication registers occurs with low probability during vertical shifts of the signal and thereby adds approximately  $200 \text{ e}^-/\text{frame}$  of spurious charge. This effect is called clock-induced charge.

sCMOS in Figure 1.9

Next, I discuss the curves of the active-pixel sensors. The device designated as global shutter sCMOS is a sensor with five transistors per pixel (Vu et al. 2011). Similar to a passive-pixel CCD sensor the global shutter can start the exposure in all pixels simultaneously, but it has two major drawbacks. The additional two transistors cover space that would otherwise be available as light sensitive area and for quantitative data, a reference frame must be taken for each image, which increases the readout noise (Gamal and Eltoukhy 2005; Hamamatsu 2012a).

The rolling shutter sCMOS sensor has only the minimum three transistors per pixel and therefore a correspondingly higher quantum efficiency. For a signal between 6 and 80 electrons per pixel this sensor provides the best quality at 8 times higher readout speed than the EM-CCD. Rolling shutter means that the pixel lines are read in succession but for our prototype it is crucial that all pixels integrate while the displays show patterns. Fortunately there is a mode called global exposure synchronization which initiates integration in the pixels line by line and generates a trigger output once all pixels have started capturing light. This allows using the camera as a master without further effort but the camera can also be run as a slave. In that case the only requirement is that the trigger comes early enough (10 ms, Hamamatsu (2012b)) to initiate exposure in all lines before the illumination is activated.

The entry back-thinned sCMOS is only a hypothetical sensor which I added to compare the performance of a low noise active-pixel sensor with near perfect quantum efficiency.

## 1. Introduction

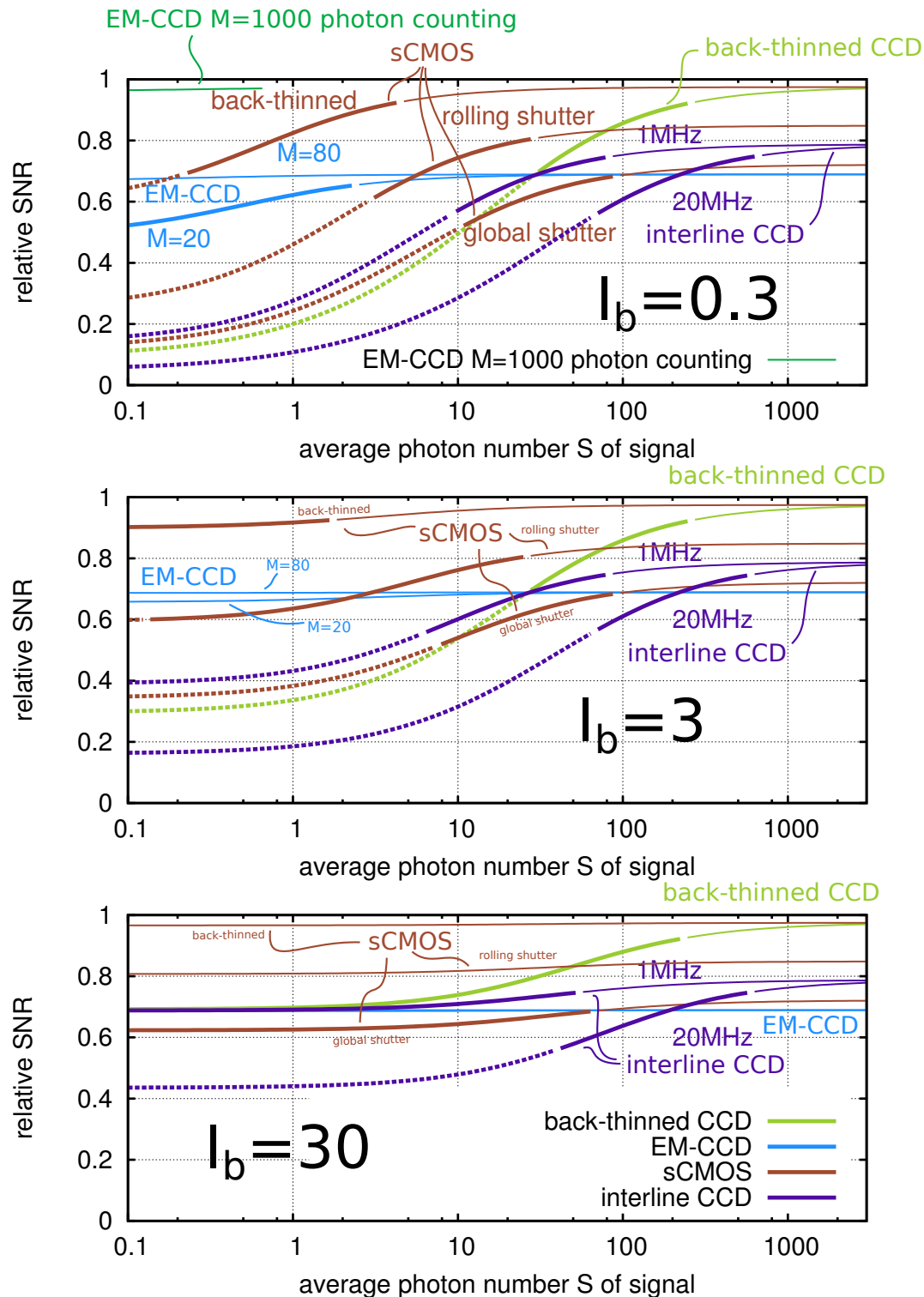


Figure 1.9.: Comparison of signal-to-noise ratio for different cameras. Dotted line for lowest light level, where  $N_r$  is the dominant noise; thin line indicates high light region where quantum efficiency and excess noise factor  $F_n$  matter.

## 1. Introduction

### 1.4.4. Calibration of the EM-CCD gain

The method I presented for CCD calibration in section 1.4.2 can be applied to measure the gain  $M$  and the excess noise factor  $F_n$  of an EM-CCD. This requires dark images and image sequences of the smooth intensity distribution (from exactly the same sample and illumination) with and without electron multiplication gain, so that data for both cases can be converted into detected photoelectrons.

The apparent quantum efficiency with gain is  $Q_E/F_n$ . Therefore the excess noise factor can be calculated with

$$F_n = N_{(1)}/N_{(M)} \quad (1.25)$$

where  $N_{(1)}$  and  $N_{(M)}$  are the sums of photoelectrons in the image without and with electron multiplication gain, respectively.

The variance for data without gain is  $(\Delta I)_{(1)}^2 = Q_E \langle I \rangle$  and smaller than for data with gain, where the variance is  $(\Delta I)_{(M)}^2 = Q_E F_n^2 \langle I \rangle$ .

The  $x$ -axis in the intensity-variance plot is equal to the intensity for gain-free data and scaled with  $M$  for the amplified data. The gain  $M$  can be calculated from both slopes  $m_{(1)} = Q_E$  and  $m_{(M)} = Q_E F_n^2/M$  of the intensity-variance curves:

$$M = F_n^2 \frac{m_{(1)}}{m_{(M)}}. \quad (1.26)$$

In Appendix A.1 I present code to automatically measure data for this calibration. In order to cover a large span of gains, I capture a short exposure image before each measurement and use the longest exposure time that is possible without overexposing the sensor.

Table A.1 summarizes the calibration results. The average of the dark images (in ADU) is given in the column offset. The read noise in conventional mode is approximately 8 electrons per pixel rms. The column mean' (primed variable) contains the average number of photoelectrons per pixel in the illuminated image normalized by the integration time. The rows conv1 and conv2 with conventional readout (without EM-gain) contain approximately the same number. This proves that no significant bleaching occurred during the experiment.

### 1.4.5. Conclusion

In this section I discussed how various camera sensors work. I have explained photon shot noise, which follows from the quantum mechanical nature of light

## 1. Introduction

and so far constitutes a fundamental limit of light detection. Based on this, I explained a calibration method that helps to evaluate camera performance and, maybe more relevant for this work, allows comparison between images that were created with different microscopes.

Since low-noise active-pixel cameras became available only late during my project, and the first models still had some issues — unstable software or in the case of the Hamamatsu Orca Flash 2.8 too few outputs for trigger signals, I designed my system for EM-CCD. For most experiments, however, I used an interline CCD.

## 2. Methods for controlling illumination patterns

This chapter provides an overview of current methods of fluorescence microscopy that allow to produce a controlled distribution of the excitation light. I focus in particular on the techniques that prevent unnecessary illumination of out-of-focus structures and reduce phototoxicity.

### 2.1. Light sheet fluorescence microscopy

Light sheets can be directly created with separate optics to illuminate the sample from an orthogonal direction. Another promising method to create a sheet is to use a high numerical aperture objective near the total internal reflection angle. There is a trade-off between the sheet width and the field of view because both of these things are interrelated due to diffraction.

The idea of illuminating a sample from the side dates back quite far into the history of microscopy. Already one hundred years ago, an additional objective, arranged perpendicular to the detection objective, was used for illumination of the focal plane in the specimen. This dark field technique was used to characterize gold nano particles in gold ruby glass (Siedentopf and Zsigmondy 1903).

Eventually, this illumination method was also applied for fluorescence microscopy. First, it was used to analyze cochlea specimen (Voie et al. 1993) and, more recently, for the development of embryos (Huisken et al. 2004). Results in the latter paper have sparked interest in the technique at many labs (Santi 2011).

#### 2.1.1. Light sheet generation with cylindrical lens

Figure 2.1 shows how the light sheet can be focused into the specimen using a cylindrical lens. Huisken et al. (2004) employ a water dipping objective with long working distance (1...2 mm) and comparatively low NA for detection. A 10 $\times$  objective with 660  $\mu\text{m}$  field of view diameter is used with a sheet thickness that

## 2. Methods for controlling illumination patterns

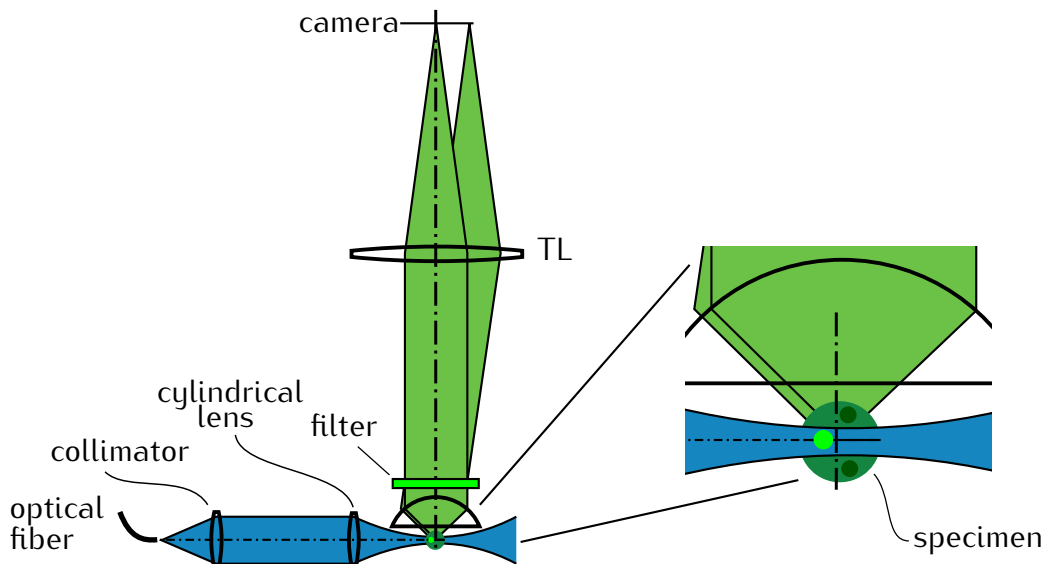


Figure 2.1.: Schematic of SPIM (selective plane illumination microscope). A cylindrical lens illuminates the specimen with a thin sheet of light along the focal plane of the objective. Rotating the sample and/or moving it along the axis allows reconstruction of a sectioned three-dimensional volume of the fluorophore concentration with improved light utilization compared to conventional microscopes (inspired by Huisken et al. 2004).

varies less than 42% ( $6 \dots 8 \mu\text{m}$ ). The light sheet not only improves sectioning and contrast, but also increases the axial resolution from originally  $14 \mu\text{m}$  by nearly a factor of two.

The axial resolution of detection objectives with higher numerical aperture isn't improved so easily over an extended field of view. Shading effects, diffraction and refraction can deteriorate the light sheet. As an improvement of the technique it was suggested to rotate the specimen or illuminate with multiple sheets of light from different directions.

A major difference between this technique and more conventional microscopy techniques is the way the sample is mounted. In a normal microscope, usually, a specimen is placed with a drop of embedding medium on a  $170 \mu\text{m}$  thick cover slip. Then it is flipped onto a microscope slide and sealed with nail varnish. This approach of mounting the sample does not work for an ultramicroscope because there the sample has to be accessed from two perpendicular sides. Often the specimens are embedded in an agarose cylinder or sometimes, they are fixed in a liquid-filled chamber.

## 2. Methods for controlling illumination patterns

### 2.1.2. Light sheet generation using the detection objective

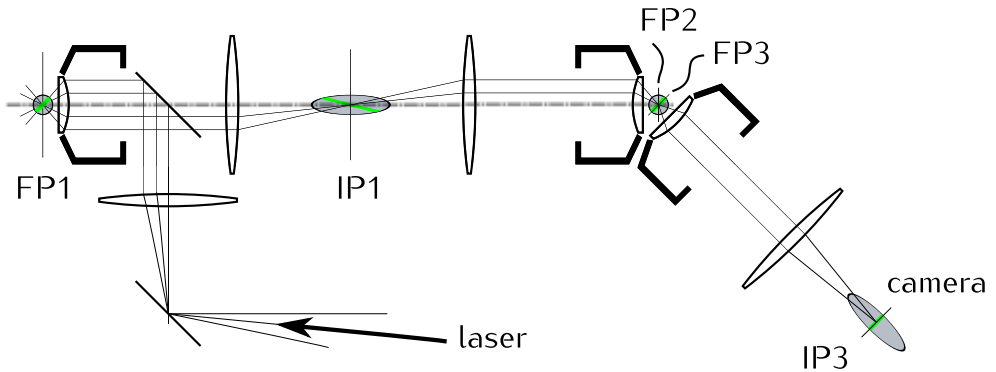


Figure 2.2.: Schematic of oblique plane microscopy (OPM). An index matched sample is excited using an oblique plane of light. The illuminated plane is tilted relative to the focal plane FP1. Therefore, out-of-focus fluorophores on the periphery of the field of view are excited as well. Two additional objectives in the detection path are used to reconstruct an aberration free image of all the excited fluorophores (drawing inspired by Dunsby (2008)).

Modern high numerical aperture objectives allow to illuminate an *index matched* sample with a half angle of up to  $70^\circ$ . This enables illumination of an oblique and thin sheet of light in the specimen just as in selective plane illumination microscopy. However this technique (oblique plane microscopy, OPM) has the advantage, that only one objective is used and therefore it will work with conventional microscope slides. However, one difficulty is that some of the excited fluorophores are severely defocused in the intermediate image plane (plane IP1 in Figure 2.2). Dunsby describes how to rotate the observational plane optically in order to recover an aplanatic image from the oblique illumination plane (Dunsby 2008). For this, they re-image the sample through two additional objectives.

Biological specimen are often not index matched and have a lower index  $n_e \approx 1.33 \dots 1.45$  than the immersion oil  $n = 1.52$ . As indicated in Figure 2.3, the refraction at the interface between cover slip glass and embedding medium can be exploited to illuminate the specimen with a light sheet that is nearly parallel to the focal plane. This technique is called highly inclined and laminated optical sheet microscopy (HILO) (Tokunaga et al. 2008; Konopka and Bednarek 2008).

Note that the index mismatch between embedding and immersion medium will introduce aberrations (mostly spherical) in the detection which will limit the useful imaging depth to a few microns for high aperture lenses.

## 2. Methods for controlling illumination patterns

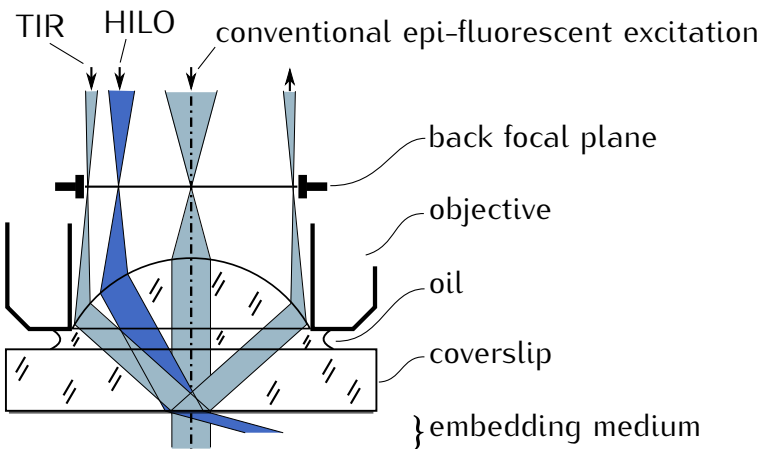


Figure 2.3.: Schematic of rays in HILO (highly inclined and laminated optical sheet) technique. The specimen is embedded in a medium of lower optical density than the immersion medium. For a very high illumination angle — corresponding to a point on the periphery of the back focal plane — the light would be reflected at the “cover slip-medium” interface due to the total internal reflection (TIR). For HILO, a point on the back focal plane slightly closer to the optic axis is illuminated. The light enters the embedding medium at a highly inclined angle and only a thin sheet in the focal plane is illuminated (inspired by Tokunaga et al. 2008).

## 2.2. Scanning techniques with improved light utilization

A confocal microscope exposes out-of-focus fluorophores with approximately the same dose as the in-focus fluorophores when producing an image of a focal slice. During acquisition of z-stacks this results in bleaching and successive slices contain less and less signal. In particular living organisms may be harmed due to phototoxicity during the observation.

Here I present two methods that can mitigate this effect. The first method is two-photon microscopy, in which the excitation is limited to the focal plane. Furthermore, there is controlled light exposure microscopy that selectively illuminates the sample depending on its structure. It delivers images with the overall quality as a conventional confocal while decreasing phototoxicity and bleaching considerably.

This method is based on a feedback that controls excitation dose depending on the local fluorophore concentration and therefore benefits from any latency improvements. In this context I discuss two approaches that can increase the scanning speed considerably.

## 2. Methods for controlling illumination patterns

### 2.2.1. Two-photon laser scanning fluorescence microscopy

If the laser intensity in the focal spot of a confocal microscope is sufficiently high, then two infrared photons can be absorbed within  $\sim 5\text{ fs}$  and excite the same electronic state.

In this regime, the fluorescence emission increases quadratically with laser intensity (Göppert-Mayer 1931). This non-linearity confines the excitation volume to the vicinity of the focal plane (Denk et al. 1990). Fluorophores outside of this region are not excited. Therefore this method produces sectioned images by default and there is no need for a detection pinhole.

As an additional benefit infrared light is scattered less than visible light of half the wavelength. This increases penetration depth and image quality. Photodamage outside of the focal volume is unlikely and phototoxicity is much lower, compared to the single-photon confocal microscope, when z-stacks are acquired.

However, the phototoxicity within the focal volume is higher and techniques like ultramicroscopy (section 2.1) with single-photon excitation are preferable, when low overall phototoxicity is a requirement.

### 2.2.2. Controlled light exposure microscopy (CLEM)

In the confocal microscope the excitation beam is scanned in a rectangular grid over the focal plane. Normally this is done using two galvanometer mirrors, one of which addresses pixel columns and the other (much slower) addresses the rows. The excitation laser is continuously active during a scan over one line. So ultimately, the integration time at the detector defines horizontal sampling.

The measured signal in each pixel is proportional to the collected photons and therefore subject to Poisson distributed quantum shot noise (see section 1.4.2). Thus, the signal-to-noise ratio fluctuates over the image. The image is particularly noisy in areas with low fluorophore concentration. For the human observer and many computer algorithms the noise in these particularly noisy areas defines the image quality. The fact that areas with more signal have considerably less noise does not increase the perceived image quality, neither does it improve the results of an edge detector for the dim areas. Considering the detrimental effects of the excitation light it would be advantageous to acquire fluorescence images with constant signal-to-noise ratio in each pixel.

This approach is pursued in the controlled light exposure microscope (CLEM). It utilizes a confocal microscope, adapted for fast switching of the excitation

## 2. Methods for controlling illumination patterns

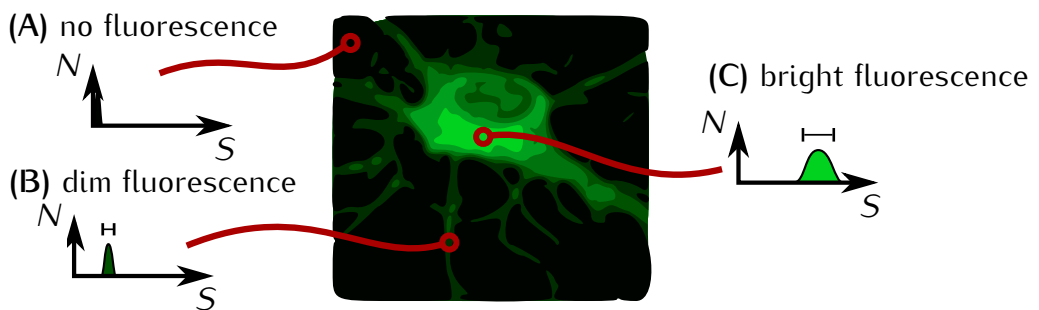


Figure 2.4.: Illustration of a typical fluorescence image of a neuronal cell and histograms for three different regions. In the conventional confocal microscope areas without fluorophores (A) and the areas with many fluorophores (C) are subjected to an unnecessarily high light dose. Controlled light exposure microscopy (CLEM) adapts the illumination to the sample in order to reduce phototoxicity and bleaching.

light. Depending on whether the photons collected during a short preparation time, each pixel is classified into one of three classes. The darkest pixels (class A in Figure 2.4) are assumed to not contain any information and the laser is switched off for the remainder of the dwell-time. Pixels with moderately many photons (class B) are illuminated for the entire dwell-time. For pixels with a high fluorophore concentration (class C) the excitation laser is turned off, once a certain number of photons have been detected. In this case the signal is not the number of photons but the illumination duration.

In this way, one obtains a picture in which bright regions have a constant signal-to-noise ratio and regions without fluorophores are illuminated with only a small dose. Especially when capturing z-stacks this procedure significantly reduces phototoxicity and photobleaching — with an insignificant decline in image quality.

The CLEM approach was first presented by Hoebe et al. in 2007, followed by an independent similar version with adaptive control of the laser power for 2-photon microscopy by Chu et al. (Hoebe et al. 2007; Chu et al. 2007).

### 2.2.3. Fast beam steering

In a conventional confocal microscope, the beam is steered by two galvanometer mirrors. While this technique offers very good light throughput the inertia of the mirrors limit the access rate of spots in the focal plane. The CLEM technique could be simplified and improved by an inertia-free solution to steer the excitation beam from pixel to pixel. The laser intensity would no longer have to be modulated and

## 2. Methods for controlling illumination patterns

when enough photons were collected in a pixel, the next one could be addressed.

The z-focus is often controlled by piezomechanical elements that either move the sample or the objective, i.e. objects of relatively large mass. Therefore, the settling time for focus movements has a correspondingly large latency and focusing is often much slower than lateral pixel access.

### Acousto-optic deflectors for fast beam steering

An interesting alternative to galvanometric mirrors are acousto optical deflectors (AODs). They consist of a transparent optical element into which an acoustic wave is coupled by means of an ultrasound transducer. An acoustic wave is a longitudinal variation of the interatomic distance and thereby affects the local electron density and thus the refractive index of the medium. An acoustic wave in an AOD allows diffracting a beam of light with moderate efficiency (70%). By changing the acoustic frequency the angle of diffraction can be controlled. Due to its strong chromatic aberration and low efficiency, an AOD should not be used to descans the beam of a normal confocal microscope. However, this device is well suited for a two-photon microscope, where descanning is not strictly necessary. In Otsu et al. (2008) the authors achieved a switching time of  $4 \mu\text{s}$  using an acoustic wave in tellurium dioxide ( $\text{TeO}_2$ ).

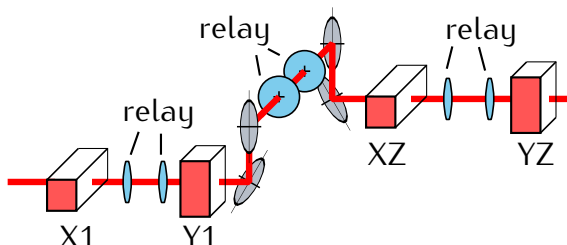


Figure 2.5.: Schematic of an acousto-optic deflector (AOD) illumination system with z-focusing. Drawing inspired by Reddy et al. (2008)

The system in Reddy et al. (2008) even uses an acousto optic technique to focus the excitation beam of a two-photon microscope (see Figure 2.5). A pair of two ultrasound transducers (e.g. X1 and XZ in the figure) produce two counter-propagating waves with continuously changing frequency. The resulting diffraction pattern resembles an one-dimensional Fresnel zone — oscillations of high frequency on the outside and low frequencies towards the center. A combination of two such elements but rotated by 90 degrees allows focusing the beam, similar to how two cylindrical lenses would (see Figure 2.5).

## 2. Methods for controlling illumination patterns

### Aberration-free optical refocusing

Achieving the resolution limit of modern microscope objectives using acousto-optic Fresnel zones seems impossible or at least very difficult. An alternative approach that can significantly speed up conventional focusing techniques is based on a similar technique as the oblique plane microscope (see section 2.1.2). In Botcherby et al. (2007) and Botcherby et al. (2012) an additional objective produces an unmagnified three-dimensional image of the sample which allows rapid refocusing with a lightweight mirror. This approach is achromatic and can focus many tens of microns deep into the sample while maintaining diffraction limited resolution. Unlike the acousto-optic device this method is not limited to a single collimated beam and can be applied in widefield microscopes.

## 2.3. Non-scanning techniques

### 2.3.1. Intensity modulation

#### Programmable array microscopy

The main element of the programmable array microscope is a digital micro mirror (DMD). It is placed into the intermediate image and acts simultaneously in the excitation as well as the detection beam path. The mirrors can be programmed to have one of two deflections. Either they send light into the sample or they send it into a beam dump. This allows structured illumination with a computationally defined pattern. In the simplest case, when only a single pixel is turned on, the operation of the PAM resembles that of a confocal microscope. Fluorescence light of in-focus fluorophores returns to the micro mirror that was responsible for the excitation and is directed towards the camera 1. Out-of-focus fluorescence will be reflected by any of the other DMD mirrors and ends up on camera 2.

At the time when Heintzmann et al. (2001) was written, EM-CCDs were not widely available. In order to reduce the effects of readout noise, cameras 1 and 2 integrate for a long time while the DMD displays many patterns. The pattern sequence could for example be a single pixel which scans the entire field. This would be very slow, so instead, patterns of a pseudorandom sequence are presented which significantly accelerates data acquisition, because each individual pattern excites more in-focus information. However, at the same time crosstalk is increased, i.e. additional light from out-of-focus fluorophores is collected in camera 1. The images from both cameras for z-stack acquisitions are reconstructed using

## 2. Methods for controlling illumination patterns

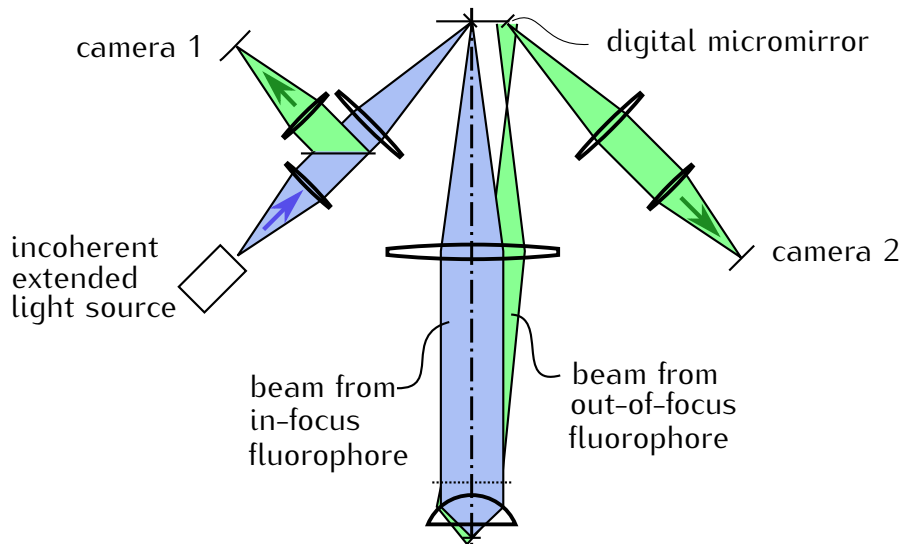


Figure 2.6.: Schematic of a programmable array microscope (PAM) (inspired by Verveer et al. 1998). A digital micro mirror device (DMD) containing an array of tiltable mirrors is imaged into the focal plane of the objective. Returning fluorescent light from out-of-focus fluorophores is distributed onto both cameras. In-focus fluorescence is only imaged onto the camera 1.

a maximum likelihood deconvolution.

A technique similar to controlled light exposure microscopy (CLEM, section 2.2.2) has been implemented in a programmable array microscope (PAM) (Caarls et al. 2011).

There are a few drawbacks with the programmable array microscope. First, diffraction losses at the DMD reduce detection efficiency. Second, if excitation light causes fluorescence or Raman scattering at the DMD surface, it is impossible to distinguish this disturbance from the fluorescence signal of the sample. Third, it is difficult to align the optics such that DMD pixels are imaged exactly and without distortion on camera pixels.

Distorted imaging could be retrospectively corrected by interpolation. However, this process would destroy the known noise characteristics of the sample values. The values in an interpolated image are no longer Poisson distributed and application of the maximum likelihood estimation is problematic.

With the availability of cameras with sub-electron readout noise (EM-CCD or sCMOS) one would no longer place the DMD in the detection path. Instead, one could acquire an image of each individual pattern and do the descanning computationally.

## 2. Methods for controlling illumination patterns

### 2.3.2. Direct illumination

An obvious method for doing spatial control is to image a two-dimensional array of high-power micro-LEDs into the specimen. However, the problem is to achieve

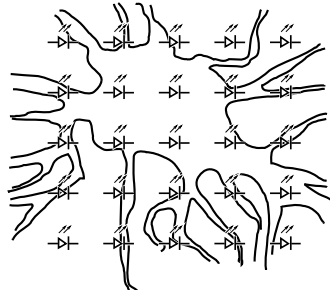


Figure 2.7.: Schematic of a micro-LED illumination array and the outline of a neuronal cell, inspired by Grossman et al. (2010).

sufficient *irradiance* and *fill factor*. The angular emission profile of LEDs is often Lambertian, i.e. the back focal plane of the objective would be over-illuminated and a lot of light would be lost. The fill factor is limited because it is difficult to put a lot of LEDs close to each other. The technique has been demonstrated using a  $64 \times 64$  array of  $20\text{ }\mu\text{m}$  micro-emitters with  $50\text{ }\mu\text{m}$  pitch (Grossman et al. 2010) (see Figure 2.7). The LEDs can be switched at millisecond speed and emit at a wavelength of  $(470 \pm 22)\text{ nm}$ .

Currently it is not clear whether direct illumination will ever replace the more flexible spatial light modulators. Manufacturers of direct illumination devices will optimize their technology for consumer applications such as mobile phone displays, where neither fill factor nor extreme radiant intensity ( $\text{W}/\text{sr}$ ) are very important. Arrays of Vertical-cavity surface-emitting lasers (VCSEL) may become interesting alternatives to LED-arrays because they can provide high radiant intensity, but currently they are not readily available in the interesting wavelength ranges.

### Light field microscopy

Interesting work on light fields originally started in the macroscopic domain of cameras (Lippmann 1908) and was eventually applied as a technique for microscopy (Levoy et al. 2006, 2009; Zhang and Levoy 2009). This approach is built on imaging through an array of microlenses.

Downstream of the microlenses a spatial light modulator (SLM) is placed, so that a rectangular group, of say  $10 \times 10$  pixels is imaged into the pupil. Each microlens illuminates the pupil from another angle. In Levoy et al. (2009) they use

## 2. Methods for controlling illumination patterns

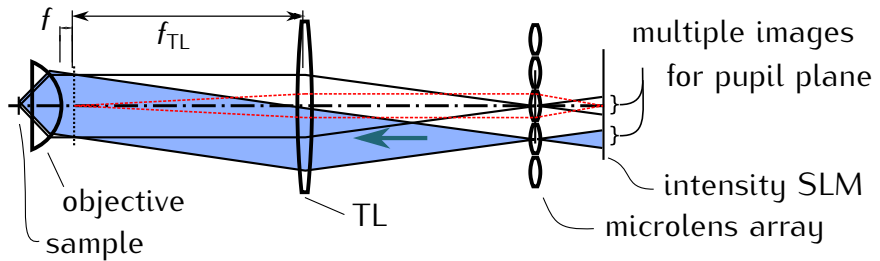


Figure 2.8.: Schematic of microlenses in the intermediate image plane (inspired by Levoy et al. 2006). A spatial intensity modulator is illuminated from the right with an extended light source. Groups of neighboring pixels downstream of individual microlenses are imaged into the pupil. Therefore these pixels allow to control the irradiance in the sample at the area that is conjugated to the microlens.

an intensity SLM and each of its pixels controls the radiant intensity (W/sr) in the area of the sample that is covered by the conjugated image of the corresponding microlens. A trade-off has to be made between the resolution that can be obtained in the pupil and the resolution in the focal plane in the sample. The latter is limited by the size of the microlenses.

The paper uses microlenses in the detection path as well. The camera captures a lot of images of the pupil. This allows retrospective refocusing or rotation of the image using the ray-based plenoptic theory. However, splitting the images with microlenses has severe drawbacks and should not be used with fluorescence microscopy. When recording camera images, important phase information is lost and the sub-images can not be recombined to obtain the full resolution of the microscope objective.

In the case of illumination the loss in resolution is not as important and perhaps the full resolution could even be maintained when a phase SLM is used.

### 2.3.3. Temporal focusing

The axial extent of ultra-short laser pulses can be as thin as a few microns. A collimated beam can be split into different spectral components by a grating in the intermediate image plane (Oron et al. 2005). The tube lens focuses the diffraction pattern into a line in the back focal plane of the objective.

The objective, which has to be corrected for chromatic aberration and dispersion, then focuses all the beams onto the focal plane. Different spectral components arrive in the focal plane at the same time. The out-of-focus points see an extended illumination. For a high NA objective, a pulse duration of  $\tau = 20\text{ fs}$  results in slice

## 2. Methods for controlling illumination patterns

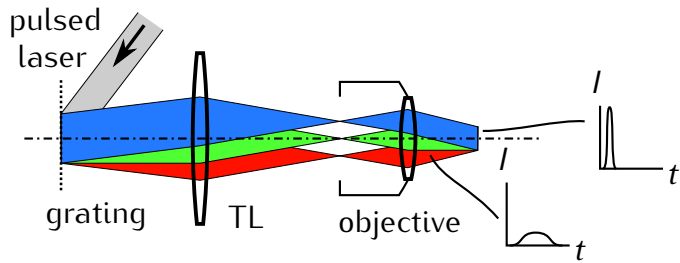


Figure 2.9.: Schematic of temporal focusing (inspired by Oron et al. 2005). A grating in the intermediate image plane separates the pulse into its spectral components. The out-of-focus areas of the specimen are illuminated with a longer pulse. Only in the focal plane, all spectral components interfere coherently and form a short intensive pulse.

of  $z \approx \tau c/2 \approx 3 \mu\text{m}$  thickness around the focus, where the beam has significant intensity.

Using this technique it is possible to build a widefield 2-photon microscope that only excites fluorophores within the focal plane. The technique can be further improved by spatially modulating the beam in the intermediate image plane for CLEM like performance. This technique has been implemented in the TF-GPC approach and will be discussed in the next section.

### 2.3.4. Phase modulation

#### Digital holography

Certain types of liquid crystal spatial light modulators can be used to modify the phase of light. When such a device is placed into the back focal plane of a lens, it is possible to control the light distribution in its front focal plane. An iterative algorithm (iterative Fourier transform algorithm, IFTA) can be used to establish a phase image on the liquid crystal display that will result in an intensity distribution in front of the lens.

This approach has been used to excite a two-dimensional pattern in the specimen (Lutz et al. 2008; Zahid et al. 2010) and is advantageous especially for cases where only small parts of the specimen ought to be illuminated. As opposed to conventional intensity spatial light modulators, the light can be redirected from dark areas into the bright areas.

There is also a limited possibility to create three-dimensional patterns, e.g. several points below, in and above the focal plane by displaying Fresnel zone planes. For illumination, usually a laser with non-zero interference length is employed. However, this illumination contains an unwanted “speckle” pattern

## 2. Methods for controlling illumination patterns

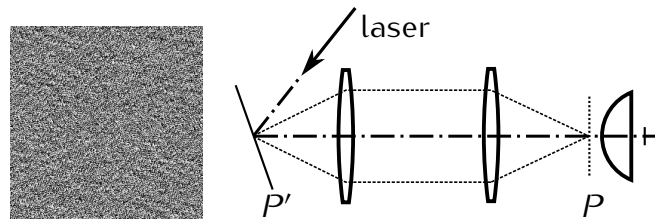


Figure 2.10.: Schematic of spatial illumination by phase holography. A phase-only SLM displays a hologram in the plane  $P'$  which is conjugated to the back focal plane  $P$  of the objective (inspired by slide from V. Emilian).

in the form of noisy non-uniformities. To a certain extent, the contrast of the speckle pattern can be reduced by controlling spatial and temporal coherence of the illumination (sweeping the frequency of the laser or changing illumination direction while the detector is integrating).

Holographic control can be used with 2-photon excitation as well (Nikolenko et al. 2008), but this exacerbates the effect of speckles.

### Generalized phase contrast (GPC)

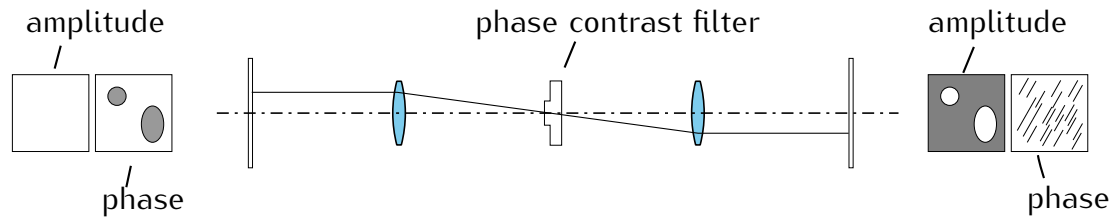


Figure 2.11.: Schematic of generalized phase contrast (inspired by Rodrigo et al. 2008).

A phase contrast microscope objective can be used to convert a phase image from the intermediate image plane into an intensity image in the specimen (Rodrigo et al. 2008). Compared to digital holography, hardly any computation is necessary. Yet, the phase spatial light modulator can concentrate a lot of light on a small region of the specimen as opposed to other techniques, which involve intensity modulation and lose all the light of dark areas by sending it into a beam block or something similar.

The generalized phase contrast method is suitable even with spatially incoherent illumination. However, when the fill-factor – the size of the bright area in the image – changes, the phase contrast filter must be changed.

## 2. Methods for controlling illumination patterns

### Generalized phase contrast and temporal focusing (TF-GPC)

The combination of generalized phase contrast and temporal focusing allows spatially controlled illumination of in-focus areas (Papagiakoumou et al. 2010). Usage of a phase spatial light modulator results in high light efficiency compared to intensity modulation. Splitting and recombination of the spectral components of the pulse reduce speckle noise considerably.

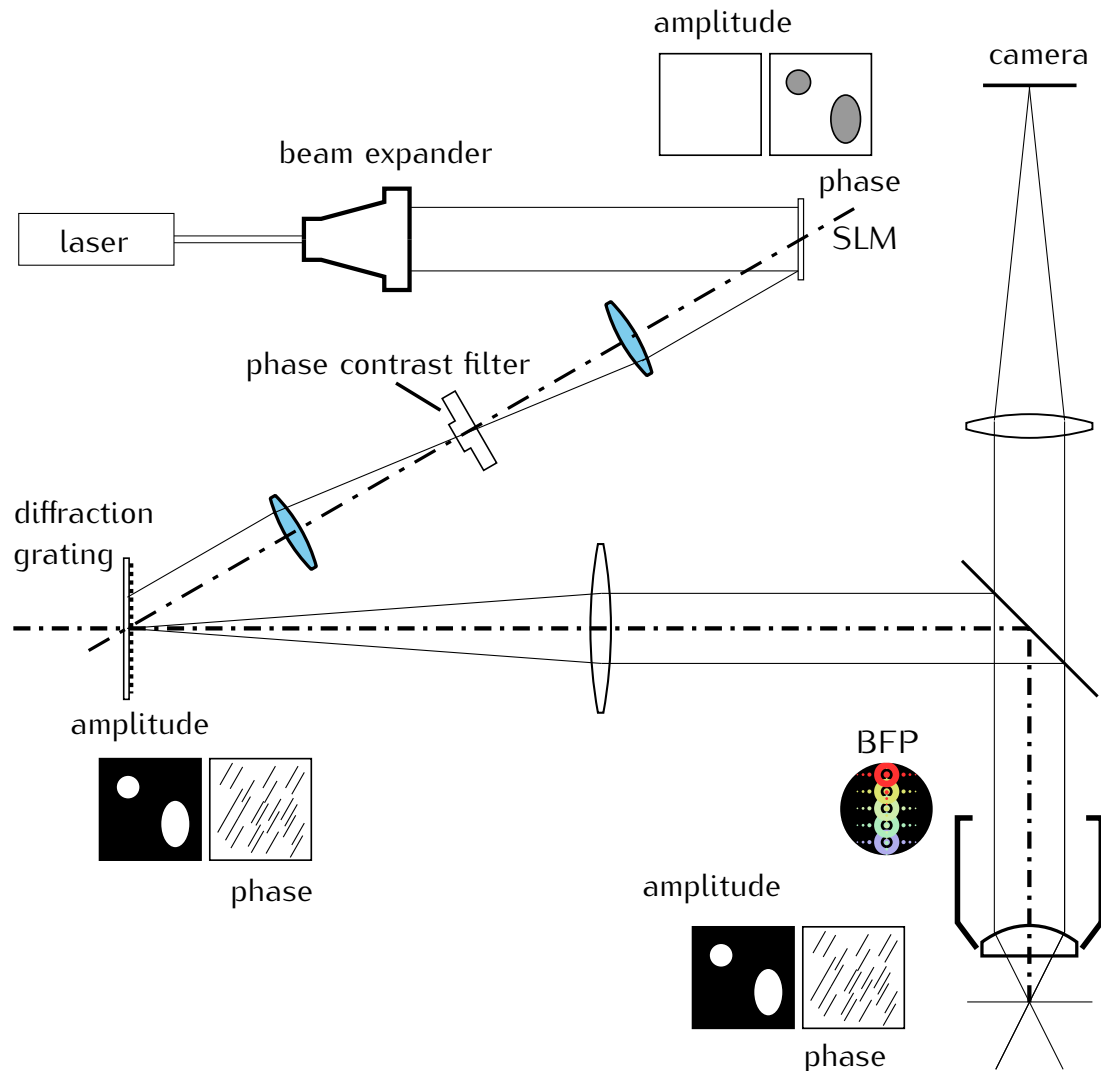


Figure 2.12.: Schematic of phase contrast with temporal focusing (TF-GPC) (inspired by Papagiakoumou et al. 2010), PCF is a phase contrast filter.

### 3. The concept of spatio-angular microscopy

Here I introduce spatio-angular microscopy. First I explain the concept of its illumination system using exemplary fluorophore distributions, that occur in typical specimen.

Then I describe some decisions we faced during the initial design phase concerning the arrangement of optical components. Furthermore, I position our method among known approaches of light control for microscopy. Of all published techniques for excitation illumination control, the light field microscope (Levoy et al. 2006) comes closest to our approach. I explain differences between both techniques and discuss their respective pros and cons. I address the peculiarities and limitations of the hardware components in chapters 4. Initially, the details would be detrimental to clarity.

The effective use of the spatio-angular microscope, requires more knowledge about the specimen than a conventional or a light-sheet microscope (Siedentopf and Zsigmondy 1903; Huisken et al. 2004). Ideally, the distribution of refractive index and fluorophores in the specimen should be known. If these parameters were precisely known, there would be no need for an image in the first place. However, while imaging a known specimen, sufficiently good predictions of these parameters can often be made. The higher the accuracy of these prognoses, the greater the reduction in phototoxicity will be.

The computer-based selection of appropriate illumination masks requires model prediction, or at least an approximate estimation, of the three-dimensional distribution of light in the specimen as well as knowledge about the fluorophore distribution.

In the last part of this chapter, I describe the computational control loop in our spatio-angular microscope and touch topics of image processing.

#### 3.1. Motivation

In order to introduce the basic idea underlying the spatio-angular microscope, I consider the distribution of excitation light in the object of a conventional

### 3. The concept of spatio-angular microscopy

fluorescence microscope: Figure 3.1 a) schematically illustrates the side view of the excitation beam path through objective lens and object in a confocal microscope. A collimated beam with a circular cross-section (this cross-section is not shown in the illustration) passes through the lens. The lens focuses the light in its focal plane.

Between lens and focal plane the light rays form a convergent circular cone. If refractive index variations in the object are negligible, the light distribution below the plane of focus forms a cone as well, due to symmetry. Assuming a non- or weakly absorbing specimen, the energy of the light in the circular cross-sections of the cone remains constant<sup>1</sup>.

The fluorescent bead (1), in the focus, would therefore be excited significantly more than the bead (2) outside the focal plane. Also shown is the light distribution in the intermediate image plane.

The image of the in-focus bead (1) is sharp, i.e. its emanating fluorescence light is concentrated on an area as small as possible and positioned exactly on the detection pinhole. Conversely, the image of the out-of-focus bead (2) is blurred and its fluorescence light is distributed over a large area.

While only a tiny proportion of the light emitted by the out-of-focus bead contributes to the detection signal of the confocal microscope—and therefore hardly affects the image quality, with respect to overall phototoxicity of the full confocal system—it would be better to prevent the excitation of the out-of-focus bead in the first place.

The scheme in Figure 3.1 b) demonstrates how the light cone would have to be manipulated in order to exclude the out-of-focus bead (4). The expected fluorescence image in the intermediate image plane then contains only information from the in-focus bead (3).

Viewed from the in-focus bead (3) the change in illumination corresponds to a restriction of the light angles. Such control can be exerted well through a mask in the other focal plane of the objective lens (also denoted back focal plane or pupil plane).

---

<sup>1</sup>The ray-model is valid in large parts of Figure 3.1 a), but not everywhere. The Law of Malus–Lupin states that rays and wavefronts are equivalent as long as rays do not intersect (caustic), or a strong intensity gradient occurs. Thus the ray-model is valid almost everywhere in the cone, except for a region with a distance of a few wavelengths to the edge, and the focus itself. While the wave-optical treatment of these areas is possible, it is computationally much more expensive than ray tracing. Wave-optical effects either lead to blurring in a length scale of a few wavelengths or intensity fluctuations due to interference (Stokseth 1969). If necessary, we can use heuristics to find an upper bound for the local intensity from ray tracing results. For this reason we exclusively employ the ray-model in this work.

### 3. The concept of spatio-angular microscopy

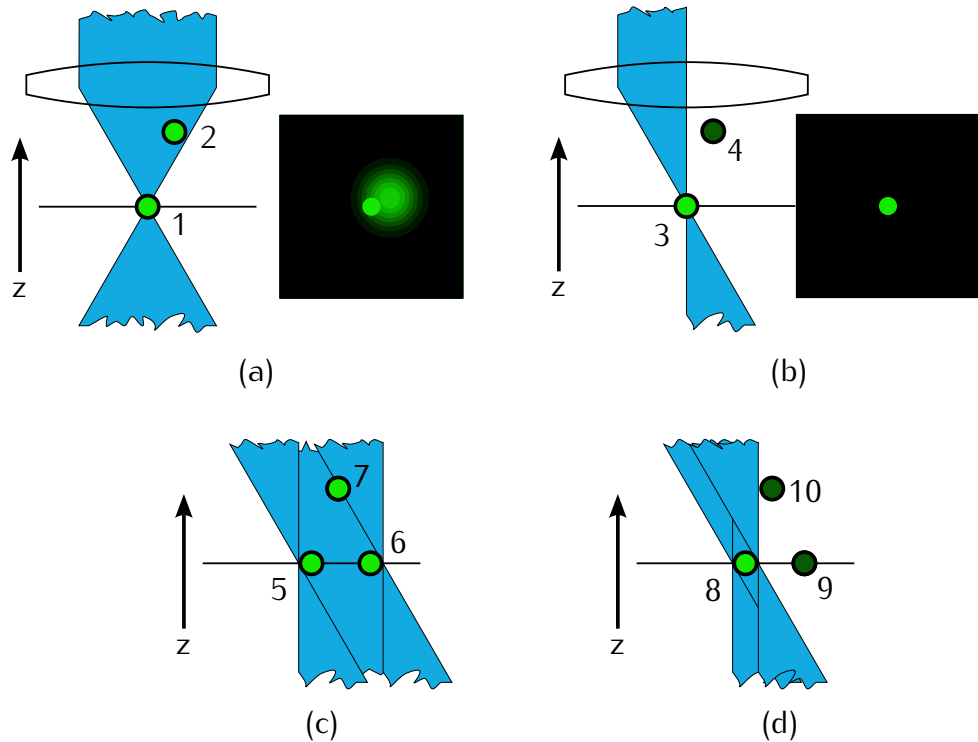


Figure 3.1.: (a) Two fluorescent beads are illuminated by all angles that the objective can deliver. The sharp image of the in-focus bead is deteriorated by blurry fluorescence of the out-of-focus bead (2). (b) Angular control allows selective illumination of the in-focus bead (3), and results in a better image on the camera. (c) Angular control, however, is insufficient, when an extended in-focus area is illuminated. (d) Then, simultaneous spatial and angular control can sequentially excite the in-focus beads, while excluding the out-of-focus bead (10).

Thus it is useful and possible to equip a confocal microscope with angular control. However, in our project we set out to build a wide field microscope in order to benefit from the speed and quantum efficiency of modern cameras.

I now turn to the task of bringing angular control to the widefield microscope. Figure 3.1 c) shows a configuration of the specimen with two in-focus beads (5) and (6), and one out-of-focus bead (7). The angular illumination control is ineffective for this arrangement of beads. If both in-focus beads, (5) and (6), are exposed simultaneously, i.e. an extended light source illuminates the entire field, then the out-of-focus bead (7) is always excited.

Only by separate illumination of the in-focus beads (8) and (9), as shown in Figure 3.1 d), angular control regains its function. For this reason a widefield system with angular control, using a mask in the pupil, requires an additional mask conjugate to the field. Therefore, we call our method spatio-angular microscopy.

### 3. The concept of spatio-angular microscopy

"Spatial" refers to the illumination control in the field and "angular" refers to the control in the pupil plane.

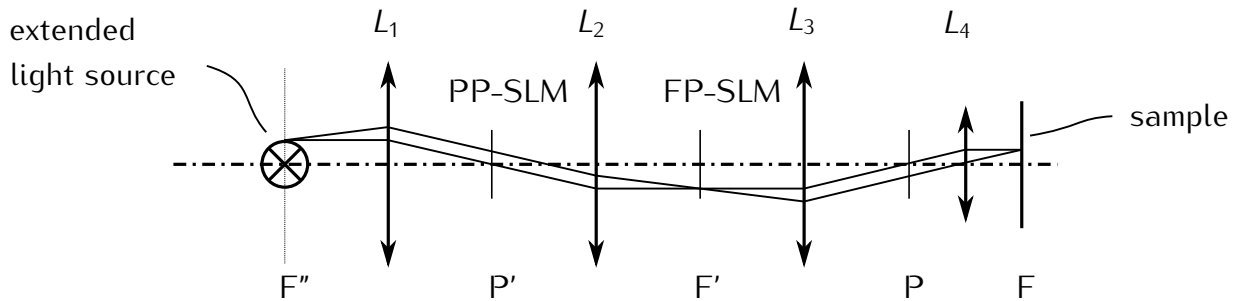


Figure 3.2.: Simplified schematic of the illumination system in our spatio-angular microscope. A homogeneous extended light source delivers light from the left. It is imaged by lenses  $L_1$  and  $L_2$  into the intermediate image  $F'$ . Then the tubelens  $L_3$  and the objective  $L_4$  form an image of  $F'$  in the sample plane  $F$ . We use two spatial light modulators (SLM) to control the spatial and angular light distribution in the specimen—the focal plane SLM in  $F'$ , and the pupil plane SLM in  $P'$ .

Figure 3.2 shows the optical path through our prototype in a simplified form. From the left side, an extended light source illuminates the system. A sequence of confocal lenses  $L_1$ ,  $L_2$ ,  $L_3$  and the objective lens  $L_4$  image the light source from  $F''$  into the front focal plane (indicated by  $F$ , for field). The etendue (see page 29 for its definition) of the light source must be large enough to simultaneously fill both the pupil  $P$  as well as the field  $F$ .

In each of the two planes  $P'$  and  $F'$  we place a spatial light modulator (SLM) that controls the intensity of the transmitted light.

Looking at the scheme in Figure 3.2, one might argue that we could save a lens, if we placed the pupil plane SLM into  $P$  instead of  $P'$ . There are three reasons why this is neither possible, nor beneficial: First, the pupil of modern high-performance objective lenses is typically not accessible. Second, the detection path for fluorescent light should contain as few optical components as possible and we can definitely not afford it to be blocked by a SLM. Third, the two masks induce difficult to predict, filtering of spatial frequencies. An analysis requires consideration of partial spatial coherence, but even without a thorough simulation one may assert that the downstream<sup>2</sup> SLM will always deliver a good image, mostly independent of the state of the SLM upstream.

Considering the fact that the image of the focal plane SLM is most important to us, we decided to place it downstream of the pupil plane SLM. The focal plane

---

<sup>2</sup>Downstream regarding the propagation direction of the excitation light.

### 3. The concept of spatio-angular microscopy

SLM may disturb the image of the pupil plane SLM in P, but we can always produce very fine, high-contrast structures in the sample F.

The ability to achieve high resolution in the field is the main difference between our approach and Levoy's light field microscope. In the light field microscope, the density of the microlenses noticeably limits the resolution. As opposed to our system, the light field microscope allows control of the angle of incidence in all field positions independently. But, additionally to the reduced focal plane resolution, this requires a single high-resolution SLM with a comparatively low refresh rate. We use two small SLMs, which can each achieve 1 kHz frame rate and enable interesting experiments, e.g. optogenetic control of neuron activities.

## 3.2. An imaging protocol with spatio-angular illumination control

### 3.2.1. Description of an exemplary biological specimen

I now refer to the *C. elegans* test sample for phototoxicity that I introduced in section 1.1. So far I did not reach the point of being able to image the development of a real embryo. Key problems are the low light throughput of the illumination system and the length of time necessary to update images on the focal plane display. Nevertheless, I always kept this example in mind while I was developing the control software for our microscope.

During the first few hours, the embryo develops confined within the constant volume of its egg, which has an ellipsoidal shape, extends 40 to 60 microns and can be readily observed using a 63 $\times$  objective lens. Cell divisions occur every few minutes. During development the nuclei get smaller and more dense. In order to track the fate of all individual cells it is sufficient, to capture one stack per minute with 41 layers and a z-step of 1 micron.

### 3.2.2. Preparation of living embryo samples

For an experiment a hermaphrodite worm is cut and the embryos are placed on an agarose pad, so that they stay immobile during imaging. This procedure is explained<sup>3</sup> in Hope (1999). Of these embryos, the experimenter chooses a young specimen, that has not yet divided. We avoid using fluorescence excitation for

---

<sup>3</sup>Note that Murray et al. (2006) describes an improvement of this protocol that prevents squeezing the embryos too much.

### 3. The concept of spatio-angular microscopy

this step. The undivided embryos can be distinguished using the less phototoxic differential interference contrast (DIC) imaging mode.

#### 3.2.3. Sectioning through structured illumination

To get an estimate of the initial distribution of the fluorophores in the embryo I obtain the very first stack with structured illumination and no angular control. I use this method to avoid the missing cone problem of the widefield microscope. Perhaps for our particular task of finding the position of one nucleus within the egg, widefield images would be just sufficient. However, for our spatio-angular method, knowledge about the three-dimensional fluorophore distribution is very important and therefore we built our microscope such that we can obtain optical sections.

We compared conventional structured illumination using conventional max–min reconstruction with laser and LED illumination. Although LED illumination resulted in excellent optical sections, the reconstruction of laser illuminated images contained artifacts.

Therefore, we decided to implement the HiLo algorithm for optical sectioning (see Appendix B). With this algorithm, we obtain artifact-free optical sections, regardless of the illumination source. As another advantage the HiLo method increases acquisition speed, because only two raw images per slice are necessary. Please note, that this algorithm should not be confused with Tokunaga's HILO illumination technique from section 2.1.2.

#### 3.2.4. Computer model for the integration of a priori knowledge about the biological events

Given an initial measurement of the fluorophore distribution of the embryo, I employ a computational algorithm to find good illumination conditions for subsequent stack acquisitions. An important requirement is that the computer can estimate, which areas of the sample should be protected from illumination.

For our test system, the *C. elegans* embryo, it is a promising approach to represent its three-dimensional fluorophore distribution by a simple model: Spheres encompassing the nuclei, indicate regions with fluorophores. When in focus, the spheres are the source of useful, informative fluorescence signal, but should be protected against exposure when out of focus.

As mentioned earlier, there are also unused histones with fluorophores outside

### 3. The concept of spatio-angular microscopy

of the nuclei. The images reveal that they occur in the cytoplasm at a much lower concentration than in the nuclei. Fluorophores in the cytoplasm have a smaller phototoxic effect, because any radicals they produce are much less likely to reach the DNA and therefore inflict substantially less damage. In the following my goal is to protect only out-of-focus nuclei from exposure. The regions in between are used to bring the light in.

During observation, the nuclei, i.e. the centers of the spheres, move slowly within the embryo. For small periods of time we can describe this movement using a vector field of growth velocities.

A cell division announces itself by a change of the fluorophore distribution of the nucleus due to chromatin condensation and spindle formation. Therefore, whenever the computer detects such changes in the images, in one of the following time steps an additional sphere should be introduced to account for the new daughter cell.

So far I have implemented a simple algorithm, to convert a time series of image volumes from a confocal microscope into a sphere model (Santella et al. 2010). One of our project partners (Jean-Yves Tinevez, <http://fiji.sc/wiki/index.php/TrackMate>) developed a more sophisticated plug-in for ImageJ, that provides the lineage tree and snapshots of the developing cells (see Figure 3.3). Before our microscope can be used for our biological problem, the computer model has to be extended so that it reliably tracks the movement of nuclei. Overlooking any nucleus would prevent this nucleus from being imaged in later acquisitions and would be a setback for the experiment. Estimating the vector field of growth velocities helps to track nuclei more robustly and allows prediction of their positions for the next exposure.

Currently we have not implemented programs that would fulfill the requirements for imaging a developing embryo. However, in the following text I assume that the described position predictions were available and I discuss how I determine masks for the focal plane and pupil plane SLM.

#### 3.2.5. Illumination optimization by means of raytracing

I now discuss a method to find both SLM masks for image acquisitions with minimal phototoxicity. First I define a mask for the focal plane SLM:

From the predicted arrangement of spheres we select in-focus nuclei by intersecting the model with a planar surface. I then define focal plane SLM masks to selectively illuminate each of the in-focus nuclei, by drawing a bright disk in the

### 3. The concept of spatio-angular microscopy

appropriate position.

Based on such a mask, we can determine which angles can illuminate the in-focus target nucleus, without exposing out-of-focus nuclei.

As I already explained at the beginning of this chapter on page 55, ray-optical theory suffices to describe the light distribution within the sample.

I connect the periphery of an out-of-focus nucleus with a point inside the in-focus target. This defines a circular cone of rays, that are propagated through the objective lens. Their intersection with the pupil plane results in a figure that still very much resembles a circle—I found that already seven rays lead to good representation of its perimeter. An algorithm computes these figures for every out-of-focus nucleus and for a few in-focus targets points within the bright areas of the focal plane pattern. In this manner I construct the desired mask for the pupil plane SLM.

In order to trace the rays into the pupil, I need the design parameters of the objective lens (vertex position, curvature and material for all surfaces). Unfortunately, these rarely are publicly available for high-performance objective lenses. Nevertheless, in chapter 5 I use a simpler model of the objective lens, that requires only three parameters: focal length, refractive index of the immersion medium and numerical aperture. These are always known.

Additionally, I have adapted the model for non index matched embedding of the specimen. This problem occurs when the embryo is illuminated with an oil immersion objective, using HILO (Tokunaga et al. 2008). It should be noted, however, that good image quality of the embryo can only be achieved with an objective lens that has the same immersion index as the embryo. Otherwise data from 20 microns within the sample will be severely deteriorated by spherical aberrations.

### 3. The concept of spatio-angular microscopy

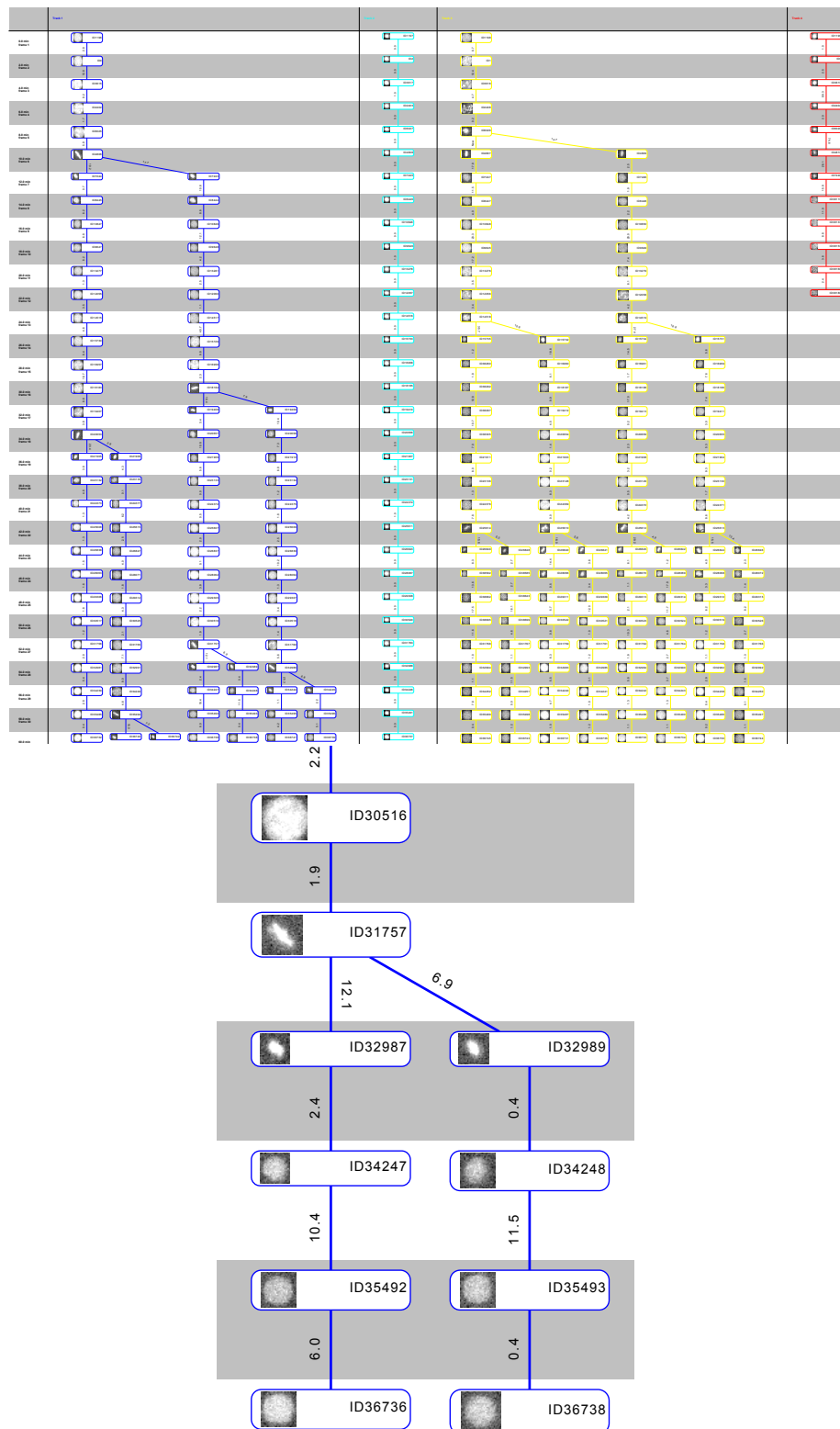


Figure 3.3.: Lineage tree of a developing *C. elegans* embryo, visualized in TrackScheme. An image of each nucleus is shown in each time step. Note the elongated structure of the nucleus before the cell division event.

# 4. Description of our prototype for spatio-angular illumination

In the preceding chapter I showed the underlying concept of our spatio-angular microscope. Here I discuss additional details that are important for the practical implementation.

I explain the beam path, electronic synchronization of the displays with other components and an algorithm to transform the coordinate system of the camera pixels into the coordinate system of the focal plane SLM.

The pupil plane SLM was specifically developed for our project by our partner Fraunhofer IPMS (Dresden, DE).

## 4.1. Description of the optical components

In the preceding chapter I have shown the beam path for transmissive displays (in Figure 3.2). Such SLM have a very low transmission in practice. Therefore we use reflective displays in our prototype.

In Figure 4.1 I adjusted the beam path accordingly. This schematic also depicts the optics we use to adapt light from the laser to fill the etendue of our system. The light source enters the system from the bottom left. The optic components are color corrected and have anti-reflection coating for wavelengths in the range from 400 nm to 700 nm.

The system successively illuminates the pupil plane SLM — a greyscale micro mirror array developed by our project partner Fraunhofer IPMS Dresden — and the focal plane SLM, a commercial binary liquid crystal on silicon display.

### 4.1.1. Ensuring homogeneous illumination

A quantitative evaluation of our experiments (section 6) with different illumination patterns is simplified when both pupil plane SLM and focal plane SLM are

#### 4. Description of our prototype for spatio-angular illumination

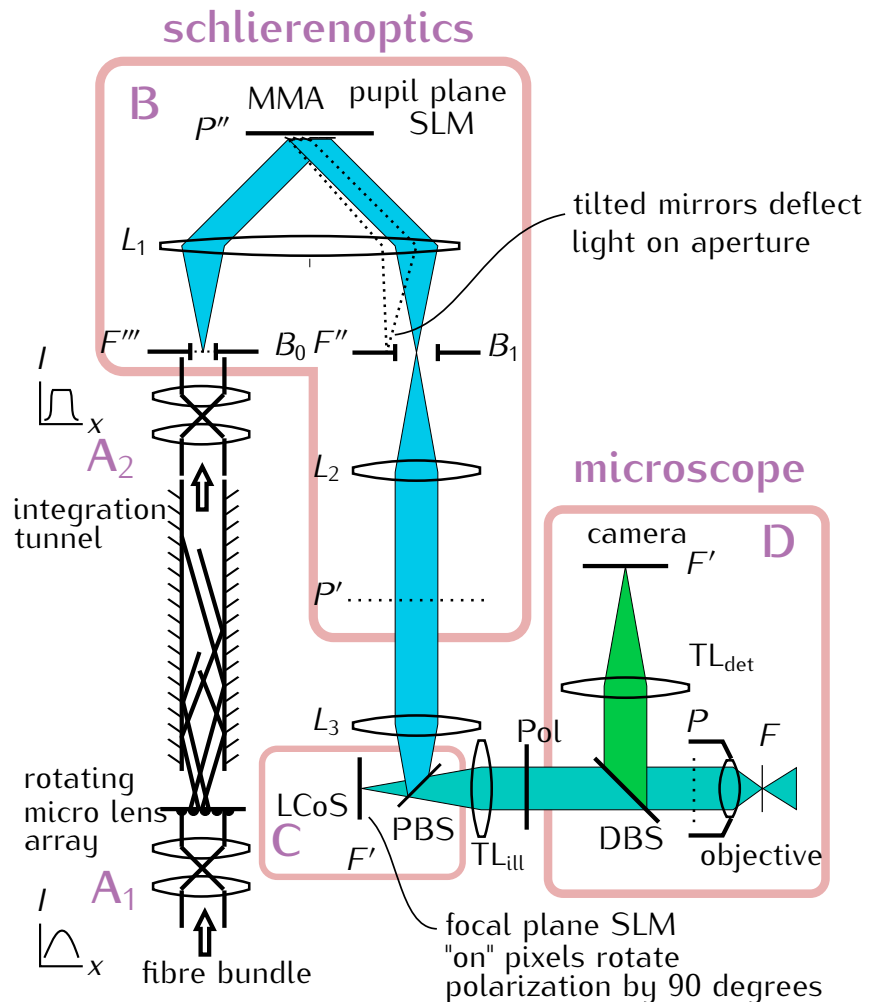


Figure 4.1.: Schematic of the light path through our microscope. Laser light enters from the lower left, is scrambled and homogenized to illuminate the pupil plane SLM in  $P''$  and the focal plane SLM in  $F'$ .  $F$  is the field plane in the sample and its primed versions are conjugated planes.  $P$  is the pupil of the objective. Field mask  $B_0$  and Fourier stop  $B_1$  are adjustable circular apertures. PBS is a polarizing beam splitter. DBS is a dichromatic beam splitter. The red boxes delineate subsystems of the illumination system: **A<sub>1</sub>** and **A<sub>2</sub>**: light scrambling and homogenization, **B**: Fourier-optical filter to provide intensity modulating pupil plane SLM. **C**: Polarization based intensity modulator as focal plane SLM. **D**: Wide-field fluorescence microscope with detection path.

#### 4. Description of our prototype for spatio-angular illumination

uniformly illuminated. Below we discuss an optical setup that attains homogeneity of the illumination of both displays.

We use either a laser<sup>1</sup> or a light emitting diode (LED) as the light source in our experiments. The LED<sup>2</sup> we use has a large active area. Due to etendue mismatch a relatively large amount of light will never reach the sample. However, it is easy to achieve a homogeneous illumination with an LED. Moreover, the LED can be quickly switched on and off electronically. Nevertheless, it would be better to use an LED with a smaller active area but those are hard to find.

Unlike an LED, a laser delivers light of considerably higher spectral radiance ( $\text{W}/(\text{sr m}^2\text{nm})$ ). Thus it is in principle possible to use the laser as a highly efficient light source for our system. Unfortunately, the high spectral and spatial coherence of a laser often leads to high-contrast fluctuations of the irradiance and we have to compensate for this by time averaging.

When using the laser, we send its collimated Gaussian beam into a bundle<sup>3</sup> of randomly distributed fibers. This randomizes the light distribution at the bundle output and also broadens the illumination angles.

A relay system ( $A_1$  in Figure 4.1) images the circular output of the fiber bundle onto the entrance of a light pipe. This relay system contains a rotating microlens array<sup>4</sup>. It is driven by a motor with the axis of rotation displaced from the optical axis. Integrating sufficiently long over the time-variations in the intensity pattern allows reduction of speckle.

Both the fiber bundle and microlens array increase the etendue of the laser illumination to the optimum value, which is given by one of our SLMs as discussed on page 72.

The integration tunnel shown in Figure 4.2 is hollow and has a quadratic cross-section. The mixing effect of the tunnel can be understood by considering the irradiance in the plane of the tunnel output as it would occur without the tunnel. Drawing the outline of the square cross-section into this irradiance map selects the light that reaches this plane directly without any reflection. Surrounding this outline with four identical copies that touch its edges selects the light that will reach the output plane after one reflection. The irradiance maps from neighbouring squares are mirrored and added to the direct illumination.

---

<sup>1</sup>Lasever LSR473H, diode-pumped solid state laser, output power 600mW,  $\lambda = 473 \text{ nm}$

<sup>2</sup>Huey Jann HPB8-48KBD, wavelength  $(463 \pm 1) \text{ nm}$ , brightness 35 lm, view angle 120°

<sup>3</sup>Fiber bundle with circular cross-section (Loptek, Berlin, DE), 1.1 mm diameter and 2 m length.

The beam broadening is 3° and increases, when the bundle is bent (Ipp et al. 2009).

<sup>4</sup>Array of cross-oriented cylindrical lenses on both sides with a pitch of 0.5 mm resulting in an effective focal length of 6.9 mm (LIMO, Dortmund, DE).

#### 4. Description of our prototype for spatio-angular illumination

Depending on the numerical aperture of the input light, more reflections may occur — resulting in the addition of irradiance from next-nearest-neighbours.

This integration tunnel improves the uniformity of the light distribution in the output plane without altering the numerical aperture of the light. The more subregions are superimposed, the better will be the uniformity of the illumination. Assuming  $N$  subregions were overlaid and their contributions were statistically independent, then according to the central limit theorem the standard deviation of the irradiance is proportional to  $1/\sqrt{N}$  (Koshel 2012). We also align the source distribution to be rotationally symmetric about the optical axis and obtain an even more uniform output because positive and negative slopes from different subregions compensate in the superposition.

The dimensionis of the integration tunnel in our sytem is  $2.5\text{ mm} \times 2.5\text{ mm} \times 250\text{ mm}$  and ensures enough reflections for homogeneous illumination. A relay system magnifies the tunnel output to  $4\text{ mm} \times 4\text{ mm}$  in the plane  $F''$ .

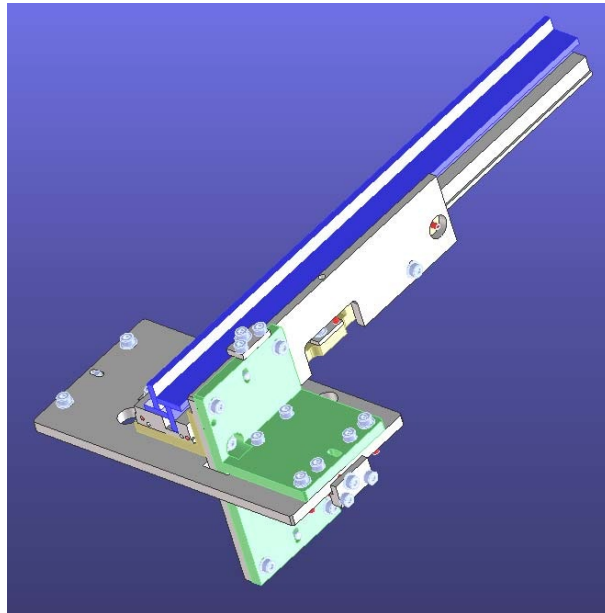


Figure 4.2.: Hollow mirror-integrator tunnel with a quadratic cross section of  $2.5\text{ mm}$  side length and  $250\text{ mm}$  length.

During the planning phase we also considered a homogenization design based on a fly's eye condensor (two consecutive microlens arrays). According to simulations performed by In-Vision, this, however, would have been more difficult to adjust than the tunnel. In particular the system would have been more dependent on illumination wavelength compared to the tunnel.

In summary the following points are important in order to achieve homogeneous

## 4. Description of our prototype for spatio-angular illumination

illumination of focal and pupil plane with the tunnel:

- The image of the end of the bundle should properly cover the tunnel entrance. Especially the corners of the tunnel should not be darker than the center. Inhomogeneous illumination at the tunnel entrance leads to inhomogeneous illumination of the pupil plane SLM.
- The end of the fibre bundle must be adjusted in four axes (centering and angle).
- The focal length of the microlenses should be chosen shorter than predicted by pure etendue calculation in order to compensate coating defects on the edges of the cemented glass mirrors.

### 4.1.2. Fourier optical filter for contrast generation on pupil plane SLM

The micro mirror array consists of torsion mirrors that modulate the phase of the light (see Figure 4.3 for images of the device). It is used as a pupil plane SLM. In order to modulate the intensity we use the Fourier optical filter denoted as 'schlierenoptics' in Figure 4.1 B.

The device itself is documented in more detail in the following references: design of the actuators (Schmidt et al. 2010), grey value images and contrast measurement (Berndt et al. 2010) and per-pixel calibration of the deflection angle using a white light interferometer (Berndt et al. 2011; Berndt 2007).

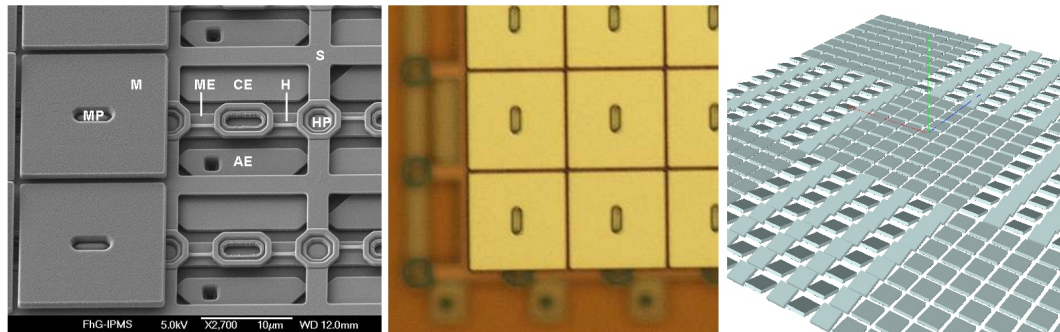


Figure 4.3.: **left:** Scanning electron microscope image of the micro-mirror array (MMA). The pixel pitch of the device is 0.016 mm. The hinges for the tilt movement and the electrodes are clearly visible. **middle:** Optical reflective microscope image of the MMA. **right:** Rendering of how a 8x8 checker board pattern would be displayed on the device. The deflection angles are exaggerated. Electron and optical micrograph by Fraunhofer IPMS Dresden, Germany

#### 4. Description of our prototype for spatio-angular illumination

The lens L1 has two purposes: First, it images the field mask B0 into the Fourier stop B1. Second, the plane P'' with the phase SLM is imaged to infinity.

With undeflected micro mirrors, the SLM has no significant effect and works like a plane mirror. Both planes F'' and P' are then homogeneously illuminated.

If the left half of the micro mirrors are tilted, then they direct the light along the dashed line in Figure 4.1. This light is absorbed by the field stop B1 and therefore missing in P', i.e. the right side in P' is dark. The total radiant flux (W) through the beam stop in F'' decreases while the transmitted irradiance ( $\text{W/m}^2$ ) remains homogeneous.

Since the torsion angles of the micro mirrors are quite small, the contrast generation in our Fourier filtering device (denoted as schlierenoptics in Figure 4.1) is somewhat complicated. In the following I will describe the effect of the MMA phase function on a plane monochromatic wave. In particular, I will investigate the amount of light in the zeroth diffraction order depending on the torsion angle. Furthermore, the structure of the diffraction image limits the maximum acceptance angle of the system. I will show, that the acceptance angle is just barely sufficient for our experiments.

To describe the Fourier pattern, I first consider a single pixel with index  $p$  and width  $w = 16 \mu\text{m}$ . In one dimension its shape can be described by the following equation:

$$T_p(x) = \delta(x - x_p) \otimes (\text{rect}(x/w) \cdot e^{ik_{px}x}) \quad \text{with } \text{rect}(x) := \begin{cases} 1 & |x| < 1/2 \\ 0 & \text{else} \end{cases} \quad (4.1)$$

The convolution with the  $\delta$ -distribution shifts the pixel to the position  $x_p$  and  $k_{px}$  describes the torsion angle of the  $p$ -th mirror. With the Fourier transform

$$\frac{1}{w} \int_{-w/2}^{w/2} e^{ik_x} dx = \frac{\sin(kw/2)}{kw/2} =: \text{sinc}(kw/2) \quad (4.2)$$

one can express the Fraunhofer diffraction image of a single pixel:

$$\tilde{T}_p(k_x) = e^{ik_x x_p} (w \text{sinc}(kw/2) \otimes \delta(k_x - k_{px})) = e^{ik_x x_p} w \text{sinc}((k + k_{px}) \cdot w/2) \quad (4.3)$$

That is, the sinc-shaped diffraction image of the pixel shifts in k-space depending on the deflection of the mirror. Now I will derive the relationship between the direction of the reflected phase front, described by  $k_{px}$ , and the deflection  $l$  of the mirrors from the equilibrium position. For that I consider the term  $e^{ik_{px}x}$  in

#### 4. Description of our prototype for spatio-angular illumination

equation (4.1) at the point  $x = -w/2$ . The distance  $l$  is traversed twice during the reflection (see Figure 4.4 left). This can be expressed in the following equation.

$$e^{-ik_{px}\frac{w}{2}} = e^{\frac{2\pi i}{\lambda}2l} \quad (4.4)$$

Solving for  $k_{px}$  results in:

$$k_{px} = -\frac{2\pi}{\lambda} \frac{4l}{w} \quad (4.5)$$

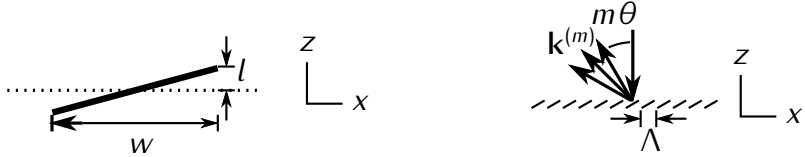


Figure 4.4.: **left:** Schematic indicating the deflection  $l$  of a micro mirror. **right:** Illustration of diffraction orders of the micro mirror array.

1D diffraction problem

Now I investigate a line of  $N$  pixels in the plane  $P''$  in Figure 4.1. The  $N$  pixels are distributed with a pitch of  $\Lambda$ , i.e. the  $p$ -th pixel is centered at  $x_p = \Lambda \cdot p$  with the index  $p = -[N/2], \dots, [N/2] + 1$  where  $[N/2]$  denotes the biggest integer below  $N/2$ . For simplicity I neglect gaps between the mirrors and the surface deformations at the central attachment point (see Figure 4.3). Therefore, in the following derivations I consider the pixel pitch to be identical with the pixel width:  $\Lambda = w = 16 \mu\text{m}$ . The Fourier spectrum  $\tilde{T}_{\text{line}}$  of a line of  $N$  pixels is (positioned in the plane  $F''$  in Figure 4.1):

$$\tilde{T}_{\text{line}}(k_x) = \sum_{p=-[N/2]}^{[N/2]+1} T_p(k_x) = w \sum_{p=-[N/2]}^{[N/2]+1} e^{ik_x \Lambda p} \text{sinc} \left( \frac{w}{2}(k_x + k_{px}) \right) \quad (4.6)$$

The sum over the first exponential term in this expression corresponds to a grating of  $N$  lines with a period equal to the pixel pitch. Depending on the torsion angle of individual mirrors the terms are modulated with a correspondingly shifted sinc-function. In the first diagram in Figure 4.5 left the intensity  $|\sum_p \exp(ik_x \Lambda p)|^2$  of the sum over the phase factor is displayed for  $N = 1$ ,  $N = 4$  and  $N = 20$ . With an increasing number of mirrors  $N$  the diffraction peaks become more pronounced. The micro mirror device that was built for our prototype has  $N = 256$ , that is to say the sum over the phase factors corresponds to a train of fine diffraction orders

#### 4. Description of our prototype for spatio-angular illumination

at wave vectors  $k_x^{(m)}$  described by the grating equation (see Figure 4.4 right):

$$\sin \theta = \frac{m\lambda}{\Lambda}, \quad k_x^{(m)} = \frac{2\pi}{\lambda} \sin \theta = m \frac{2\pi}{\Lambda} \quad (4.7)$$

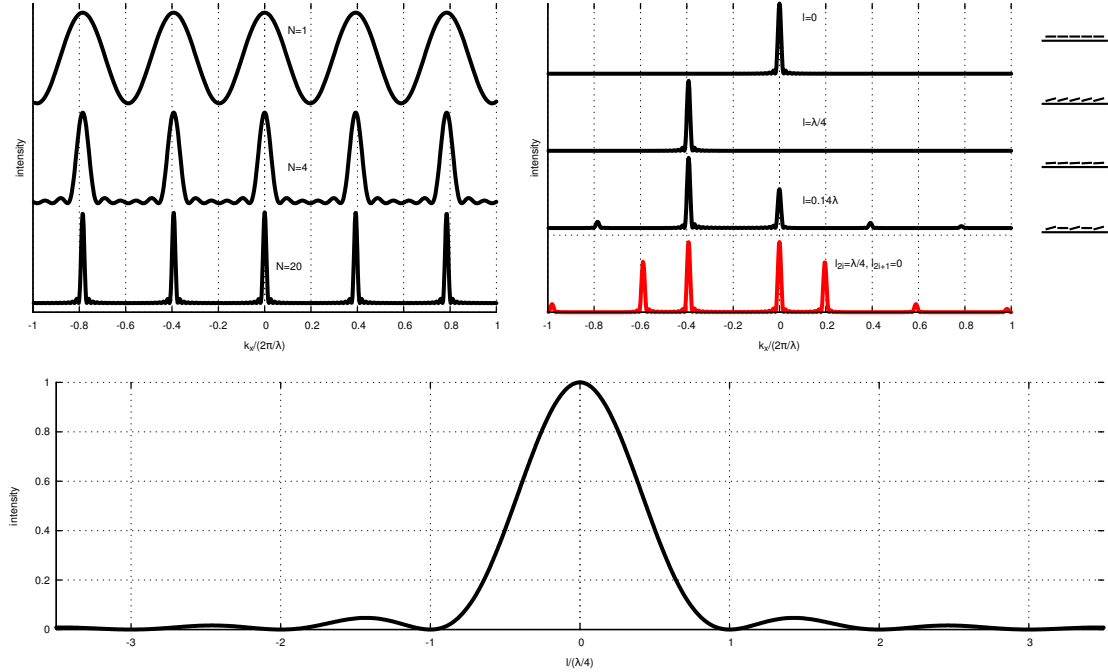


Figure 4.5.: **left:** Intensity of the diffraction pattern of a line grating  $|\sum_{p=-[N/2]}^{[N/2]+1} e^{ik_x \lambda p}|^2$  for an increasing number of lines  $N$ . **right:** Intensity of the diffraction pattern  $|\tilde{T}_{\text{line}}(k_x)|^2$  according to equation (4.6) for four different mirror deflections. The diagrams on the right indicate the mirror shapes. For the red curve every second pixel remains in the equilibrium position. **bottom:** Intensity in the zeroth diffraction order  $|\tilde{T}_{\text{line}}(k_x = 0)|^2$  for various deflections  $l$  (all mirrors deflected to the same angle).

Figure 4.5 right displays numerical evaluations of the full expression  $|\tilde{T}_{\text{line}}(k_x)|^2$  for  $N = 20$  and varying mirror deflections  $l$ . In the case of  $l = 0$ , all mirrors are undeflected and all the light remains in the zeroth order. A particularly interesting case occurs for  $l = \lambda/4$  (blaze condition) where all the light is reflected into the first order.

The bottom diagram in Figure 4.5 shows the intensity in the zero order for

#### 4. Description of our prototype for spatio-angular illumination

varying mirror deflections:

$$|\tilde{T}_{\text{line}}(k_x = 0)|^2 = \text{sinc}(4\pi l/\lambda)^2 \quad (4.8)$$

According to the diagram for a deflection of the mirrors between 0 and  $\lambda/4$  intensity in the zero order is gradually modulated. In our system this means that the intensity at any point in the plane  $P'$  (see Figure 4.1) depends on the deflection of the mirror that is conjugate to this image point. Up to now, all the calculations were done for a single plane wave corresponding to light emanating from a single point in  $F''$  (see Figure 4.1).

However, for the application in the spatio-angular microscope it is necessary to consider an extended light source with a diameter controlled by the aperture  $B_0$  in  $F''$ . Illuminating with an extended incoherent source corresponds to a convolution of the diffraction pattern in  $F''$  with an image of the source (a circle with the diameter of the aperture  $B_0$ ). In order to achieve intensity modulation with high contrast in the plane  $P'$ , the Fourier filter aperture  $B_1$  in  $F''$  may only transmit zero order light of the diffraction spectrum and must exclude any higher orders. We choose the radius  $d_{\max}$  of the apertures  $B_0$  and  $B_1$  to be smaller than half the distance between two consecutive diffraction orders. Therefore, the acceptance angle of the micro mirror array in the schlierenoptical system is  $|k_x^{(0)} - k_x^{(1)}|/2$ .

For historical reasons mirrors in adjacent rows of the micro mirror array tilt in opposite directions. Apparently, for other applications a symmetric Fourier spectrum is advantageous. However, in our application this design decision leads to an additional reduction of the acceptance angle by a factor of two.

In order to substantiate this statement I will now derive the two-dimensional surface profile of the micro mirror array. Individual mirrors are square and adjacent rows of them can only be deflected in the opposite direction. A measured profile is depicted in Figure 4.6 left. I index the pixel rows of the device with  $q$  and the columns with  $p$ .

$$T_{\text{array}}(x, y) = \left( \text{rect}(y'/w) \otimes_{y'} \sum_{q=-[N/2]}^{[N/2]+1} \delta(y' - q\Lambda) T_{\text{line}}^{(q)}(x) \right) (x, y) \quad (4.9)$$

$$= \sum_q \sum_p e^{ik_{(pq)x}x} \text{rect}\left(\frac{y + \Lambda q}{w}\right) \text{rect}\left(\frac{x + \Lambda p}{w}\right) \quad (4.10)$$

The convolution with respect to  $y'$  in equation (4.9) replicates  $N$  mirror rows with

extended source and  
partial coherence

2D diffraction  
pattern

#### 4. Description of our prototype for spatio-angular illumination

width  $w$  and pitch  $\Lambda$ . The value of  $k_{(pq)x}$  controls each individual mirror tilt. The constraints on these tilts are:

$$k_{(pq)x} \in \begin{cases} [0, k_x^{\max}] & q \text{ even} \\ [-k_x^{\max}, 0] & q \text{ odd} \end{cases} \quad \text{with } k_x^{\max} = \frac{2\pi}{\lambda} \frac{4l^{\max}}{w} \quad (4.11)$$

and the maximum deflection  $l^{\max} = 250 \text{ nm}$ . The tilt pattern to deflect all mirrors into the blaze condition and to darken the entire image in  $P'$  is  $k_{(pq)x}^{\text{dark}} = (-1)^q \cdot k_x^{\max}$ .

Figure 4.6 right shows the diffraction pattern of the two-dimensional micro mirror array for tilt angles that are close to, but not exactly fulfilling the blaze-condition. Therefore, most light is deflected into higher orders. The circles with radius  $d_{\max}$  in this image indicate the maximum size of the apertures B0 and B1 at which the device can achieve high contrast. Note that this is only true for moderately smooth variations of the pixel tilts  $k_{(pq)x}$ . Displaying a checkerboard pattern with two pixel period, i.e.  $k_{(pq)x} = k_{(pq)x}^{\text{dark}} \cdot ((-1)^{p+q} + 1)/2$ , would require a smaller radius than  $d_{\max}$  for the illumination aperture B0 because of additional "orders" that appear in the diffraction pattern (similar to the additional order at  $k_x = 0.2 \cdot 2\pi/\lambda$  of the red curve in Figure 4.5 right). In all my experiments I usually put more emphasize on a large acceptance angle than on contrast or pattern resolution in the back focal plane. I always used moderately varying pupil plane patterns.

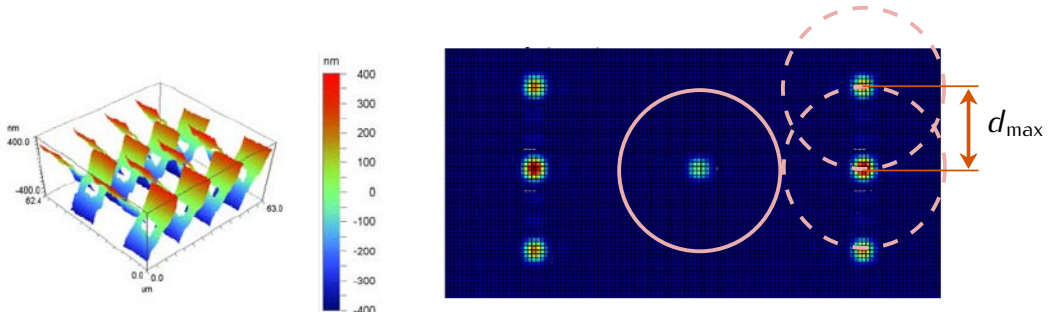


Figure 4.6.: **left:** Measurement of the deflection of micro-mirrors using a white-light interferometer (provided by Fraunhofer IPMS Dresden, Germany). **right:** Simulation of the Fraunhofer diffraction pattern of the micro-mirror array for coherent, monochromatic light (kindly provided by Joel Seligson). The circles with radius  $d_{\max}$  indicate the maximum size of the field mask B0 where the diffraction orders do not overlap. This limits the etendue of our illumination system.

The smallest distance between the orders in Figure 4.6 right corresponds to diffraction at a grating with a period of two mirror pitches. Therefore, the

## 4. Description of our prototype for spatio-angular illumination

diffraction angle  $\theta$  is:

$$\sin \theta = \lambda / (2\Lambda) \quad (4.12)$$

and the maximum radius can be expressed as:

$$d_{\max} = f_{L1} \tan \theta \approx \frac{f\lambda}{2\Lambda} \quad (4.13)$$

Here,  $f_{L1}$  is the focal length of lens L1. With the F-number  $\# = f_{L1}/(2d_{\max})$  one can calculate the maximum etendue of the schlierenoptical system:

$$\mathcal{E} = \frac{\pi A}{4\#^2} = \frac{\pi A \lambda^2}{4\Lambda^2}, \quad (4.14)$$

with the area  $A = (4 \text{ mm})^2$  of the micro-mirror array.

For our system the maximal etendue is between  $0.0079 \text{ mm}^2/\text{sr}$  (for  $400 \text{ nm}$  wavelength) and  $0.024 \text{ mm}^2/\text{sr}$  (for  $700 \text{ nm}$  wavelength). This is much smaller than the etendue of a typical microscope objective ( $0.27 \text{ mm}^2/\text{sr}$ , see section 1.3.3). With the following equation the more intuitive diameter of the illuminated field in the sample can be determined:

$$D_{\text{field}} = \frac{2}{\text{NA}} \sqrt{\frac{\mathcal{E}}{\pi}} \quad (4.15)$$

For a wavelength of  $\lambda = 400 \text{ nm}$  the maximum diameter is  $D_{\text{field}}^{\text{blue}} = 70 \mu\text{m}$  and for  $700 \text{ nm}$  wavelength it is  $D_{\text{field}}^{\text{red}} = 125 \mu\text{m}$ , opposed to  $400 \mu\text{m}$ , that the microscope objective would permit.

### 4.1.3. Relay optics between pupil plane and focal plane SLM

The lenses L2 and L3 form a double-telecentric relay system with magnification 2 and image  $F''$  onto the focal plane SLM in  $F'$ . At the same time these lenses make sure that the pupil plane SLM is imaged to infinity.

The relay system ensures that the focal plane SLM pixels with a pitch of  $13.62 \mu\text{m}$  (see Figure 4.1) are at the resolution limit, while the pupil plane SLM fills the pupil. In addition, the relay system enables a simpler mechanical realization and good contrast. It would be difficult to accommodate the focal plane SLM and polarization beam splitter in  $F''$ . Attaching an adjustable schlieren aperture would probably not be feasible at all.

## 4. Description of our prototype for spatio-angular illumination

### 4.1.4. Contrast generation on focal plane SLM using polarization

The SLM we use to control the focal plane illumination is a ferroelectric liquid crystal on silicon device (fLCoS, ForthDD WXGA R3, UK). If a pixel is in the off-state the returning light retains its polarization. If a pixel is in the on-state, the polarization of the light is rotated by 60 degrees (Martínez-García et al. 2009). From this, a polarization beam splitter generates a binary intensity contrast (see Figure 4.1 C).

We have not used a digital micro-mirror device (DMD), because those mirrors have sharp edges and loose significant amounts of light into higher orders that can not contribute to the image in the specimen. The pixels borders of a fLCoS device are defined by electric fields and are therefore more blurred. In this sense, an fLCoS based device should be more efficient than a DMD.

We use a wire-grid polarization beam splitter (Moxtek PBF02C, Orem, UT, US) because they ensure a high enough optical quality, good contrast and the plate causes less back reflection than a beam splitter cube.

The s-polarized component of the incoming light is reflected towards the SLM. Active pixels of the SLM rotate the polarization of light by 60 degrees. The light then passes through the beam splitter as p-polarization in the direction of the microscope. There is a supplementary cleanup analyzer in the beam path.

It would also be conceivable to arrange SLM and the polarization beam splitter (PBS) differently, so that the light coming from the SLM is *reflected* towards the microscope. In this case, however, unwanted bending of the beam splitter's surface would deteriorate the image quality of the focal plane SLM. Therefore, we use the beam splitter in transmission.

### 4.1.5. Variable telescope as tube lens

Microscope objectives come with various pupil diameters. The last lens  $T_{\text{Lill}}$  in our illumination system has been designed as a variable zoom objective (by In-Vision, Guntramsdorf, Austria), that maps the pupil plane SLM from  $P''$  to  $P$  with variable magnification.

Unlike conventional zoom telescopes we use three movable lens groups to guarantee that the image of the pupil plane SLM remains stationary while the focal plane SLM is imaged into infinity during magnification changes.

Why fLCoS and not DMD?

polarizing beam splitter

#### 4. Description of our prototype for spatio-angular illumination

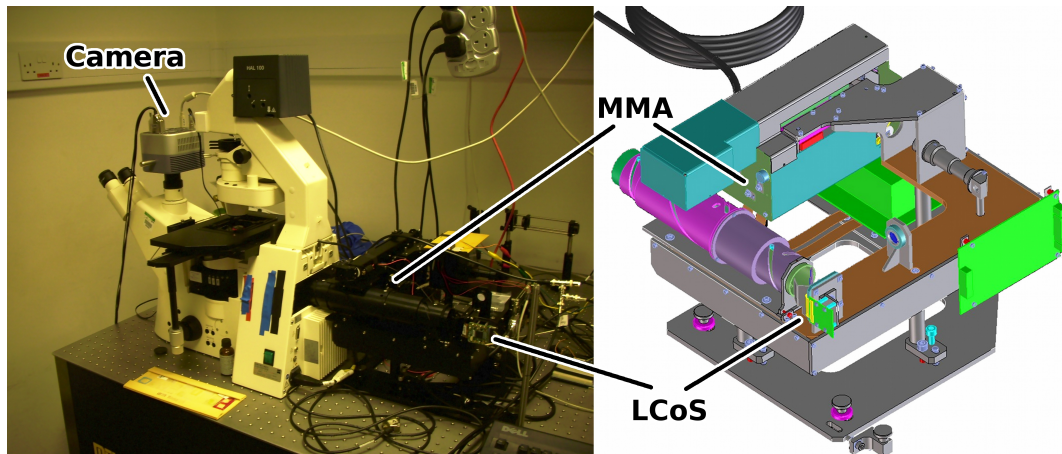


Figure 4.7.: The widefield epi-fluorescence microscope with attached illumination head. The positions of the two spatial light modulators (pupil plane SLM: micro mirror array (MMA) and focal plane SLM: liquid crystal on silicon display (LCoS)) are indicated. Drawing by Josef Wenisch (In-Vision, Austria).

#### 4.2. Electronic control of the component

local pattern storage

Both spatial light modulators can run at most with 50% duty cycle. Therefore it is necessary to synchronize the displays. The controllers of the displays allow to upload several hundred frames of image data into local storage at the beginning of an experiment. Images can then be selected by relatively fast function calls over USB (focal plane SLM, fLCoS) or Ethernet (pupil plane SLM, MMA), see Figure 4.8 for a plan of the interconnections.

camera is master

The camera (Clara, Andor PLC, Belfast, Northern Ireland) is the slowest device and therefore is chosen as the master. It provides two TTL outputs. The output "fire" is high while the camera is integrating. The output "shutter" is programmed to reach high 1 ms before "fire".

This time period allows sufficient margin for an Arduino microcontroller to initiate a time-delayed trigger for both SLMs, so that they show their patterns exactly while the camera is integrating. I determined the necessary delays using a photodiode and an oscilloscope in order to measure when a dark image is established on each device. The delay is  $840\ \mu s$  for pupil plane and  $396\ \mu s$  for focal plane SLM. The Arduino microcontroller activates a laser by an acousto-optic modulator (AOM) so that the system is only illuminated when the camera is integrating and both SLM are showing a defined pattern.

disadvantage of LCoS controller

The USB LCoS controller for the focal plane SLM can display the images only for certain discrete times (20 ms, 10 ms, 5 ms, 200  $\mu s$ ). This is because it needs to

#### 4. Description of our prototype for spatio-angular illumination

be programmed with sequences which are supplied by the manufacturer and it is not straightforward to change them via USB interface. Therefore we always work with a fixed LCoS display time of 20 ms.

synchronization with stage

The camera acquisitions are stopped by the control software, whenever the XYZ-stage is moved. Hardware triggering could accelerate the acquisition of z-stacks, but has not been implemented so far.

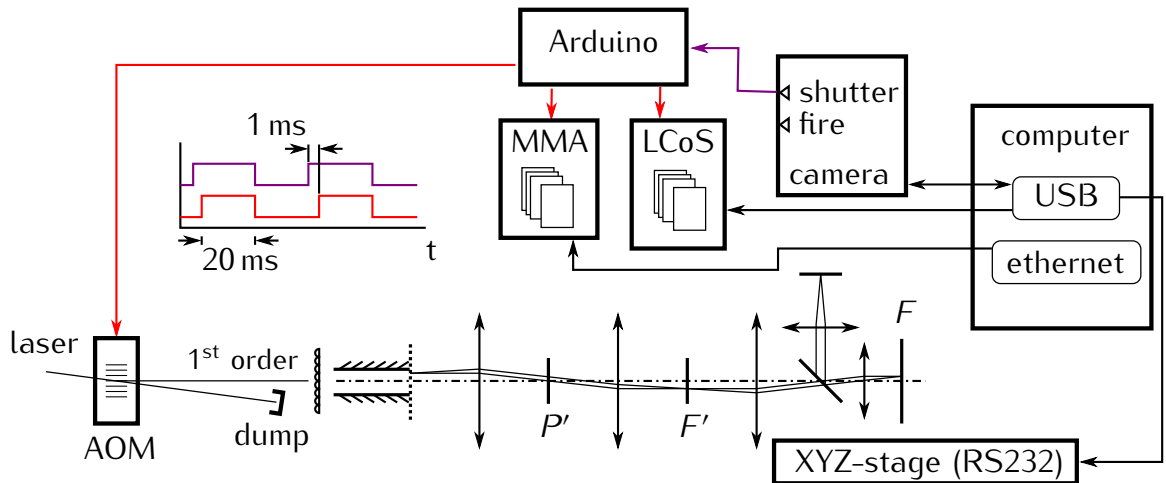


Figure 4.8.: The camera triggers the Arduino microcontroller 1 ms before its integration begins. The microcontroller then starts the two SLM so that they have enough time for initialization and later enables the laser at the predefined interval, where the camera is exposing.

#### 4.3. Mapping between pixels of the focal plane SLM and camera pixels

A basic prerequisite for measurement with our system is that the mapping between SLM and camera pixels is known. Only then, the sample can be irradiated as planned. To measure the mapping, I use a fluorescent plane sample placed at the focal plane of the objective, turn on individual pixels at position  $r^d$  of the focal plane SLM and acquire camera images, which have bright spots centered on a camera coordinate  $r^c$ .

The fluorescent plane is attached directly to the underside of the cover slip, ensuring good image quality and no (or negligibly small) distortion.

## 4. Description of our prototype for spatio-angular illumination

### 4.3.1. The rigid transform

In our experiments, the following transformation with four degrees of freedom (scaling  $s$ , rotation angle  $\phi$ , translation vector  $\mathbf{t} = (t_x, t_y)^T$ ) has proved particularly advantageous:

$$\mathbf{r}^d = s\mathbf{R}_\phi \mathbf{r}^c + \mathbf{t} \quad (4.16)$$

$$\mathbf{R}_\phi = \begin{pmatrix} \cos \phi & q \sin \phi \\ -\sin \phi & q \cos \phi \end{pmatrix} \quad (4.17)$$

where  $\mathbf{r}^d = (r_x^d, r_y^d)^T$  is a point on the display,  $\mathbf{r}^c = (r_x^c, r_y^c)^T$  is a point on the camera and  $R_\phi$  is a rotation matrix. The value of  $q$  depends on the arrangement of mirrors in the beam path. The parameter  $q$  is  $-1$ , if there is a single axis reflection and it is  $+1$  if there is no reflection.

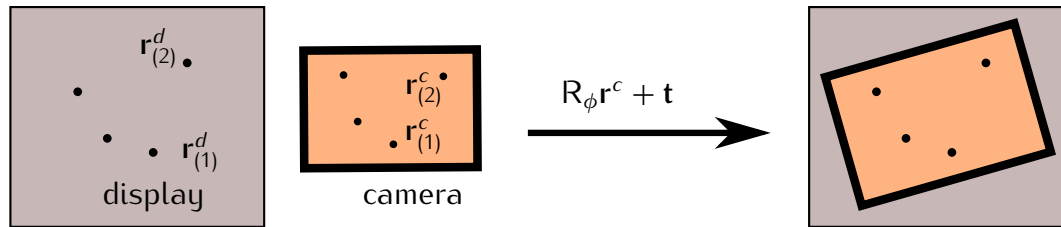


Figure 4.9.: Given  $n \geq 4$  camera images of a display showing one point. It is possible to calculate the parameters of the rigid transform parameters scaling  $s$ , rotation angle  $\phi$ , translation vector  $\mathbf{t}$ .

Alternatively, in the beginning we experimented with an affine transformation. This transform is over-determined, as it includes two additional degrees of freedom for shear and anisotropic scaling, which are negligible in our system. Therefore it is difficult to assess the quality of the calculated affine transform parameters.

With the rigid transform in equation (4.16), our system can, however, be modeled very well: The camera is connected to a flange on the microscope body and can be easily rotated. So when the camera is moved, ideally, only the rotation angle  $\phi$  needs to be recalibrated. Similarly, the focal length setting of the illumination tubelens  $TL_{ill}$  mainly affects the scale  $s$ .

## 4. Description of our prototype for spatio-angular illumination

### Computational parameter estimation

Having measured a set of  $n \geq 4$  tuples  $(\mathbf{r}_i^c, \mathbf{r}_i^d)$  of camera and SLM coordinates, the four rigid transform parameters can be obtained by minimizing the error  $\mathcal{Q}$ :

$$\mathcal{Q} = \sum_i^n |sR_\phi \mathbf{r}_i^c + \mathbf{t} - \mathbf{r}_i^d|^2 \quad (4.18)$$

There are good algorithms to solve this type of least squares problem. In appendix C.1 I show the source code for the computer algebra system Maxima (Maxima.sourceforge.net 2012). With “Maxima” the implementation is particularly concise because it transparently calculates all the necessary derivatives symbolically.

### 4.3.2. Experimental example and image processing

Now I will show example images to describe the data collection for measuring the transformation between camera pixels and focal plane SLM.

sample preparation

For good results it is useful to have a fluorescent plane sample that is homogeneous and without empty (non-fluorescent) holes. I succeeded in making particularly thin and uniform fluorescent planes with fluorescent beads. I prepared the sample by drying an undiluted suspension of sub-diffraction, fluorescent latex beads on a cover slip. This results in expanded areas with uniform mono-, double- or multi-layers (see Figure 4.10).

maximize field

It is also advantageous if as large an area of the focal plane SLM as possible is taken into account for the estimation of the transform’s parameters. Therefore I opened the two diaphragms B0 and B1 (see Figure 4.1) completely for the calibration measurements. I also kept the mirrors of the pupil plane SLM undeflected to ensure maximum irradiance in the sample.

scanning SLM pixel grid

For the calibration I usually do not only enable individual SLM pixels as this would give very dim images with 20 ms integration time. Instead, I enable pixels in a circular area around the centre. This results in images as depicted in Figure 4.10 right. I acquired 100 such camera images while moving the circular mask on the focal plane SLM over a  $10 \times 10$  grid (a disk of 24 focal plane SLM pixels diameter at the positions  $\mathbf{r}_{i+j}^d = (400 + 50i, 500 + 50j) \forall i, j \in [0, 99]$ ). Accidentally a number of these points fell outside of the illuminated area and were excluded from further processing.

In Appendix C.2 I show Matlab code (using the DIPimage toolbox, Diplib.org

#### 4. Description of our prototype for spatio-angular illumination

(2012)) to determine the position of the bright spot in each camera image. Since the size of the illuminated areas in the sample is bigger than the diffraction limit and inhomogeneities of the fluorescent layer therefore will be visible in the image, the image data must be corrected by dividing the pixel values by the data of a uniformly illuminated image of the identical region after background subtraction. Otherwise, sample non-uniformities would bias the results of the localization algorithm.

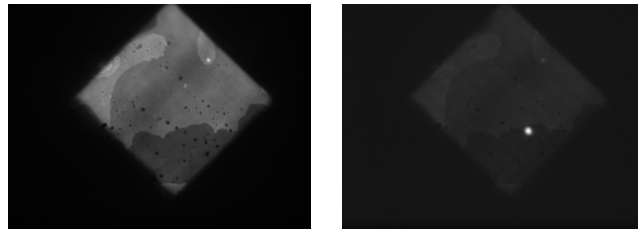


Figure 4.10.: **left:** Uniformly illuminated fluorescent plane (mono and double layer of yellow beads with 110 nm diameter, excited with 473 nm laser in a 63 $\times$  objective with NA = 1.47). **right:** Image with the the focal plane SLM displaying a disk with 24 pixels diameter (corresponding to 2.4  $\mu$ m in the sample) centred at focal plane SLM position  $r^d = (550, 750)$ .

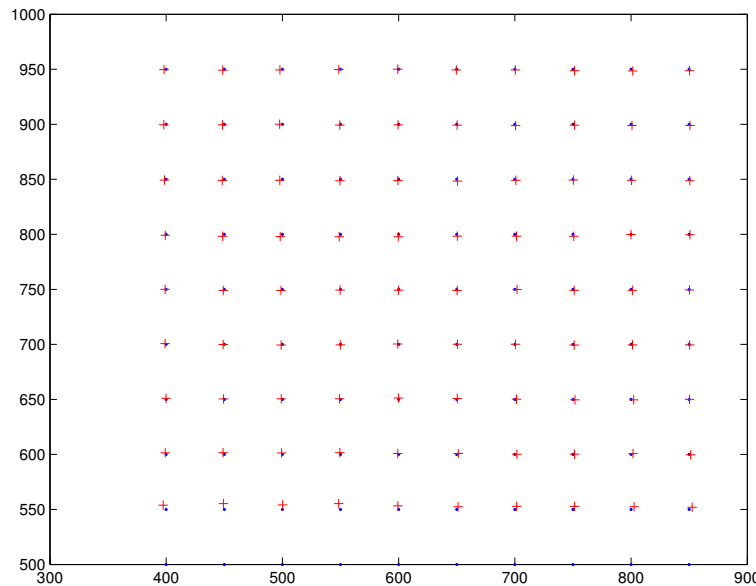


Figure 4.11.: Red "+" signs indicate where the spots that were localized in the camera images end up after a rigid transform. There is sufficient agreement with the original display positions.

Figure 4.11 shows how well the transformed camera coordinates ( $r^c$ , indicated by '+' signs) superimpose with the coordinates of the focal plane SLM pixel grid.

#### 4. Description of our prototype for spatio-angular illumination

Figure 4.12 left depicts a pattern of discs that was displayed on the focal plane SLM and the right figure shows a superposition of the camera image and the outline of the circles.

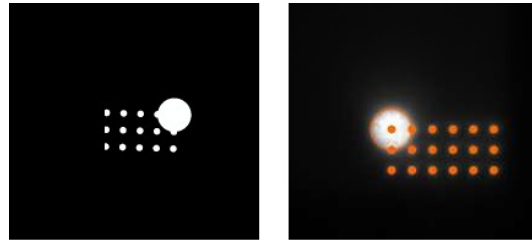


Figure 4.12.: Example of a rigid transform between focal plane SLM and camera. **left:** Mask that is displayed on the SLM. **right:** Camera image of fluorescent plane illuminated by mask. The orange outlines indicate the borders of the original pattern. The transformation between the coordinates fits very well and the illumination mask exactly covers the image, i.e. it is possible to selectively illuminate even small structures using the focal plane SLM.

##### 4.3.3. Conclusion on the mapping transformation

I have shown the simplest possible transformation to map between the pixel grid of the camera and the focal plane SLM.

For this I have implemented a calibration routine using a computer algebra system which would allow for more complicated transformations, e.g. considering image distortion. However, my experiments have shown that the simple transform is sufficient for our requirements and the field of view, that the current illumination system supports.

The results of a calibration with this particular transformation can be easily inverted. Furthermore, the interpretation of the parameters and their fitting errors is obvious and simple. In particular, the fitted transform parameters scaling  $s$ , rotation  $\phi$  and translation  $t$  can be used directly in OpenGL to transform vector primitives in an elegant way and with negligible computational effort. I give example code in Appendix C.1.1.

#### 4.4. Optical sectioning by structured illumination

As mentioned in section 1.3.2 on page 27, a uniform signal of background fluorescence is inevitable in widefield microscopy. Here, I explain how in-focus and out-of-focus information can be separated by structured illumination.

#### 4. Description of our prototype for spatio-angular illumination

In order to provide maximum imaging speeds with our system, I investigated techniques to obtain optically sectioned images with as few exposures per slice as possible. Illuminating with a sinusoidal grating has proved to be particularly advantageous because then the necessary image processing can be expressed elegantly with linear operations in Fourier space. Using the HiLo method (Mertz and Kim 2010), already two acquisitions allow to calculate an optical section.

When a sinusoidal grating is imaged into the focal plane of a microscope objective using incoherent light then the three-dimensional light distribution in the sample has the  $xz$ -cross section shown in Figure 4.13 left. I generated this image by a convolution of a sinusoidal transmission grating with the three-dimensional point spread function of a  $63\times$  oil ( $n = 1.52$ ) immersion lens and  $NA = 1.4$ . The Matlab/DIPimage source code that I used to generate the images in this section is listed in appendix B on page 123.

For optical sectioning the essential effect that allows separation of in-focus and out-of-focus light is that according to Figure 4.13 an in-focus fluorophore at point (a) experiences a change in excitation intensity when the grating phase is shifted. An out-of-focus fluorophore at point (b), however, is always exposed to equal amounts of excitation light. There are many possibilities to determine the degree of modulation in the acquired images. Three of them I will introduce now.

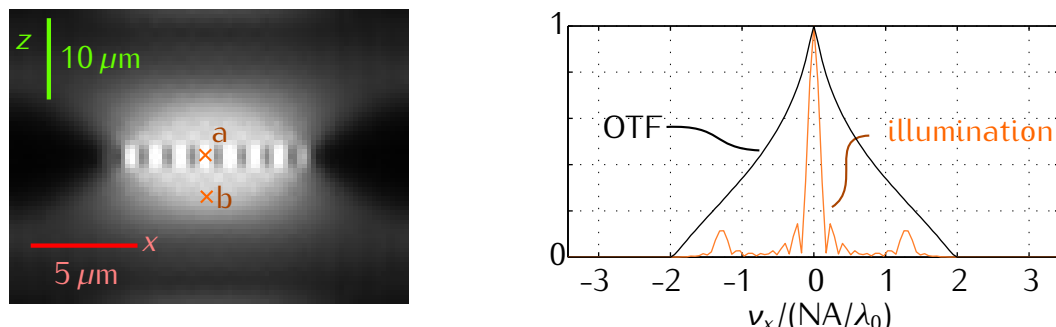


Figure 4.13.: **left:** Light distribution in the sample for a  $63\times$  objective with  $NA = 1.4$  and immersion index  $n = 1.52$  using a grating pattern and incoherent illumination of wavelength  $\lambda_0 = 500\text{ nm}$ . **right:** Cross-section of the in-focus optical transfer function (OTF) of this objective and spatial frequency spectrum of the in-focus light distribution.

For the simplest algorithm (Benedetti et al. 1997) one assumes that the in-focus information is responsible for the majority of the signal. One can recover an approximation of the in-focus information by calculating the maximum of a pixel value in the images  $I_n$ . Where  $n = 1, \dots, N$  denotes the phase of the pattern in each image. The out-of-focus background remains the same in each pixel of the

#### 4. Description of our prototype for spatio-angular illumination

raw images and can be approximated by the minimum of each pixel value:

$$I_{\text{max-min}}(x, y) = \max_{n=1 \dots N} (I_n(x, y)) - \min_{n=1 \dots N} (I_n(x, y)) \quad (4.19)$$

However, this method has the disadvantage that the noise of the reconstructed image does not decrease with an increasing number of acquisitions  $N$ . Another method, which is related to homodyne detection (Neil et al. 1997), allows the separation of the modulated signal if at least three raw images are available:

$$I_{\text{homodyne}}(x, y) = \left| \sum_{n=1 \dots N} I_n(x, y) e^{2\pi i n/N} \right|, \text{ and } N \geq 3 \quad (4.20)$$

In particular, with this approach each acquisition contributes to the reconstructed optical section, resulting in a better noise performance than the 'max-min' method. In Figure 4.14 c) and d) I compared these reconstruction methods for  $N = 4$  using a simulated fluorophore distribution as depicted in Figure 4.14 a). In the simulated widefield image Figure 4.14 b) the intensity in the points 1 and 2 is similar, while the results of the sectioning algorithms in c), d) and e) reject significant amounts of out-of-focus light in point 2.

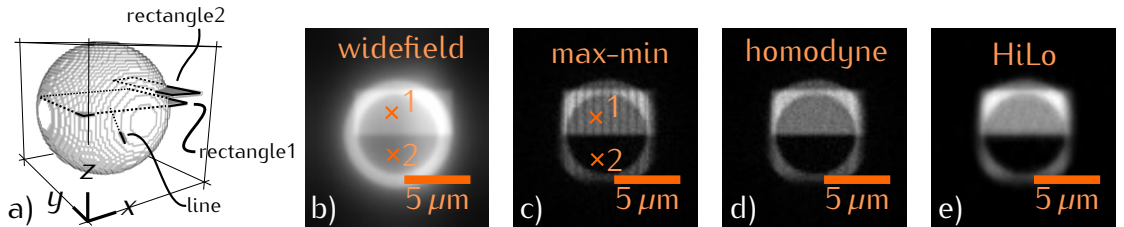


Figure 4.14.: a) Distribution of fluorophores for the simulations in this section. Two rectangles and a line intersecting a hollow sphere shell. b) Widefield image in the slice with rectangle 1. c,d,e) Optical sections of this slice using three different methods. The brightest points of the raw images were set to contain 60000 photons and their photon shot noise was included in these simulations.

The reconstruction methods can all separate the rectangle from background fluorescence. The simple 'max-min' method, however, causes artifacts in the reconstruction. The spurious stripes would only disappear if significantly more images were recorded. The homodyne method gives a very good result but requires at least three images (I used four to obtain Figure 4.14 d).

In contrast, the HiLo method requires only two acquisitions (and I used only two for Figure 4.14 e). I will now describe my version of the algorithm. The HiLo

#### 4. Description of our prototype for spatio-angular illumination

method was originally developed for speckle illumination (Ventalon and Mertz 2005; Ventalon et al. 2007; Lim et al. 2011) but has also been used for structured illumination with grating patterns (Bozinovic et al. 2008; Mertz and Kim 2010).

Assuming the grating varies in the  $x$ -direction then the information in the two raw images can be expressed as a superposition of modulated in-focus information  $I_{\text{in}}$  and out-of-focus information  $I_{\text{out}}$  that is the same in all raw images (Mertz and Kim 2010):

$$I_n(x) = (1 + m \sin(k_g x + n\pi)) I_{\text{in}}(x) + I_{\text{out}}(x), \text{ with } n = 0, 1 \quad (4.21)$$

Here,  $m$  is the modulation contrast and  $k_g$  the spatial frequency of the excitation pattern. For HiLo, the two raw images are combined to form two new images:

$$I_{\text{wf}}(x) = I_0(x) + I_1(x) = 2(I_{\text{in}} + I_{\text{out}}(x)) \quad (4.22)$$

$$I_{\text{demod}}(x) = I_0(x) - I_1(x) = 2m \sin(k_g x) I_{\text{in}} \quad (4.23)$$

The sum of the raw images corresponds to a widefield image with uniform illumination, containing sectioned sample information only for higher spatial frequencies (see Figure 1.6 on page 26). The image  $I_{\text{demod}}$  allows extraction of in-focus information for low spatial frequencies of the fluorophore distribution. For HiLo, in-focus information from different parts of the spatial frequency spectra of the images  $I_{\text{wf}}$  and  $I_{\text{demod}}$  are combined to form the new image  $I_{\text{hilo}}(x)$ :

$$I_{\text{hilo}}(x) = \eta \text{ HP}(I_{\text{wf}}(x)) + \text{LP} \left( \text{FT}^{-1} \left[ \frac{\tilde{I}_{\text{demod}}(k - k_g)}{\text{OTF}(k)} \right] (x) \right) \quad (4.24)$$

With the low-pass filter LP, whose cutoff frequency is quite small, so that other orders of the spatial frequency spectrum of  $I_{\text{demod}}$  do not contribute to the signal (see Figure 4.15 e). HP is a the complementary high-pass filter and the factor  $\eta$  is introduced to compensate for the modulation contrast  $m$ . I divide by the optical transfer function (see Figure 4.13) in order to re-weight the sample information surrounding the first order in  $I_{\text{demod}}$ . This is necessary because sample information on different sides of the order were filtered differently by the optical transfer function. Both  $\eta$  and  $k_g$  must be determined for each experiment. The algorithm in Mertz and Kim (2010) does not require to specify  $k_g$  but their algorithm is non-linear and therefore gives biased results in the presence of photon shot noise.

#### 4. Description of our prototype for spatio-angular illumination

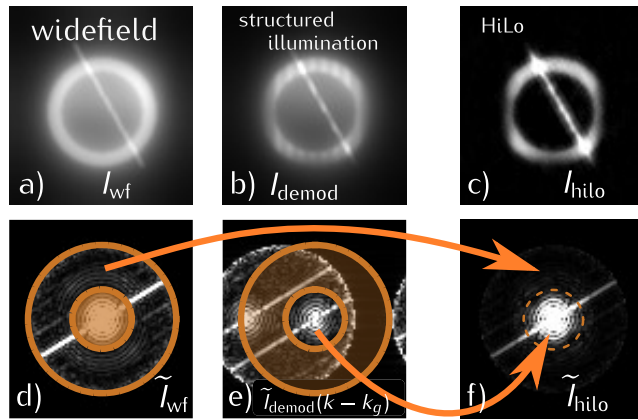


Figure 4.15.: Application of my HiLo algorithm variant to a slice in the simulated fluorophore distribution from Figure 4.14 a.

##### 4.4.1. Discussion and outlook on optical sectioning

In this section, I have given an overview of different methods for optical sectioning. In particular, I described a variant of the HiLo reconstruction algorithm which requires only two exposures per slice and is optimized for application in our instrument.

A thorough comparison of different algorithms in the presence of noise is still pending. Furthermore, it would be helpful to examine which projected grating frequencies will give the best sectioning results. In the examples, which were shown here, a grating pattern of high spatial frequency with the first order at  $\nu_x \approx 1.3\text{NA}/\lambda_0$  (see orange graph in Figure 4.13 right) was used. The best  $z$ -resolution would be expected for  $\nu_x = 1\text{NA}/\lambda_0$  since there, the support along  $z$  of the three-dimensional optical transfer function is widest (see Figure 1.6), with smaller spatial frequencies the modulation contrast  $m$  increases but so does the overlap with adjacent orders. The source code in appendix B should be a good starting point to investigate these questions.

## 5. Raytracing for spatio-angular microscopy

Imaging with the microscope we developed requires a continuous update of the patterns for the spatial light modulators during operation. It is not easily possible to solve the problem with commercial software. Therefore, a simple raytracer is implemented in this work.

This chapter documents the basic concepts. Some approximations, which are usually used in optical design (paraxial, only non-skew rays) are not applicable here, because rays are to be pursued in all possible angles through diverse fluorophore distributions in the specimen.

I begin by introducing simple geometric formulas to determine the points of intersection between a ray and a plane or a sphere. I also describe how to calculate refraction at a planar surface.

Then I explain the refraction at a thin, paraxial lens and show a modification of the formulas for high aperture lenses. This allows tracing rays through a microscope objective in two directions (denoted as detection or illumination direction) without knowing the exact design parameters and glass types.

Furthermore, I consider the refraction at the “cover slip–medium” interface for non-index matched media. This enables the calculation of illumination patterns for highly inclined and laminated optical sheet microscopy, as introduced in section 2.1.2.

I follow up with a rather technical discussion of a geometric problem that helps to significantly speed up the raytracing calculations for the specific case of a sample that can be represented as a three-dimensional distribution of fluorescent spheres.

**Note:** The formulas that are emphasized by surrounding frames are implemented in the computer code that is published on <https://github.com/plops/mma/tree/master/lens>.

## 5. Raytracing for spatio-angular microscopy

### 5.1. Basic geometric algorithms

#### 5.1.1. Intersection of a ray and a plane

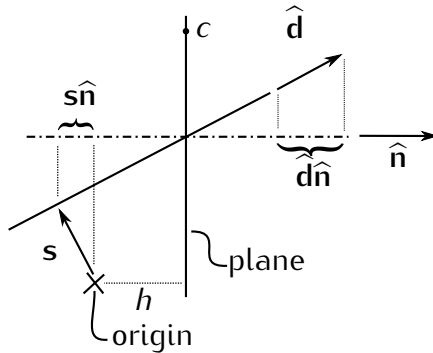


Figure 5.1.: Schematic of plane-ray intersection.

Let a ray start at a point  $s$  with direction  $\hat{d}$ . A plane (defined by a point  $c$  and the unit normal  $\hat{n}$ ) intersects this ray if its normal and the ray's direction are not perpendicular:  $\hat{n} \cdot \hat{d} \neq 0$ . The distance between the plane and the origin is  $h = c \cdot \hat{n}$ . The equation of the plane is given in Hesse normal form:

$$r \cdot \hat{n} = h \quad (5.1)$$

I replace the coordinate  $r$  with the ray equation and solve for the parameter  $\tau$ .

$$(s + \tau \hat{d}) \cdot \hat{n} = h \quad (5.2)$$

$$s \cdot \hat{n} + \tau \hat{d} \cdot \hat{n} = h \quad (5.3)$$

$$\tau = \frac{h - s \cdot \hat{n}}{\hat{d} \cdot \hat{n}} \quad (5.4)$$

The point of intersection is located on the ray at  $s + \tau \hat{d}$ .

#### 5.1.2. Intersection of a ray and a sphere

Let a ray start at a point  $s$  with direction  $\hat{d}$ . Let a sphere be centred in  $c$  with radius  $R$ . There are two equations

$$(r - c)^2 = R^2 \quad (5.5)$$

$$r = s + \tau \hat{d} \quad (5.6)$$

## 5. Raytracing for spatio-angular microscopy

that define the intersection points. By substituting  $\mathbf{r}$  one obtains a quadratic equation in the distance  $\tau$  along the ray:

$$(\mathbf{s} + \tau \hat{\mathbf{d}} - \mathbf{c})^2 = R^2 \quad (5.7)$$

$$\mathbf{l} := [\mathbf{s} - \mathbf{c}] \quad (5.8)$$

$$l^2 + 2\tau \mathbf{l} \cdot \hat{\mathbf{d}} + \tau^2 - R^2 = 0 \quad (5.9)$$

$$\underbrace{1}_a \tau^2 + \underbrace{2\mathbf{l} \cdot \hat{\mathbf{d}}}_b \tau + \underbrace{l^2 - R^2}_c = 0 \quad (5.10)$$

In order to prevent numerical errors the following solution should be used (Press et al. 1997):

$$\Delta := [b^2 - 4ac] \quad (5.11)$$

$$q := \left[ -\frac{b + \sqrt{\Delta} \operatorname{sign} b}{2} \right] \quad (5.12)$$

$$\tau = \begin{cases} q/a & \text{when } |q| \approx 0 \\ c/q & \text{when } |a| \approx 0 \\ (q/a, c/q) & \text{else} \end{cases} \quad (5.13)$$

If the discriminant  $\Delta$  is negative the ray misses the sphere and there is no solution. If the discriminant is zero the ray touches the periphery of the sphere and there is only one solution. A positive discriminant corresponds to two solutions.

### 5.1.3. Refraction at planar surface

Now I describe the refraction at a planar surface<sup>1</sup>. The wavelength of the light in vacuum defines the length of the wave vector  $\mathbf{k}_0$ . The lengths of the incident and transmitted wave vectors  $\mathbf{k}_1$  and  $\mathbf{k}_2$  are obtained by multiplication with the refractive index in their respective half space:

$$k_0 = 2\pi/\lambda \quad (5.14)$$

$$k_1 = n_1 k_0 \quad (5.15)$$

$$k_2 = n_2 k_0. \quad (5.16)$$

I choose the normal  $\hat{\mathbf{n}}$  to be directed into the half-space of the incident wave (see Figure 5.2) and define the transversal and normal component of the wave

---

<sup>1</sup>I use the same notation as McClain et al. (1993).

## 5. Raytracing for spatio-angular microscopy

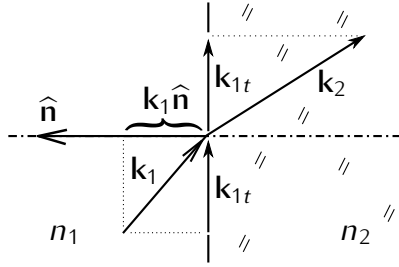


Figure 5.2.: Refraction at an interface transforms the incident wave vector  $\mathbf{k}_1$  into the outgoing wave vector  $\mathbf{k}_2$ .

vectors to be:

$$\mathbf{k}_{1n} = (\mathbf{k}_1 \hat{\mathbf{n}}) \hat{\mathbf{n}} \quad (5.17)$$

$$\mathbf{k}_{1t} = \mathbf{k}_1 - \mathbf{k}_{1n}. \quad (5.18)$$

These two vectors are orthogonal and during refraction the transversal component of the wave vector is invariant:

$$k_2^2 = k_{2n}^2 + k_{2t}^2 \quad (5.19)$$

$$\mathbf{k}_{2t} = \mathbf{k}_{1t}. \quad (5.20)$$

Using the two equations from above, one can calculate the length of the normal component of the transmitted wave vector  $\mathbf{k}_2$ :

$$k_2^2 = k_{2n}^2 + (\mathbf{k}_1 - \mathbf{k}_{1n})^2 \quad (5.21)$$

$$k_{2n}^2 = k_2^2 - (\mathbf{k}_1 - (\mathbf{k}_1 \hat{\mathbf{n}}) \hat{\mathbf{n}})^2 \quad (5.22)$$

$$= k_2^2 - (k_1^2 - 2(\mathbf{k}_1 \hat{\mathbf{n}})^2 + (\mathbf{k}_1 \hat{\mathbf{n}})^2) \quad (5.23)$$

$$= k_2^2 - k_1^2 + (\mathbf{k}_1 \hat{\mathbf{n}})^2. \quad (5.24)$$

Finally, one can express the full transmitted wave vector  $\mathbf{k}_2$  using only known quantities:

$$\mathbf{k}_2 = \mathbf{k}_{1t} - \sqrt{k_2^2 - k_1^2 + (\mathbf{k}_1 \hat{\mathbf{n}})^2} \hat{\mathbf{n}} \quad (5.25)$$

$$= \mathbf{k}_1 - (\mathbf{k}_1 \hat{\mathbf{n}}) \hat{\mathbf{n}} - \sqrt{k_2^2 - k_1^2 + (\mathbf{k}_1 \hat{\mathbf{n}})^2} \hat{\mathbf{n}}. \quad (5.26)$$

I divide by  $k_2$  with  $\mathbf{k}_2/k_2 = \hat{\mathbf{t}}$  and  $\mathbf{k}_1/k_2 = \eta \hat{\mathbf{i}}$  in order to introduce unit direction vectors  $\hat{\mathbf{i}}$  and  $\hat{\mathbf{t}}$  for incident and outgoing light. The relative index change across

## 5. Raytracing for spatio-angular microscopy

the interface is  $\eta = n_1/n_2$ . With these substitutions equation (5.26) becomes:

$$\hat{\mathbf{t}} = \eta \hat{\mathbf{i}} - \eta (\hat{\mathbf{i}} \hat{\mathbf{n}}) \hat{\mathbf{n}} - \sqrt{1 - \eta^2 + \eta^2 (\hat{\mathbf{i}} \hat{\mathbf{n}})^2} \hat{\mathbf{n}} \quad (5.27)$$

$$= \boxed{\eta \hat{\mathbf{i}} - \left( \eta \hat{\mathbf{i}} \hat{\mathbf{n}} + \sqrt{1 - \eta^2(1 - (\hat{\mathbf{i}} \hat{\mathbf{n}})^2)} \right) \hat{\mathbf{n}}} \quad (5.28)$$

When the expression under the square root is negative a reflection occurs instead of refraction. Note that in my application total internal reflection (TIRF) just corresponds to a loss of the beam, because the reflected beam no longer contributes to sample illumination. The exact direction of this beam is not relevant in this case but I give the equation here for completeness' sake.

In the case of reflection, the tangential component is invariant and the normal component inverts sign:

$$\mathbf{k}_2 = \mathbf{k}_{1t} - \mathbf{k}_{1n} \quad (5.29)$$

$$= \mathbf{k}_1 - 2\mathbf{k}_{1n} \quad (5.30)$$

$$= \mathbf{k}_1 - 2(\mathbf{k}_1 \hat{\mathbf{n}}) \hat{\mathbf{n}} \quad (5.31)$$

$$\hat{\mathbf{t}}_{\text{TIR}} = \boxed{\hat{\mathbf{i}} - 2(\hat{\mathbf{i}} \hat{\mathbf{n}}) \hat{\mathbf{n}}} \quad (5.32)$$

## 5.2. Refraction through lenses

validity of thin lens model

An ideal lens is infinitesimally thin and is completely defined by its focal length. For an ideal lens the focal length is independent of the incidence angle but in practice, the model of the thin lens is only valid for lenses of long focal length and for paraxial rays that subtend very small angles from the optical axis.

principal planes

For a better approximation of refraction through a thick lens the two principal planes of the thick lens are calculated and the ray is shifted between them axially (Smith 2000). The principal plane of a thick lens is located on the intersection between an incident beam  $\hat{\mathbf{i}}$ , that is parallel to the optical axis, and the transmitted beam  $\mathbf{r}$ . Just as the focal length, the principal planes are a property of lenses that are only defined in the paraxial limit. There are always two principal planes, one for each of the two possible illumination directions. The distances between each principal plane and its corresponding focus point (the intersection of  $\mathbf{r}$  with the optical axis) are identical, and define the focal length.

As already mentioned in section 1.3.1 on page 21 a microscope objective is a lens which is corrected to have a constant focal length for rays of widely varying

## 5. Raytracing for spatio-angular microscopy

incidence angle. In this case, the principal surface is no longer a plane but is deformed into a spherical surface. After introducing the formulas for the thin lens in the next section, I show in section 5.2.2 how to carry over those formulas to a model that describes an aplanatic lens with immersion.

### 5.2.1. Refraction through a paraxial thin lens

First I describe the refraction by a thin lens: The incident beam with direction  $\hat{i}$  hits the lens at the point  $\rho$ . A line parallel to  $\hat{i}$  through the centre  $O$  of the lens defines the point on the focal plane, which will be intersected by the transmitted ray  $r$  as well.

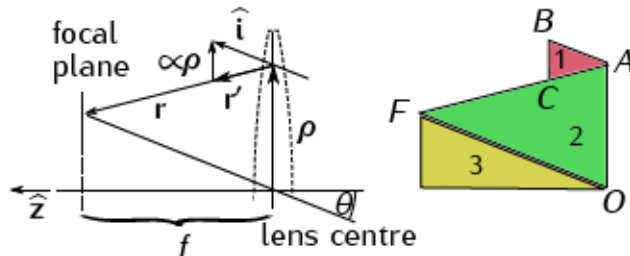


Figure 5.3.: Construction of a ray that is refracted through a thin lens. The incident beam with direction  $\hat{i}$  (from right) hits the lens at the point  $\rho$ . This diagram is inspired by a figure in Hwang and Lee (2008).

The red triangle 1 with the points  $ABC$  is similar to green triangle 2 with points  $FOA$ . All three angles are identical because each of the lines are parallel:  $\overline{CB} \parallel \overline{OA}$ ,  $\overline{FA} \parallel \overline{CA}$  and  $\overline{AB} \parallel \overline{OF}$ ,  $\hat{i}$ . The side  $\overline{OF}$  is hypotenuse of the yellow right angled triangle 3. Its adjacent with respect to the angle  $\theta$  has length  $f$ . Therefore one can deduce the length  $|\overline{OF}| = f / \cos \theta$ .

Between the two similar triangles, the following relation can be used to calculate the length  $|\overline{BC}|$ :

$$\frac{|\overline{BC}|}{|\overline{BA}|} = \frac{|\overline{OA}|}{|\overline{OF}|} \quad (5.33)$$

$$\frac{|\overline{CB}|}{1} = \frac{\rho}{f / \cos(\theta)}. \quad (5.34)$$

Given its length, the vector  $\overrightarrow{CB}$  is now calculated by its length and the direction  $\rho$ . With this vector and  $\hat{i}$  one can now obtain the (arbitrarily scaled) transmitted vector  $r'$ . Only the two framed equations need to be implemented to calculate

## 5. Raytracing for spatio-angular microscopy

refraction on a thin lens with the procedure from above:

$$\rho = (x_0, y_0, 0)^T = \rho(\cos \phi, \sin \phi, 0)^T \quad (5.35)$$

$$\phi = \arctan(y_0/x_0) \quad (5.36)$$

$$\cos \theta = \boxed{\hat{i} \hat{z}} \quad (5.37)$$

$$r' = \hat{i} - \frac{\cos \theta}{f} \rho \quad (5.38)$$

$$r = \boxed{\frac{f}{\cos \theta} \hat{i} - \rho} \quad (5.39)$$

with the axial unit vector  $\hat{z} = (0, 0, 1)^T$ .

### 5.2.2. Refraction through high aperture objective (illumination)

Now I modify the results of the calculation from the previous section to treat an aplanatic immersion objective (Hwang and Lee 2008). I account for the immersion

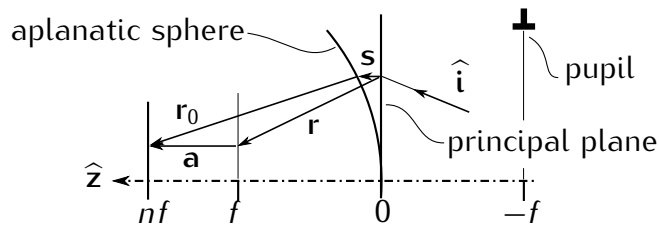


Figure 5.4.: Ray construction for a high numerical aperture objective with immersion. As opposed to a thin air lens the objective's focal length needs to be corrected by the focus difference vector  $\mathbf{a}$  to accommodate for the immersion and one must take into account spherical principal surface (aplanatic surface).

medium by axially shifting the focal plane in sample space to  $nf$  using the difference vector  $\mathbf{a}$ , i.e. in an immersion medium with  $n = 1.52$  the focus moves further away from the principal plane.

$$\mathbf{a} = \boxed{f(n - 1)\hat{z}} \quad (5.40)$$

$$R = \boxed{nf} \quad (5.41)$$

In order to account for the curvature of the aplanatic surface, the origin of the transmitted ray is axially shifted by a  $\rho$ -dependent sag  $s$  from the principal

## 5. Raytracing for spatio-angular microscopy

plane onto the aplanatic surface:

$$\mathbf{s} = \left( R - \sqrt{R^2 - \rho^2} \right) \hat{\mathbf{z}} \quad (5.42)$$

The final ray exiting the objective has the direction  $\mathbf{r}_0$ :

$$\mathbf{r}_0 = [\mathbf{r} + \mathbf{a} - \mathbf{s}]. \quad (5.43)$$

All microscope lenses that come into consideration for use in the system that we built are designed as an aplanatic lens. The model described by above formulas is therefore very well suited to represent the objectives when we run our illumination optimization algorithm to find illumination patterns for the two SLM in our spatio-angular microscope.

In the paper Hwang and Lee (2008) the authors demonstrate the viability of this model by comparing its results with a full raytrace through a  $100\times$  objective with  $NA = 1.4$ . There, focus displacement errors are less than  $130\text{ nm}$  for a field of  $86.4\text{ }\mu\text{m}$  radius. This is perfectly adequate for our application.

One might think it would be better to know the exact objective parameters, i.e. glasses, curvatures and vertex positions of lens surfaces. These details are, however, to my knowledge not published by any manufacturer. In addition alignment of the components plays a prominent role in building high performance objectives. Therefore just the design parameters alone probably do not provide a better model of a microscope objective. They would have to be augmented with performance measurements of the individual objective, e.g. point spread functions in different regions of the field.

### 5.2.3. Reverse path through oil objective (detection)

Now I consider an oil immersion objective in the detection direction, tracing rays from the sample into the pupil.

For that I present two approaches. The first and simpler one utilizes the fact that a perfect microscope lens converts ray angle in the sample in a linear manner into positions on the pupil. This approach is sufficient when calculating pupil plane SLM patterns for samples in an index matched embedding medium.

In the second approach I additionally calculate the angle in which rays emerge from the pupil. For a perfectly aplanatic lens this would hardly be an advantage but the formulas will be modified to take into account aberrations.

## 5. Raytracing for spatio-angular microscopy

Easy case: back focal plane positions only

If the points of ray intersection of the back focal plane are sufficient, a full raytrace is not necessary. This is the case with aberration-free imaging, i.e. when the sample is embedded in an index matched medium and we want to calculate a pattern for the pupil plane SLM. Then it is possible to ignore the starting points of rays in the specimen and just work with their directions.

A unit ray direction  $\hat{i} = (x, y, z)^T$  in sample space is transformed into a position  $r_b = (x', y')^T$  in the back focal plane of the objective. The azimuthal angle  $\phi$  isn't changed when going through the objective. The polar angle  $\theta$  defines how far off axis the back focal plane is hit.

$$\phi' = \phi = \arctan(y/x) \quad (5.44)$$

$$\theta = \arcsin(\sqrt{x'^2 + y'^2}) \quad (5.45)$$

$$r_b = r_b (\cos \phi', \sin \phi')^T, \quad \text{with } r_b = nf \sin \theta \quad (5.46)$$

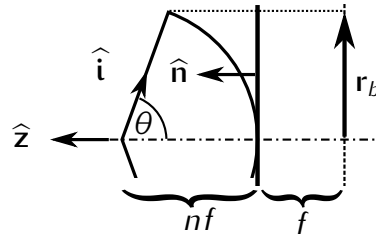


Figure 5.5.: Schematic for tracing a ray direction  $\hat{i}$  from sample space into the back focal plane. The bigger the angle between  $\hat{i}$  and the optical axis, the further outside the ray will pass through the back focal plane.

Full raytrace through oil objective in detection direction

Now I discuss the general case and calculate both the origin and the direction of a ray emerging from the back focal plane. This is necessary in order to trace light bundles from the specimen into the plane of the camera (or focal plane SLM). In the next section I will further modify these formulas to incorporate aberrations due to non-index matched embedding medium.

The position of the objective is defined by its principal point  $c$  and the normal  $\hat{n}$  (directed along optical axis towards sample space). The incident ray is defined by its starting point  $p$  and the direction  $\hat{i}$ . First I calculate the centre of the

## 5. Raytracing for spatio-angular microscopy

aplanatic sphere  $\mathbf{g}$  (see Figure 5.6).

$$\mathbf{g} = \mathbf{c} + nf\hat{\mathbf{n}}. \quad (5.47)$$

Then I obtain the position  $\mathbf{p}'$  by intersecting the incident ray and the plane

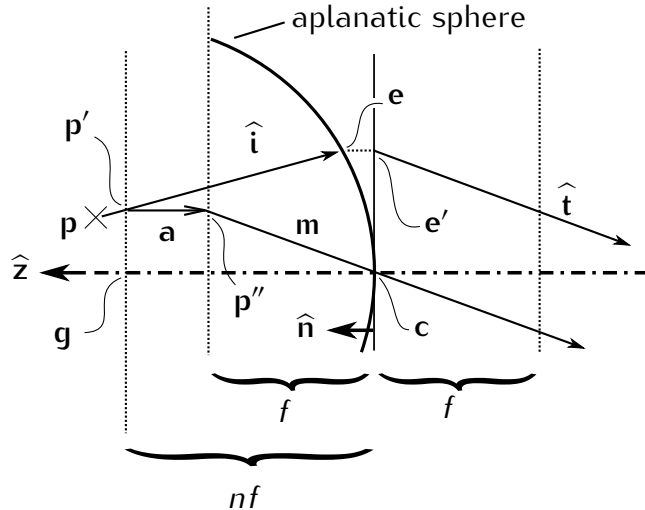


Figure 5.6.: Construction to find the transmitted ray through an oil immersion objective from a point within the sample.

perpendicular to the optical axis through the centre  $\mathbf{g}$  of the aplanatic sphere. The focus difference vector  $\mathbf{a}$  is defined by its length and the optical axis. It can be used to calculate an intermediate point  $\mathbf{p}''$ .

$$\mathbf{a} = -f(n-1)\hat{\mathbf{n}} \quad (5.48)$$

$$\mathbf{p}'' = \mathbf{p}' + \mathbf{a}. \quad (5.49)$$

The point  $\mathbf{p}''$  has been shifted, so that an aplanatic air lens would image it exactly as the oil objective would image  $\mathbf{p}'$ . One can use  $\mathbf{p}''$  to find the direction  $\hat{\mathbf{t}}$  of the transmitted ray. It is just the normalized difference vector  $\mathbf{m}$  to the principal point  $\mathbf{c}$ .

$$\mathbf{m} = \mathbf{c} - \mathbf{p}'' \quad (5.50)$$

$$\hat{\mathbf{t}} = \mathbf{m}/|\mathbf{m}|. \quad (5.51)$$

As a last step I calculate the starting point  $\mathbf{e}'$  of the transmitted ray by intersecting the incident ray with the aplanatic sphere (in point  $\mathbf{e}$ ) and axially shifting this point onto the principal plane.

## 5. Raytracing for spatio-angular microscopy

Note: In order to verify the correctness of these formulas or their implementation it is possible to compare the algorithms of this section (for tracing in detection direction) and section 5.2.2 (for illumination direction).

### 5.2.4. Treatment of aberration (detection)

Now I will extend the formulas of the previous section to include aberrations due to a non-matched embedding medium  $n_e \neq n$ .

I consider a ray originating in point  $p$  with direction  $\hat{i}$  within an embedding medium of index  $n_e$ . I determine the intersection  $f$  of the ray with the “cover slip–embedding” interface and refract to obtain  $\hat{i}'$ . Then I calculate the time  $t$  a photon takes, to travel from  $p$  to the interface  $f$ :

$$t = |\mathbf{f} - \mathbf{p}| \frac{n_e}{c} \quad (5.52)$$

and extend the path of the photon backward along the direction  $\hat{i}'$  (corrected for the refraction at the “cover slip–embedding” surface) by the distance  $tc/n$ . This results in the corrected position  $p'$  that indicates where the photon would have originated if the embedding medium were index matched. Now I can apply the equations from the previous section on the ray defined by  $p'$  and  $\hat{i}'$  to obtain the transmitted ray in the pupil.

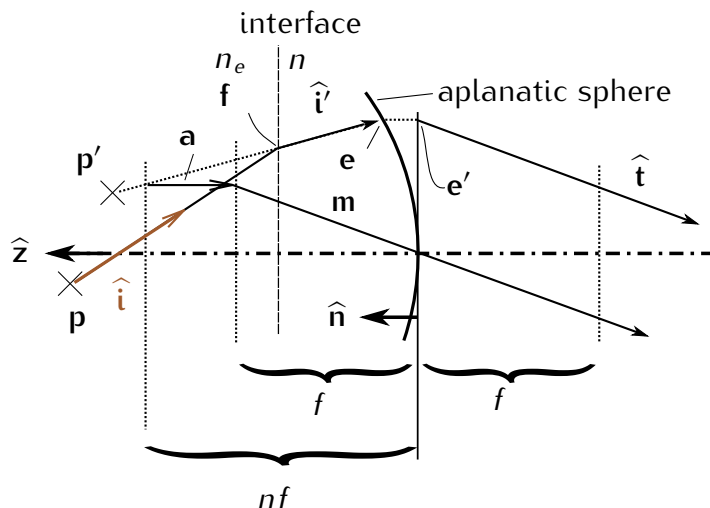


Figure 5.7.: Construction of an oil immersion objective with a non-index matched embedding medium.

### 5.3. Sphere projection

While the previous sections have described a fairly general raytracer, this section is very technical and relates to the specific problem to represent a fluorophore distribution as a model of spheres and simulate it with as few rays as possible.

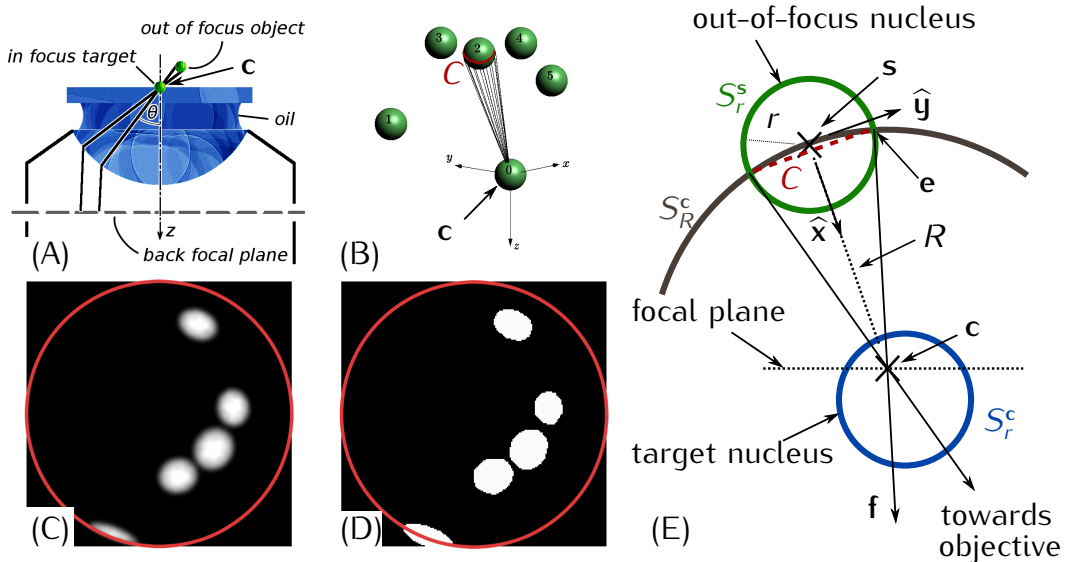


Figure 5.8.: (A,B,E) Diagrams depicting the geometry of a sample of spherical nuclei. The main text derives the rays on the cone through the target point  $c$  that touches an out-of-focus nucleus in the curve  $C$ . (C) Map of the pupil plane. A ray is sent from each point of the pupil plane into the target point  $c$ . The brightness value in the pupil map indicates the length of the segment of the ray that intersects out-of-focus nuclei. (D) Approximation of the map in (B) using the technique discussed in this section with a minimum number of rays per out-of-focus nucleus.

Figure 5.8 A) shows two rays emanating from the pupil plane and illuminating the target point  $c$ . For Figure 5.8 C) rays were traced from each point of the pupil plane through the target point  $c$ . The brightness of the map in Figure 5.8 C) indicates the length of ray segments for rays that intersect with out-of-focus rays.

Creating such an image in the illumination direction requires to trace a lot of rays (at least  $50 \times 50$ ). In order to reduce the computational effort, I reverse the calculation direction and trace rays starting from the periphery of out-of-focus nuclei through the target point  $c$  in order to determine appropriate “shadow masks” in the pupil plane (as depicted in Figure 5.8 D)). Already with six rays per nucleus, this approach can determine very good masks.

Now I explain how to select good points on the periphery of out-of-focus nuclei in order to allow this calculation. I utilize the geometry in Figure 5.8 E).

## 5. Raytracing for spatio-angular microscopy

The tangents of an out-of-focus sphere  $S_r^s$  centred at  $s$  with radius  $r$  that pass through the target  $c$  form a double cone (assuming  $c$  is outside of  $S_r^s$ ). The tangents touch the surface of the sphere  $S_r^s$  in the circle  $C$ . We will find a parametric expression for the points on the circle  $C$  by intersecting the sphere  $S_r^s$  and the sphere  $S_R^c$  centred at  $c$  with radius  $R = |c - s|$  which is the distance from the target to the centre of the out-of-focus sphere.

In order to find a point  $e$  where a tangent touches the out-of-focus sphere, it is sufficient to solve the following equation in a two-dimensional coordinate system with the origin in the centre  $s$  of the out-of-focus sphere:

$$(x - R)^2 + y^2 = R^2 \quad (5.53)$$

$$x^2 + y^2 = r^2 \quad (5.54)$$

There are two solutions:

$$x_1 = \frac{r^2}{2R} \quad (5.55)$$

$$y_{1/2} = \pm \frac{r}{2R} \sqrt{4R^2 - r^2} \quad (5.56)$$

In the case  $R \leq r$  the out-of-focus nucleus is very close to the target, obviating the reason to do the projection in the first place. In the more useful case of  $R > r$  there are two solutions but either one of them is sufficient to define the circle  $C$ .

I construct two normalized vectors  $\hat{x}$  and  $\hat{y}$  that span the coordinate system, in order to transform the solution from 2D into 3D. The direction of  $\hat{x}$  is given by the difference vector between target  $c$  and nucleus centre  $s$ . The direction  $\hat{y}$  must be perpendicular to  $x$  and I ensure this by calculating the cross product of  $x$  with an arbitrary vector  $\zeta$ . The only constraint on the vector  $\zeta$  is that it must not be colinear with  $x$ . Therefore I choose  $\zeta$  to be a vector along the  $z$ -axis, except when  $x$  comes close to the  $z$ -axis. Then I choose  $\zeta$  to be along the  $y$ -axis.

$$x = c - s \quad (5.57)$$

$$y = x \times \zeta \quad \text{with } \zeta = \begin{cases} (0, 0, 1)^T & \text{when } |x_z| < \frac{2}{3}|x| \\ (0, 1, 0)^T & \text{else} \end{cases} \quad (5.58)$$

$$\hat{x} = x/|x|, \quad \hat{y} = y/|y| \quad (5.59)$$

Now I can sample the intersection circle  $C$  in order to create viable starting points  $e$  for tangential rays. Let  $M_\phi^c$  be a rotation matrix that rotates a vector by angle

## 5. Raytracing for spatio-angular microscopy

$\phi$  around an axis  $\hat{c}$ . A point  $e$  on the circle is then defined using one solution from equations (5.55) and (5.56). The ray direction  $f$  is then easily obtained:

$$e(\phi) = s + x_1 \hat{x} + y_1 M_\phi^{\hat{x}} \hat{y} \quad (5.60)$$

$$f(\phi) = c - e. \quad (5.61)$$

Tracing a sufficient number of rays (e.g. 7) with direction  $f$  for different angles  $\phi$  to the back focal plane gives the projection of the intersection circle  $C$ . Note that this projection in general is not a circle anymore.

For practical reasons I project the vector  $\hat{x}$  as well. I use it as a centre to rasterize the shape in the pupil plane as a fan of triangles.

## 5.4. Conclusion

In this chapter I have given an overview on the raytracer that I use as a component in the illumination optimization algorithm for the spatio-angular microscope. This software is tailored to the problem of imaging with an aplanatic lens. I optimized the calculations so that illumination patterns can be determined in real time, while the device operates.

I described an algorithm that can account for aberration that occurs when a sample is not embedded in index matched medium. On the one hand this has a negative impact on the resolution of the detected images already for small penetration depths ( $\sim 10 \mu\text{m}$ ) but it enables the interesting approach of highly inclined and laminated optical sheet microscopy (see section 2.1.2). In this case, a window on the edge of the pupil is illuminated so that rays approach the “cover slip–medium” surface close to the critical angle of total reflection — and after refraction they will traverse the medium in a very steep angle. To illuminate the proper position in the field, the window that is displayed on the focal plane SLM must be moved in order to compensate for any, but mainly spherical, aberrations.

Note that ray optics are not a sufficient approximation, when intensity features in the scale of the wavelength are to be investigated. Small features would mean that only a few pixels of the focal plane SLM would be enabled. This would mean that information of the pupil plane SLM pattern is heavily filtered and no simultaneous tight angular control would be possible. Therefore, algorithms that are based on code in this chapter must generate patterns with big feature sizes. Features on the pupil plane SLM should be larger than several percent of the pupil diameter.

## 6. Experimental results with spatio-angular microscope

Here I describe some of our experiments that demonstrate the functioning of our spatio-angular microscope prototype.

In the first experiment, I use total internal reflection which prevents high angles from reaching the sample when the refractive index of the embedding medium is lower than that of the immersion medium. This is a simple way to show that angular illumination control works.

In the second experiment, we measure the three-dimensional light distribution in the sample by bleaching a fluorescent gel layer.

Then I describe another experiment, that replicates the problem of imaging live specimens. The task is to localize three-dimensionally distributed beads and then image them individually using an optimized excitation light distribution.

### 6.1. Measuring acceptance angle for three different embedding media

As one of the first attempts to use the spatio-angular illumination system, I devised an experiment to determine the acceptance angle of a microscope objective as a function of the embedding medium.

For the measurement, a thin layer of fluorophores was applied with a marker pen (Stanger, yellow-green) on three microscope slides. After drying, a drop of a liquid embedding medium was added to two of the samples (immersion oil ( $n = 1.52$ ) and water ( $n = 1.33$ )). Then cover slips were added to all three samples and sealed with nail polish.

During the measurement, the focal plane SLM projected a disk with  $30\ \mu\text{m}$  diameter on the fluorescent plane. The illumination angle was varied by stepping a window of  $15 \times 15$  pixels (equivalent to 1/17th of the pupil diameter) over the pupil plane SLM.

scan pupil plane SLM

## 6. Experimental results with spatio-angular microscope

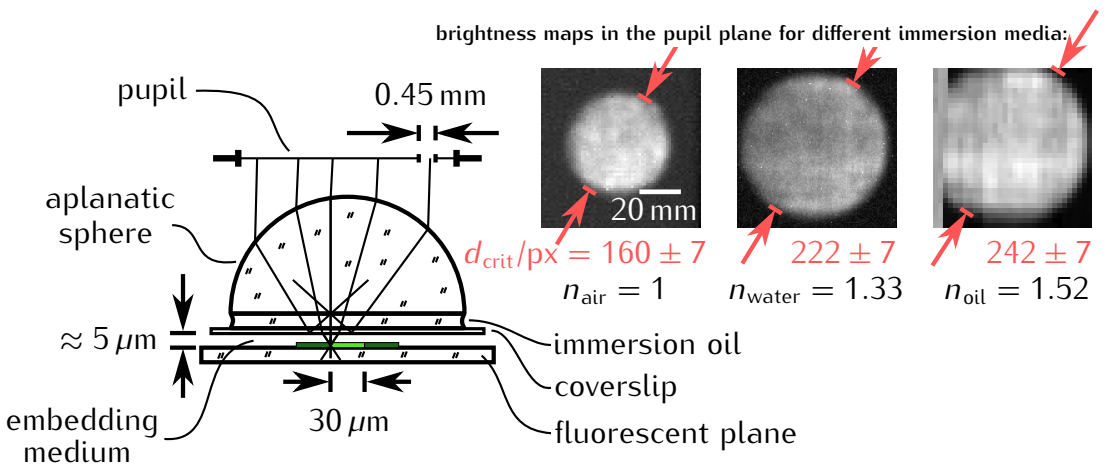


Figure 6.1.: A fluorescent plane on a slide is embedded in oil, water or air. The thickness of the embedding medium is approximately  $5 \mu\text{m}$ . The focal plane SLM illuminates a disk with  $30 \mu\text{m}$  diameter while a window of  $15 \times 15$  pixels is scanned over the MMA. The window corresponds to a square with  $0.45 \text{ mm}$  on the side as opposed to  $7.2 \text{ mm}$  pupil diameter. The red numbers indicate the diameter of the bright circle in pixels of the pupil plane SLM.

For each angle, the sum of all fluorescence light reaching the camera is recorded. The fluorescence intensity for each window position on the pupil plane SLM are depicted in the three images in Figure 6.1. These images contain a bright disk whose diameter  $d_{\text{crit}}$  is growing with the index of the embedding medium. The center of the disk corresponds to the optical axis of the objective. Points in the interior of the circle have an almost constant intensity (residual fluctuations can be attributed to non-uniformity of the illumination of the pupil plane SLM). For oil immersion, the measured diameter of the disk corresponds to the diameter of the pupil which is:

$$d_{\text{pupil}}^{(\text{theory})} = 2\text{NA} \cdot f_{\text{obj}} = 7.2 \text{ mm}, \text{ with } f_{\text{obj}} = f_{\text{TL}}/M = 164.5 \text{ mm}/63 = 2.61 \text{ mm} \quad (6.1)$$

I used an objective with  $M = 63\times$  magnification and a numerical aperture of  $\text{NA} = 1.38$  for the experiment. Therefore, the size of an MMA pixel in the pupil plane is  $\Lambda' = 7.2 \text{ mm}/(242 \pm 7) = 30 \mu\text{m} \pm 1 \mu\text{m}$ .

If the index of the embedding medium is less than the index of the immersion medium, then total internal reflection occurs on the interface between cover slip and embedding medium for high incidence angles. The excitation light can then no longer reach the sample. Therefore, the disks in the brightness maps for water and air are smaller.

## 6. Experimental results with spatio-angular microscope

The relationship between the diameter  $d_{\text{crit}}$  of the bright circle and the critical angle of total reflection at the interface between cover slip ( $n_{\text{cs}} = n_{\text{oil}} = 1.52$ ) and embedding medium ( $n_{\text{emb}}$ ) is as follows:

$$d_{\text{crit}} = 2n_{\text{oil}}f_{\text{obj}} \sin \theta_{\text{crit}} = 2n_{\text{oil}}f_{\text{obj}} \frac{n_{\text{emb}}}{n_{\text{oil}}}, \quad \text{with } \theta_{\text{crit}} = \arcsin \left( \frac{n_{\text{emb}}}{n_{\text{oil}}} \right) \quad (6.2)$$

A comparison between the ratios of the measured diameters and the ratios of the refractive indices in Table 6.1 shows that the measurement is in good agreement with the theory.

	$n_{\text{emb}}/n_{\text{oil}}$	$d_{\text{crit}}^{\text{emb}}/d_{\text{crit}}^{\text{oil}}$
water	0.875	$0.88 \pm 0.05$
air	0.658	$0.64 \pm 0.04$

Table 6.1.: Comparison showing that the measurement of the angle of acceptance for two different embedding media corresponds to the theory.

## 6.2. Measuring the light distribution by bleaching a fluorescent gel

The above-described experiment allows only an indirect measurement of the effects of angular control in our microscope. Now I describe an experiment where fluorophores in a slab of several microns thickness are bleached. This allows a more direct measurement of the light distribution in the sample by imaging the bleached region with a confocal microscope.

As a sample we use a 4% agarose gel containing fluorescently labeled DNA plasmids. The exact sequence of the plasmids is irrelevant. They only serve as carriers for the fluorophore (SYBR Save DNA gel stain, Invitrogen). Exposed samples are stable for several weeks and no unbleached fluorophores diffuse to bleached regions. The gel was chosen and prepared by Florian Rückerl with whom I conducted this experiment. This has been reported in Rückerl et al. (2013).

During the experiment, the focal plane SLM displays three different patterns (all dark, all bright, bright vertical bar) and the pupil plane SLM displays eight different patterns (all dark, all bright, and 6 circular windows). The focal plane SLM was projected as far into the gel layer as the working distance of the objective would allow and combinations of the pupil plane SLM and focal plane

## 6. Experimental results with spatio-angular microscope

SLM patterns were bleached into the sample with various exposure times overnight. Utilizing a XY-stage, the sample was moved by 0.4 mm between exposures.

The laser delivers a continuous beam of 473 nm wavelength with 400 mW power. It is modulated using an acousto-optic modulator (AOM) so that only during the camera integration time (20 ms), and when the two SLM are in a defined state, light can excite the sample. The modulated beam (duty cycle < 50%) has an average power of 15 mW. For this experiment, I illuminate the rotating micro-lens array and integrator rod directly (without fibre bundle). Behind the integrator tunnel, there were still 7 mW average power and in front of the dichromatic mirror of the microscope, a mere 17  $\mu$ W (with both SLM showing a white pattern, giving an illuminated field diameter of 40  $\mu$ m in the sample).

Given the low transmission I decided to leave out the fibre bundle as this would reduce the overall efficiency by an additional factor of two. This led, however, to inhomogeneous illumination of the pupil so that in hindsight it would have been better to use the fibre bundle.

Figure 6.2 a) is a mosaic of confocal images (LSM700, Zeiss) in the vicinity of the plane in the bleached gel where the focal plane SLM was focused. The bleached areas form a pattern of 11  $\times$  6 exposures. The bleaching dose varies with the vertical direction as indicated by the accumulated exposure times (consisting of numerous individual 20 ms camera integrations). Strong in-focus bleaching becomes evident for bleach durations of 30 s and higher, corresponding to a light dose above 40 J/cm<sup>2</sup> in the focal plane.

Along the horizontal mosaic direction, different SLM patterns were displayed. The two areas at both outer borders (column 0 and 10) were bleached with full angular and spatial exposure. The next columns 1 and 9 give an indication of how well both the SLMs can produce black as no bleaching pattern is evident in these places.

The central areas (columns 2–9, indicated with green circles) were all displaying a vertical bar on the focal plane SLM, while the pupil plane SLM displayed a circular window, varying the incidence angle. The first bar from the left (column 2) was illuminated with all angles. Figure 6.2 b) shows a three-dimensional representation of a confocal recording of the bleached area. Unfortunately, three separate bundles are visible, indicating insufficient uniformity of the illumination. As the non-uniformities are not rotationally symmetric with respect to the optical axis, the bundles propagate at slightly different angles.

The images in Figure 6.2 c) and d) show confocal measurements of the area bleached under restricted angles (columns 3 and 6). For this, a circular window

overall light efficiency of our illumination system

observed bleaching patterns

## 6. Experimental results with spatio-angular microscope

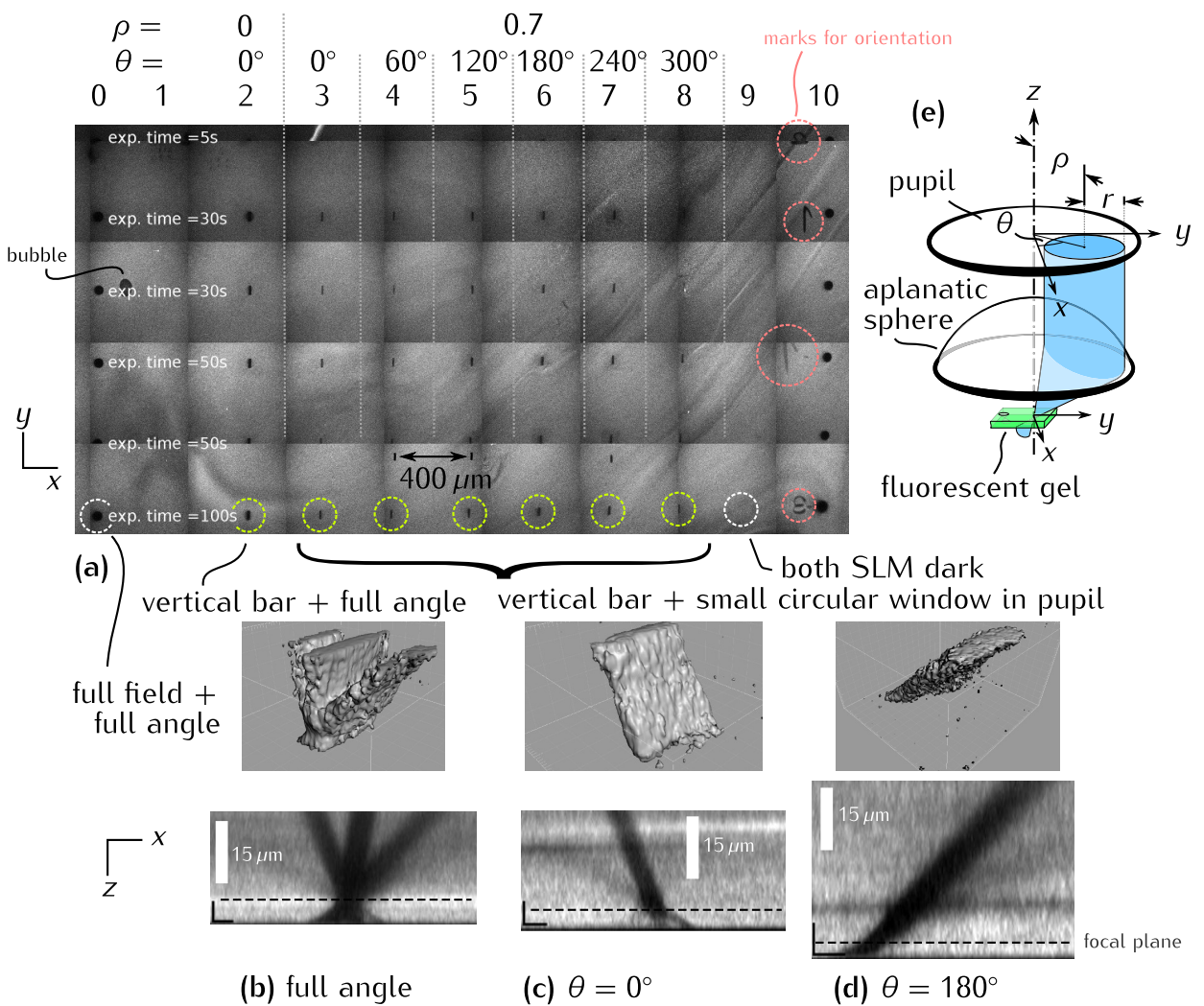


Figure 6.2.: Confocal images of a fluorescent gel that has been bleached with spatio-angular illumination. **(a)** Overview image of the exposure series. Eleven focal plane patterns were bleached for 5, 30, 50 or 100 seconds. Exposure for 30 s corresponds to a light dose of 40 J/cm<sup>2</sup>. **(b,c,d)** Rendering of confocal stack of regions that were bleached from different angles. **(e)** Geometry of the window on the pupil plane SLM. The confocal measurements and images were kindly provided by Florian Rückerl (Institut Pasteur).

## 6. Experimental results with spatio-angular microscope

with radius  $r = 0.3$  was displayed on the pupil plane SLM, where the coordinates  $\rho$  and  $r$  are given relative to the pupil radius. For  $\rho = 1$  the window would be centered on the periphery of the pupil, as indicated in the drawing of Figure 6.2 e).

Dark digits in the mosaic (framed by red circles) are landmarks that were retrospectively bleached into the specimen for orientation during acquisition with the confocal microscope.

### 6.3. Spatio-angular illumination of three-dimensionally distributed beads

The next experiment models the imaging conditions of a biological sample. For this, beads of three microns diameter were distributed in agarose gel. The goal is to first localize the beads and subsequently utilize the knowledge of their three-dimensional distribution to find patterns for the pupil plane SLM to excite and image the beads individually while avoiding exposure of out-of-focus beads.

widefield baseline

First of all, I show a focal series of wide field images with  $z$ -steps of one micron and illumination of the full field using all angles in the left mosaic of Figure 6.3. These recordings show how several beads sequentially come into focus. In order to facilitate the discussion, the beads have been labeled with a number. Unfortunately, the gel contributes a relatively high background fluorescence from which the blurred images of beads are no longer distinguishable after only three microns of defocus. For this sample of sparse beads, their three-dimensional distribution could easily be determined from these widefield images. In a more dense sample, e.g. a higher bead concentration or nuclei in an embryo, this is no longer possible.

optical sectioning

In those cases it is useful to utilize structured illumination to separate out-of-focus and in-focus fluorescence. The mosaic on the right of Figure 6.3 shows the computed optical sections from four raw images per slice. The raw images are displayed in Figure 6.4. The optical sections contain relatively distinct vertical reconstruction artifacts. These can be avoided by using the HiLo reconstruction method which has the additional advantage of only needing two raw images per slice.

bead localization

However, the HiLo method needs considerably more programming. Also, the artifacts have no effect on the localization precision of the algorithm. For localization, I determine the center of each bead by finding local maxima after applying a three-dimensional difference of Gaussian filter (matched to the bead diameter).

## 6. Experimental results with spatio-angular microscope

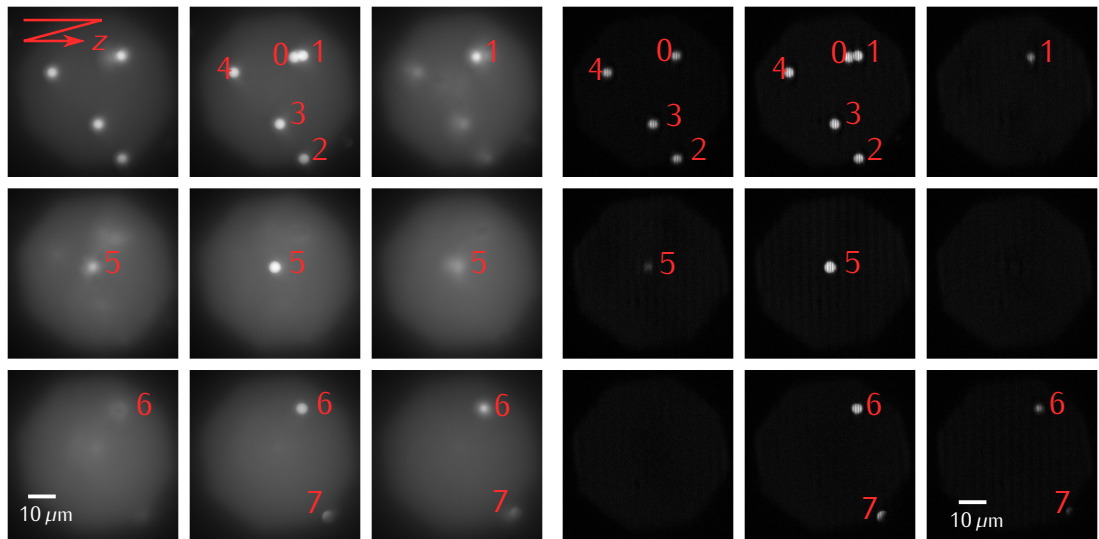


Figure 6.3.: **left:** Wide field focus series of a three-dimensional distribution of yellow-green beads in agarose gel. Sampling in  $z$  is  $1 \mu\text{m}$ . **left:** Computationally sectioned images of the same sample. The corresponding raw images are shown in Figure 6.4.

The resulting coordinates are depicted in the inlay in Figure 6.5.

In the next step, each bead is illuminated individually by displaying a bright disk at the corresponding position on the focal plane SLM, while the pupil plane SLM displays a mask which prevents exposure of out-of-focus beads. This mask is calculated automatically with a raytracer and utilizes the three-dimensional model of the bead distribution.

The eight camera images of the individual beads are shown in the two top rows in Figure 6.5. Unlike Figure 6.3, no focal series is shown. Each image is focused on a single bead. The corresponding pupil plane SLM masks are shown in the two rows below. I will briefly describe the construction of the masks using bead 4 as an example. According to the three-dimensional diagram in the inlay in Figure 6.5, bead 4 is on the edge of the bead distribution. The smallest angle relative to the optical axis is between the connecting line of bead 4 and 7. Therefore, the single "shadow" (indicated with an arrow) in the pupil plane mask corresponds to bead 7. All other beads would only be illuminated by light that strikes bead 4 under a larger angle. Bead 6 and maybe bead 5 combine to the second shadow on the periphery of the pupil.

The camera images of bead 2 and 7 in Figure 6.5 stand out because they are completely dark. The reason is that the registration between the focal plane SLM and camera has shifted by a few microns between localizing the beads and their

description of pupil  
plane masks

stability

## 6. Experimental results with spatio-angular microscope

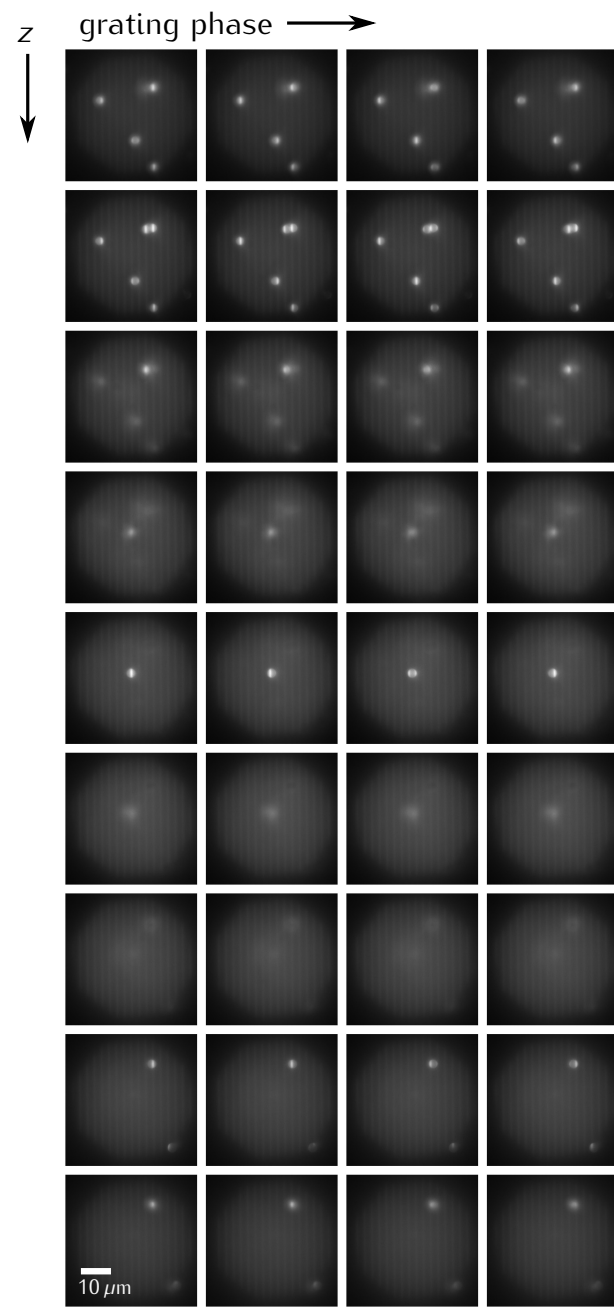
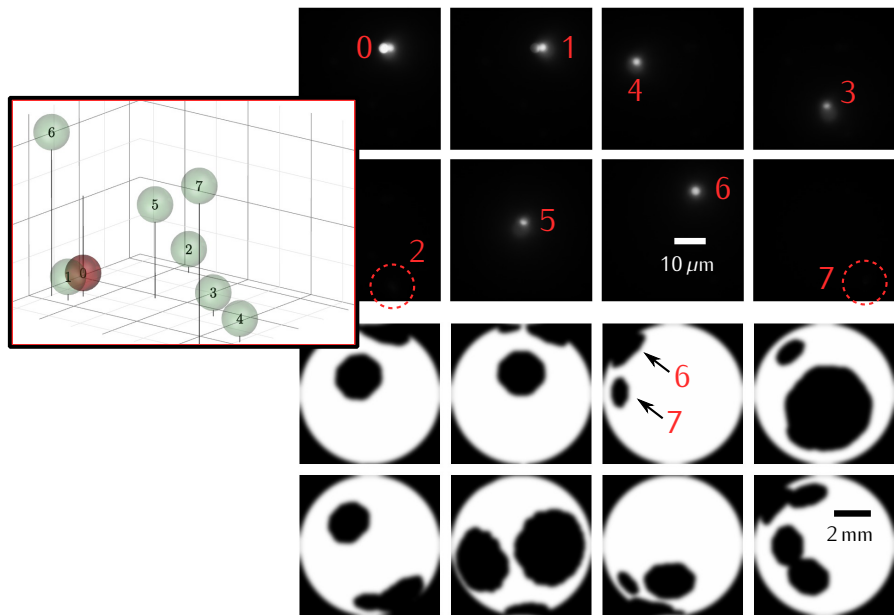


Figure 6.4.: Focal stack with structured illumination of the same sample as Figure 6.3. For each  $z$ -slice (rows) four exposures with different grating phase (columns) were acquired.

## 6. Experimental results with spatio-angular microscope



**Figure 6.5.: left inlay:** Coordinates of the beads from Figure 6.3. **top mosaic:** Camera images with spatio-angular illumination of the beads. This is not a focus series but an image of each individual bead. **bottom mosaic:** Corresponding patterns of the pupil plane SLM.

spatio-angular exposure. This type of error was corrected by removing rubber feet from the microscope and screwing it directly to the metal table.

A more interesting effect is visible in the camera image of bead 5. Only the bottom half of the bead is illuminated but due to fluorescence in the agarose gel, the circular area that is illuminated by the focal plane SLM is still visible. This effect would predominantly occur in samples where fluorescent areas are not sharply defined. As exposures with light from different angles will contain different contributions of background fluorescence, it is not clear whether individual sub-images of the spatio-angular microscope can be joined into a seamless image. The image quality of confocal microscopes hardly seems achievable by our system. Cells in an embryo can probably be counted and tracked, but a quantitative measurement of the fluorescence seems difficult.

I imaged the beads in Figure 6.5 with both full angles and optimized angles. The selective illumination of individual beads using only the focal plane SLM and full angles already reduced the background fluorescence from other beads and the gel significantly. Unfortunately, it is not possible to discern any further improvement with additional angular control. I think the fluorescence from out-of-focus beads can not be detected in the presence of photon shot noise of the fluorescence from the gel. Angular control will still have a positive effect because out-of-focus

artifacts

comparison spatial  
control and only  
angular control

## 6. Experimental results with spatio-angular microscope

beads are not uselessly exposed — it is just not possible to measure this in this particular sample.

### 6.4. Angular illumination and a higher concentration of beads

In order to measure the influence of angular illumination control directly, I made another sample with higher concentration of beads in an agarose gel with significantly less fluorescence.

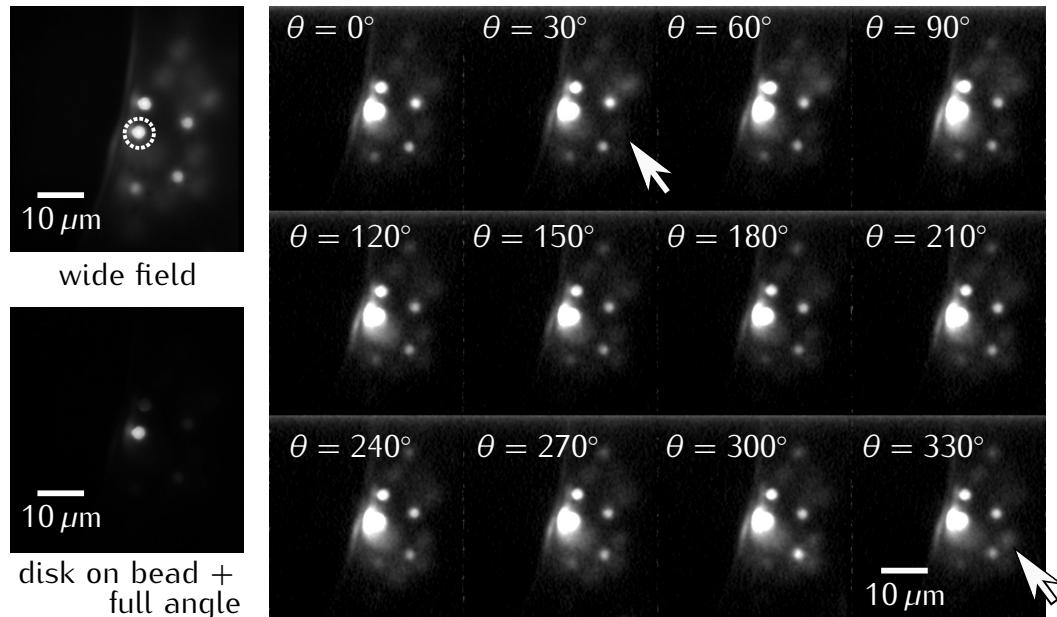


Figure 6.6.: Dense beads in agarose gel **top left:** Wide field image of the beads. The target bead is highlighted with a white circle. **bottom left:** Target bead is selectively illuminated by the focal plane SLM (using all angles). **right mosaic:** Variation of illumination angle. The contrast of out-of-focus beads is increased by scaling the values with a factor of 100 compared to the two images on the left.

The images are shown in Figure 6.6. In the widefield image, I indicate one bead with a white circle. In the other images, this bead is selectively illuminated using the focal plane SLM white circle with dashed outline.

For simplicity, I have omitted the raytrace illumination optimization and just vary a circular window on the pupil plane SLM ( $\rho = 0.7, r = 0.3$ , with the same geometry as in Figure 6.2 (e)).

In the mosaic on the right side of Figure 6.6, the intensity is displayed with a factor of 100× compared to the previous two images. The same scaling is applied to the images of the mosaic. The intensity of the central bead is clipped.

## 6. Experimental results with spatio-angular microscope

The illumination cone that moves with the window manifests itself as a change in the relative intensities of the out-of-focus beads. A difference can be seen, for example, in the point marked by an arrow in the pictures for  $\theta = 30^\circ$  and  $\theta = 330^\circ$ .

### 6.5. Conclusion

The described experiments demonstrate that the hardware of the microscope is functioning as intended, although the performance is impaired by low transmission and long pattern loading times.

Especially for the experiment in section 6.3, a lot of software had to work in conjunction. The mapping between focal plane SLM and camera has to be established, the beads must be located and optimal illumination patterns must be found. These algorithms should work in close combination with the hardware control, so that the entire experiment can run with as little user interaction as possible and finish within reasonable time.

## 7. Discussion

The aim of this thesis has been the development of a widefield fluorescence microscope system that can control the irradiance in the specimen as well as the illumination angles with the aim of decreasing phototoxicity.

origin of the idea

The original idea was to combine a programmable array microscope with control of the illumination directions. Initially, this seemed to be an elegant approach: The programmable array microscope produces two images on a camera, one of which contains only out-of-focus light. By variation of the illumination angle of the excitation light, it should be possible to find the direction with minimal out-of-focus contributions.

Fairly quickly it became clear that this approach, if at all, would work only inefficiently. After all, for the programmable array microscope to work, fine structures must be imaged into the specimen. This, however, has the consequence that several diffraction orders instead of just one bundle of rays must traverse the sample. For most specimens this will bring no advantage compared to a widefield microscope.

We opted instead for a modification of the excitation path in a widefield microscope. My assumption was that given an estimate of the three-dimensional fluorophore distribution, and perhaps additional information about the expected movement of cells, pathogens or organs; a sufficiently accurate prediction of the expected out-of-focus light can be made.

description of the hardware

Using two spatial light modulators (SLM), we can project appropriate distributions of excitation light into the sample. One SLM controls the angle and the other the in-focus pattern of light. Our goal was to acquire one stack, consisting of twenty slices, per minute. For this, partial recordings of slices should be acquired in sequence and later composed into one image (see chapter 3, in particular section 3.2.5). Therefore, we selected the SLM devices with an emphasis on high speed.

The fastest commercially available SLMs are ferroelectric liquid crystal on silicon devices (fLCoS) and digital micro mirror devices (DMD), both of which can only do binary modulation. However, in our case binary intensity modulation

## 7. Discussion

is disadvantageous. Sharp edges lead to high diffraction losses and strong oscillations of the field in the Fraunhofer diffraction pattern.

The pupil plane SLM, that controls the illumination angles should ideally not be a binary device, otherwise oscillations of excitation intensity would occur in the specimen and appear on the camera image. For this reason, we use a specifically developed SLM, whose mode of operation and speed resembles that of a DMD but can display gray scale values. A mirror array of size  $256 \times 256$  pixels is sufficient for angular control. This facilitated the development of the mirror and fast control electronics at Fraunhofer IPMS. The controller can store 1023 image frames locally. For many applications of angular illumination control it is sufficient to select from this set of patterns a suitable candidate.

The focal plane SLM should have a high resolution and it should be possible to update its patterns very fast, so that the illumination can be adapted to the specimen during acquisition with low latency. Initially, I opted for a SLM that is connected to the graphics card of a computer. We chose a ferroelectric LCoS SLM because its pixel borders are less sharp than those of the DMD and we expected a better efficiency for our application. Unfortunately, there were difficulties with the synchronization between the graphics card and the other devices. Therefore, relatively late into the project, I had to replace the SLM controller with another one that contains internal memory and is linked to a computer via USB. Unfortunately, the USB connection is very slow and fast update of image patterns is no longer possible.

The ForthDD USB controller of the focal plane SLM can store 200 images and replacing them takes several minutes. This makes it very difficult to perform a technique similar to controlled light exposure microscopy with the current setup because the set of 200 images are not enough to allow for the fine-grained spatial control one would need to implement CLEM.

In retrospect, it would have been easier to use two of the custom-made grey value SLMs from Fraunhofer. Note that Institut Pasteur and Fraunhofer IPMS continue this work and do just that under the Joint-Programme Inter Carnot Fraunhofer PICF 2011, "Micromirror Enhanced Microscopic Imaging for high-speed angular and spatial light control in spectral Optogenetics and Photomanipulation applications in biological applications" (MEMI-OP).

A serious disadvantage of the Fraunhofer SLM in combination with the Fourier optical filter approach employed in our prototype is the small acceptance angle. This limits the exposed field to  $80 \mu\text{m}$  diameter for a wavelength of  $473 \text{ nm}$  using a  $63\times$  objective with a numerical aperture of 1.4, while the objective does support

Why Fraunhofer micro  
mirror array?

choice for focal  
plane SLM

remedy against low  
acceptance angle

## 7. Discussion

400  $\mu\text{m}$  field diameter. One solution could be contrast generation in a common path interferometer as described in the patent application (Heintzmann and Wicker 2010). The approach is derived from reflective Nomarski differential interference contrast microscopy. A birefringent prism separates the illumination bundle into bundles that have a small offset (shear). If the shear distance corresponds to the pixel pitch  $\Lambda = 16 \mu\text{m}$  of the micro mirrors then this device converts height differences between adjacent mirrors into intensity contrast. My experiments with a set of Nomarski prisms that were available in our lab showed that this method can work. However, the prisms had too small a shear angle and returning diffraction orders were cut off. Meanwhile planning for the original, and with respect to acceptance angle slightly flawed, prototype had advanced so far that the change of the contrast method no longer seemed possible and the project consortium decided to abandon the development of this alternative contrast method. However, the common path interferometer is still a very promising method and has the potential for good contrast at large acceptance angles when prisms with larger shear angles are used. Additionally, it should be noted that this interferometric method will work better when using piston-type micro mirrors as compared to torsion micro mirrors.

priority of the control algorithm

Given the *low light efficiency* of our prototype (0.004%, 17  $\mu\text{W}$  using a 400 mW laser, see section 6.2 on page 102), which could be just barely enough to investigate the biological test system of *C. elegans* embryos, the disproportionately high effort that went into synchronizing the two fast SLMs which can only run at a *reduced duty cycle*, and the *limited etendue* which excludes some interesting experiments, it would have been better in hindsight, to build a demonstrator with two slow, conventional, grey-value SLMs and to spend more effort on the development of the illumination control algorithm and biological experiments.

holographic system

In this context, with the aim of simplifying the hardware, I built a holographic illumination system consisting of a single phase-only SLM in the intermediate image plane. This enables the simultaneous control of both the in-focus light distribution as well as the illumination angles in the specimen. The SLM displays diffraction gratings and its arrangement is such, that the first diffraction order illuminates the pupil. The illumination angle in the specimen can be adjusted by the grating period and direction while the local irradiance is controlled with the grating contrast.

Unfortunately, the phase-only SLM (Holoeye Plato, Berlin, Germany) that I used for the experiments suffers from cross-talk between pixels, a non-linear transfer function and temporal fluctuations of the displayed phase pattern. It

## 7. Discussion

was uncertain whether these problems could be circumvented. Especially higher orders which are generated by the device's non-linearity are a problem when they reach the sample. This makes it particularly difficult to project a grating with small period into the sample because this requires the superposition of two phase gratings on the SLM.

Projecting grating patterns is necessary, because for my illumination algorithm I need a reasonably good measurement of the three-dimensional fluorophore distribution. For many specimen structured illumination is necessary to remove out-of-focus light from the raw images and obtain optical sections. Another phase SLM (X10468 series, Hamamatsu) became available more recently has a much better performance and could presumably be used to construct a holographic spatio-angular illumination device.

The main prototype of our project with two SLM, as described in chapter 4, is more suitable for structured illumination. The period on the focal plane SLM and the illumination aperture defined by the pupil plane SLM can be selected for best possible contrast of the in-focus light pattern. Optically sectioned images can then be calculated with various methods. The HiLo method proposed by Jerome Mertz and best documented in Mertz and Kim (2010) is preferable to others as only two exposures per slice are necessary. Since images in our system are taken in rapid succession and movement artifacts are unlikely, we developed a variant of the HiLo method. In contrast to the original, which uses one uniformly illuminated image and one with structured illumination, we use two structured illumination images with a relative shift of  $\pi$  leading to an improved signal-to-noise ratio.

During my work on the project a much improved camera technology (sCMOS) came to market. No such camera was used for measurements in this work. It could, however, be added to our system without substantial changes.

I use an Arduino microcontroller for electronic synchronization. This cheap and easy to use electronics platform has been used for several years in our lab and is particularly useful for synchronization of multiple devices. The source code for the Arduino microcontroller is often short and relatively easy to read. This controller is thus well suited to document the logic in our synchronization circuits and can be easily understood and extended by new members of our group.

During this work, I used many different electronic devices (SLM: Hamamatsu, Holoeye, ForthDD, Texas Instruments, Fraunhofer, cameras: Andor (Clara, IXon2, IXon3, IXon Ultra, Neo sCMOS), Photometrics Cascade II, Hamamatsu (Orca Flash 2.8 and 4.0), Logitech Pro 9000, and more). I noticed that construction and debugging effort depend very much on the quality of the documentation. If the

sectioning by structured illumination

sCMOS -- new camera technology

Arduino for control electronics

## 7. Discussion

documentation is insufficient, which unfortunately is often the case, then it helps if communication is done with open standards (USB video device class, Ethernet).

Particularly positively I was surprised by the Texas Instruments DMD. The SLM development kit (DLP LightCrafter, YoungOptics) is very mature (Instruments 2012), contains open source software and high quality documentation explaining even the control registers of individual chips.

Unlike the Fraunhofer micro mirror array (as described in section 4.1.2), the Texas Instruments digital micro mirrors tilt around their diagonals. For the 0.3 WVGA DMD, that is used in my development kit, the pixels are addressed as a grid that is rotated by 45° but can be illuminated parallel to one of the edges of the device. This simplifies building the setup at the expense of a slightly more complicated software control. The larger DMD devices can be addressed more easily but must be illuminated in an angle of 45° relative to the device.

While working with the kit I was able to implement features within three days, for which I spent several months of reverse engineering and trial and error on devices of other manufacturers — most notably, controlling individual frames at the fastest possible update rate (1440 frames per second) using digital video output (HDMI) from a consumer grade graphics card. If I had known this before, I would have designed the prototype differently and I would have accepted some drawback regarding optical performance.

I am not content with the current state of scientific cameras because all of them gave me problems with incompatible or unstable drivers. Therefore, I hope that there will be more projects that open their resources to the public, such as Marc Levoy's Franken Camera (Adams et al. 2010) which is based on an open sensor frontend by Andrey Filippov (<http://elphel.com>); or that the manufacturers of the ever-improving consumer cameras document and disclose the protocols for disabling automatic image processing and accessing raw sensor data for their devices (as with the Logitech Pro 9000).

Both our prototype and the software for illumination optimization have been designed for the observation of cells in a developing *C. elegans* embryo. So far, I was able to demonstrate spatio-angular illumination on static, non-living samples but I have not yet applied the method on living organisms. Here, the main problem is that the image upload, especially to the focal plane SLM, takes disproportionately long.

Open hardware is a good thing

results of existing control software

## 7. Discussion

### 7.1. Outlook

proposition for  
an optogenetics  
experiment

If the sample does not change very fast, and plenty of time is available to upload images into the SLM controllers, then the current prototype allows experiments with rapidly changing illumination patterns (about 1000 fps is attainable). One interesting biological experiment would be similar to Branco et al. (2010). There, synapses were excited by moving a focal spot along one linear dendrite and its response was recorded as a function of the speed of the focal spot. With our system, two branches of a dendrite could be stimulated simultaneously. Thereby, the response of the junction could be investigated.

next steps for  
control software

The algorithm for the optimization of the illumination patterns can still be improved. So far, I assume that the sample can be represented well by spheres. The nuclei in each slice are illuminated individually and the algorithm finds illumination angles so that exposure of out-of-focus nuclei is avoided. An obvious improvement would be to find nuclei that can be illuminated with similar angles and group them for simultaneous exposure. Even better would be an algorithm in which the specimen is not represented as solid bodies but works directly on stacks of optical sections. In a first simple experiment, using the computational power of graphics processing units, I could show that the extensive calculations can be carried out in reasonable time frames.

maximum likelihood  
deconvolution

Further studies would be useful regarding the data analysis. As I already mentioned in 2.3.1, given the mapping between focal plane SLM and camera, computational descanning could be implemented, i.e. a classification of the raw image data into in-focus and out-of-focus photons. However, this would likely require a more accurate understanding of the excitation light distribution in the sample. In this regard, it would be helpful to simulate the wave-optical image formation of the prototype with partial coherence. This would answer the question how important the grey levels of the micro mirror array in the pupil-plane really are, and whether or not we can replace it with a binary DMD.

This simulation could also be used to investigate the question in section 2.3.2 regarding how a phase SLM would work in a light field microscope. A similar simulation should be used to investigate the influence of field mask B0 and Fourier stop B1 on the contrast and the transfer function of the schlierenoptics system.

## A. EM-CCD camera calibration

### A.1. Andor Basic code listing for automatic image acquisition

The following code will record calibration data for an Andor EM-CCD with as little user interaction as possible. More detail is given in the main text in section 1.4 on page 30.

The program is written in a dialect of Basic and automates the Andor Solis software. Before use, a picture resembling Figure 1.8 on page 33 should be imaged onto the sensor, e.g. a defocused fluorescent sample. The acquired data can later be processed using either the Matlab/DIPimage function `cal_readnoise` or, equivalently, by using the Python script from the next section.

A camera calibration allows conversion of image data into the device independent unit of effective photoelectrons but this only works as long as data acquisition occurs at the same camera settings (pre-amp gain, EM-gain, sensor temperature, vertical shift speed, readout rate, ...) as those that were used for the calibration. This Basic program measures data for a wide range of EM-CCD amplification settings, but it could easily be adopted to analyze other parameters as well.

The camera that I have used in the development of this program comprises an internal mechanical shutter. This is useful because it is important that for each parameter setting at least one dark image is acquired (but it is better to acquire two dark images and use the second). Ultimately, dark images are necessary to quantify the readout noise.

The code listings in this section are supposed to be in this sequence in a single source file.

For this program I assume that the camera is illuminated with a continuous flux of photons. The program is designed to acquire images with a wide range of EM gains. Since the photon flux remains constant but amplification varies greatly, I acquire one image with a short  $10\ \mu s$  exposure prior to each measurement. The following function searches for the maximum value in this image and calculates an appropriate exposure time so that a maximum of 10000 ADU will be obtained

## A. EM-CCD camera calibration

in the preceeding acquisitions.

### Andor Basic

```
function ~GetSaturatingExposure()
    SetKineticNumber(1)
    exp=.01
    SetExposureTime(exp)
    run()
    m=maximum(#0,1,512)
    GetSaturatingExposure=exp*10000/(m-100) % 100 is the background in ADU
    CloseWindow(#0)
return
```

The following code listing selects the conventional readout register of the sensor (a register without EM multiplication), acquires 20 images without and then with light by calling the function `run()` and stores the data in a TIF image file.

### Andor Basic

```
name$ = "C:\Users\work\Desktop\martin\20111111\scan-em3\xion_"
print("start")

SetOutputAmp(1)
print("conv_start")
exp= ~GetSaturatingExposure()
print(exp)
SetExposureTime(exp)
SetKineticNumber(20)
SetShutter(0,1)
run()
save(#0,name$ + "conv1_dark.sif")
ExportTiff(#0, name$ + "conv1_dark.tif", 1, 1, 0, 0)
CloseWindow(#0)
CloseWindow(#1)

SetShutter(1,1)
run()
save(#0,name$ + "conv1_bright.sif")
ExportTiff(#0, name$ + "conv1_bright.tif", 1, 1, 0, 0)
CloseWindow(#0)
CloseWindow(#1)
```

The loop in the next listing makes similar acquisitions for a range of EM gains. Evaluating the data revealed that a settling time of a few seconds should be allowed for after calling `SetGain`. After all, there are relatively high voltages. I inserted a comment in the corresponding line.

### Andor Basic

```
SetOutputAmp(0)
SetShutter(1,1)
for i = 40 to 300 step 10
    SetGain(i)
    % here should be a 3s wait
```

## A. EM-CCD camera calibration

```

exp=~GetSaturatingExposure()
print(exp)
SetExposureTime(exp)
SetKineticNumber(20)
SetShutter(0,1)
run()
save(#0,name$ + str$(i) + "_dark.sif")
ExportTiff(#0, name$ + str$(i) + "_dark.tif", 1, 1, 0, 0)
CloseWindow(#0)
CloseWindow(#1)
SetShutter(1,1)
run()
save(#0,name$ + str$(i) + "_bright.sif")
ExportTiff(#0, name$ + str$(i) + "_bright.tif", 1, 1, 0, 0)
CloseWindow(#0)
CloseWindow(#1)
next

```

Finally I acquire a last measurement with the conventional readout register:

### Andor Basic

```

SetOutputAmp(1)
print("conv_end")
exp= ~GetSaturatingExposure()
print(exp)
SetExposureTime(exp)
SetKineticNumber(20)
SetShutter(0,1)
run()
save(#0,name$ + "conv2_dark.sif")
ExportTiff(#0, name$ + "conv2_dark.tif", 1, 1, 0, 0)
CloseWindow(#0)
CloseWindow(#1)

SetShutter(1,1)
run()
save(#0,name$ + "conv2_bright.sif")
ExportTiff(#0, name$ + "conv2_bright.tif", 1, 1, 0, 0)
CloseWindow(#0)
CloseWindow(#1)

```

Table A.1 summarizes results of calibration measurements that were acquired using this software and evaluated using the Python code from the next section.

Unfortunately, the data in the first and last line (conv1 and conv2 with  $M = 1$ ) show a disparity in the pre-amplifier gain  $M_{\text{pre}}$ . An improvement would be to use an LED light source (which doesn't bleach) or intersperse conventional readouts between measurements with EM gain in order to compensate for variations due to bleaching.

### A. EM-CCD camera calibration

gain <sub>software</sub>	$1/(M \cdot M_{\text{pre}})$ [e <sup>-</sup> /ADU]	$N_r$ [e <sup>-</sup> /px]	$N_{(M)}/(W \times H)$ [e <sup>-</sup> /px]	exposure [ADU]	$N'_{(M)}/(W \times H)$ [s]	$1/F_n$ [e <sup>-</sup> /(px s)]
conv1	1.3165	7.189	3008.66	0.2016	14923	0.981
50	0.1160	0.486	260.05	0.0289	8995	0.591
60	0.0984	0.406	225.46	0.0249	9054	0.595
70	0.0841	0.349	190.52	0.0212	8983	0.591
80	0.0729	0.305	165.24	0.0186	8907	0.586
90	0.0680	0.288	150.54	0.0161	9368	0.616
100	0.0611	0.262	128.47	0.0136	9427	0.620
110	0.0550	0.241	121.11	0.0129	9409	0.619
120	0.0510	0.228	113.71	0.0120	9498	0.624
130	0.0465	0.211	106.66	0.0112	9541	0.627
140	0.0433	0.201	96.95	0.0101	9564	0.629
150	0.0405	0.192	89.68	0.0093	9671	0.636
160	0.0380	0.183	87.24	0.0090	9656	0.635
170	0.0359	0.175	81.56	0.0084	9739	0.640
180	0.0339	0.169	79.80	0.0081	9863	0.648
190	0.0321	0.163	74.00	0.0075	9806	0.645
200	0.0305	0.158	72.57	0.0073	9878	0.649
210	0.0292	0.155	69.44	0.0070	9944	0.654
220	0.0280	0.150	67.69	0.0068	9971	0.656
230	0.0268	0.147	65.63	0.0065	10057	0.661
240	0.0257	0.188	63.90	0.0063	10131	0.666
250	0.0244	0.140	62.52	0.0062	10026	0.659
260	0.0237	0.137	62.86	0.0062	10078	0.663
270	0.0229	0.135	63.17	0.0062	10130	0.666
280	0.0221	0.133	63.64	0.0062	10204	0.671
290	0.0214	0.130	63.38	0.0062	10162	0.668
300	0.0205	0.128	63.20	0.0062	10133	0.666
conv2	1.5953	8.768	8198.86	0.5291	15496	1.019

Table A.1.: Comparison of read noise for different EM-gain settings (first column) of the Andor IXon3.  $W$  and  $H$  are the size of the sensor (in pixels). The value  $N'_{(M)}$  estimates the number of photoelectrons the detector would have seen with 1 s integration time and is used to calculate the excess noise factor in the last column. In EM-mode the fastest readout speed was used (10 MHz) with the default vertical shift speed of 1.7  $\mu$ s.

## A. EM-CCD camera calibration

### A.2. Python code listing for the read noise evaluation

Here I present a Python implementation for evaluating data that has been recorded using the program from the previous section. Figure A.1 shows two evaluations for data with and without EM-gain using an Andor iXon3 EM-CCD camera.

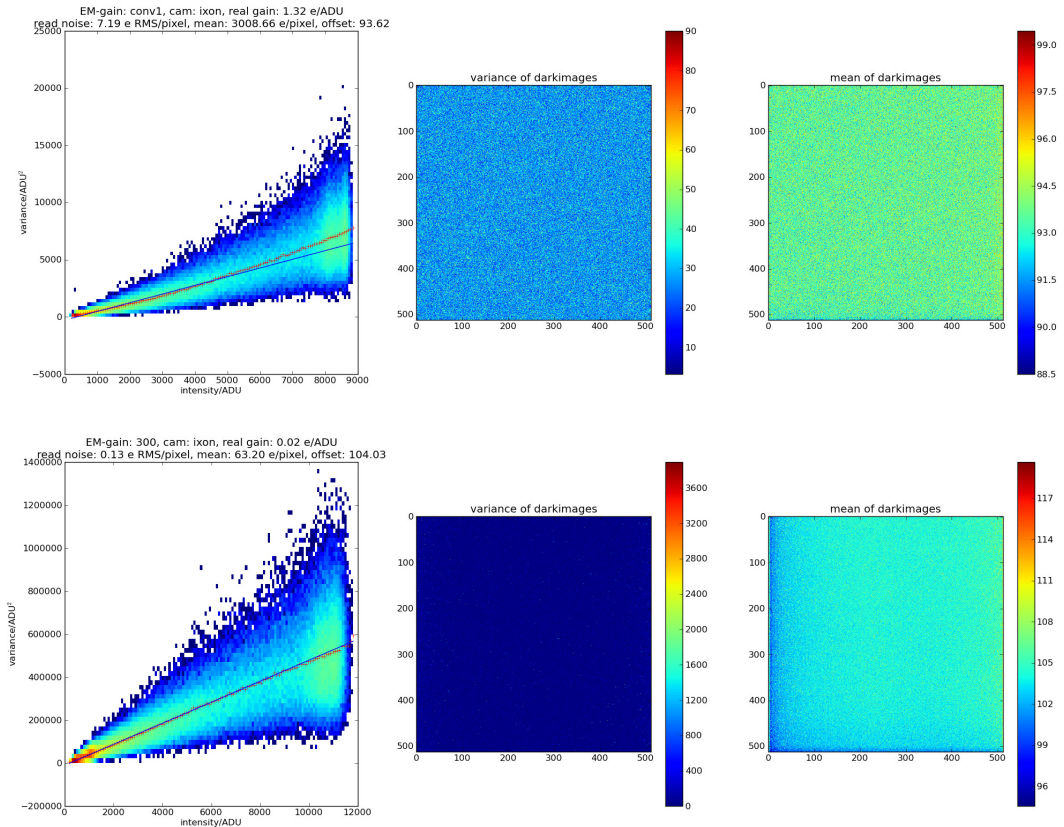


Figure A.1.: Readout noise evaluation using the Python code **top**: Conventional readout of an Andor iXon3 camera. **bottom**: readout with an EM-gain setting of 300 on the same camera with identical sample. **left**: 2D histogram of per pixel variances against binned intensities. red data points: measurements, blue line: linear fit **middle**: variance of 20 dark images. **right**: mean of 20 dark images.

The following code loads several Python packages. Essentially, I use `numpy` by loading `pylab` (Jones et al.) for the data analysis tasks and the package `matplotlib` (Hunter 2007) for visualizing the results.

Python

```
#!/usr/bin/env python
# usage: ti.py DIRECTORY CAMERA_NAME EM_GAIN
# example: ti.py /media/backup/andor-ultra-ixon/martin/20111111/scan-em3/ ultra 2700
import sys
```

## A. EM-CCD camera calibration

```
import os
import matplotlib
matplotlib.use('Agg')
from pylab import *
from libtiff import TIFFfile, TIFFimage
from scipy import stats
seterr(divide='ignore')
```

When starting the program I specify which data should be loaded using command line parameters. The following code will read in the measured image data with and without illumination.

### Python

```
folder = sys.argv[1]
cam = sys.argv[2]
gain = sys.argv[3]

def readpics(gain, cam='ixon_', isdark=False):
    print 'loading ', os.path.join(folder, cam) + '_' + gain + '_bright.tif'
    fg=TIFFfile(os.path.join(folder, cam) + '_' + gain + '_bright.tif')
    bright,bright_names=fg.get_samples()
    bg=TIFFfile(os.path.join(folder, cam) + '_' + gain + '_dark.tif')
    dark,dark_names=bg.get_samples()
    return (bright[0],dark[0])

(f,b) = readpics(gain=gain, cam=cam)
```

The next code listing creates a two-dimensional histogram with 64 bins for variances and 128 bins for intensities.

### Python

```
ny,nx=64,128
H,y,x=histogram2d(v.flatten(),i.flatten(),bins=[ny,nx],
                    range=[[0,v.max()], [0,i.max()]])
extent = [x[0], x[-1], y[0], y[-1]]

fig=figure(figsize=(24, 8),dpi=300)
hold(False)
title('bal')
subplot(1,3,1)
imshow(log(H), extent=extent,
       aspect='auto', interpolation='none',origin='lower')
hold(True)
```

The histogram is not strictly necessary for the analysis but gives an overview of the measured data at a quick glance, i.e. if there were enough measurements for all intensities and whether the sensor was over-exposed.

The most important part of the evaluation is performed in the following code segment. Here I accumulate data in the variables acc and accn that is later used to determine the average values of the variances for all intensities.

## A. EM-CCD camera calibration

Python

```
acc=zeros(x.shape,dtype=float64)
accn=zeros(x.shape,dtype=int64)
s=nx/i.max()
for ii,vv in nditer([i,v]):
    p=round(ii*s)
    acc[p]+=vv
    accn[p]+=1
```

Subsequently, I determine the parameters for a linear fit of the variances vs. intensities, utilizing only the first 60% of the intensities so that any non-linearities that might occur at higher intensities do not affect the slope.

Python

```
ax=x[nonzero(accn)]
ay=acc/accn
ay=ay[nonzero(accn)]
l=round(.6*len(ax))
bx=ax[0:l]
by=ay[0:l]
plot(ax,ay,'r+')
slope,intercept,rval,pval,stderr=stats.linregress(bx,by)
```

From the slope of the line I determine the conversion factor to change the ADU units into the device-independent unit of photoelectrons. With this I convert the variance of the dark images into readout noise in terms of photoelectrons per pixel.

Python

```
plot(ax,polyval([slope,intercept],ax))
xlabel('intensity/ADU')
ylabel(r'veariance/ADU$^2$')
real_gain=1/slope # unit electrons/ADU
read_noise=sqrt(var(b))*real_gain # electrons RMS per pixel
mean_elecs=(mean(f)-mean(b))*real_gain # photoelectrons electrons per pixel
print gain,cam,real_gain,read_noise,mean_elecs,mean(b),rval,pval,stderr
tit='EM-gain: %s, cam: %s, real gain: %.2f e/ADU\n'
read noise: %.2f e RMS/pixel, mean: %.2f e/pixel, offset: %.2f'
% (gain,cam,real_gain,read_noise,mean_elecs,mean(b))
title(tit)
subplot(1,3,2)
imshow(var(b,axis=0))
title('variance of darkimages')
colorbar()
subplot(1,3,3)
imshow(mean(b,axis=0))
title('mean of darkimages')
colorbar()
show()
fig.savefig(cam+'_'+gain+'.png')
```

## B. Optical sectioning by structured illumination using the HiLo method

In this chapter I compare three methods to calculate optical sections from fluorescence microscope images with structured illumination. I employ the wave-optical model of image formation (see section 1.3.2) to simulate focal stacks with structured illumination of a three-dimensional fluorophore distribution.

The code in this chapter simulates aberration-free imaging and compares the performance of sectioning algorithms at different light levels, i.e. in the presence of photon shot noise.

First, I will construct a three-dimensional fluorophore distribution. Then I will calculate the three-dimensional point spread function  $h(r)$  of a high-aperture immersion objective with  $NA = 1.4$  and  $n = 1.52$  using equations (1.12) and (1.8) on page 24. Using this three-dimensional array (denoted by `psf(:,:,::)` in the code), the three-dimensional light distribution in the sample, as well as images on the camera can be calculated by a convolution operation<sup>1</sup>.

For the numerical simulation I use the DIPimage Toolbox for Matlab (Diplib.org 2012) as it permits expression of the required image processing algorithms with a relatively elegant and concise syntax.

The following code listing fills a three-dimensional array with the geometric primitives line, rectangle and a sphere shell. The function `newim(GX,GX,GX)` creates a new DIPimage data object. In general, DIPimage functions can receive their arguments either explicitly, as in this case, or implicitly by calling with another DIPimage data object, e.g. when calling `rr(g2)` for constructing the hollow sphere. The function `rr()` returns an array where each element contains the distance to the central pixel. The comparison operation results in a Boolean

---

<sup>1</sup>I use the same point spread function for excitation and detection. More realistic results can be obtained when the point spread functions are scaled according to excitation and emission wavelengths.

## B. Optical sectioning by structured illumination using the HiLo method

data type which I implicitly turn back into a floating point number by adding a zero.

To save computation time when applying the section algorithms, I cut S to the smallest dimensions, so that it still contains the complete object. I implement all convolution operations with Fourier transforms. Therefore the data should be padded with zeros to prevent overlap of the image information at the borders. I used padding for all images that I show here.

The figure next to the code shows the geometry of the three-dimensional fluorophore distribution and three simulated widefield images of the planar objects.

Matlab

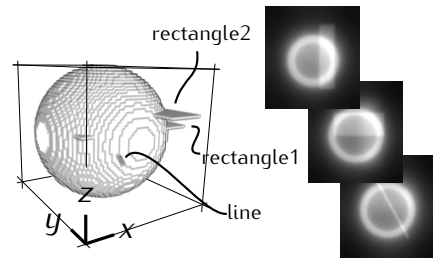
```
global GX; GX = 64; g2 = newim(GX,GX,GX); % make empty 3d image
line_z=floor(size(g2,3)/2)-3;
lineseg = drawline(g2,floor([.3*GX 0 line_z]),floor([.8*GX .9*GX line_z]),1);

rect_x0 = floor(.2*GX); rect_x1 = floor(.9*GX);
rect_y0 = floor(.2*GX); rect_y1 = floor(.5*GX);
rect_z1 = floor(GX/2)+3;
rectangle1 = newim(g2);
rectangle1(rect_x0:rect_x1,rect_y0:rect_y1,rect_z1)=1

rect_x0 = floor(.6*GX); rect_x1 = floor(.8*GX);
rect_y0 = floor(.0*GX); rect_y1 = floor(.9*GX);
rect_z2 = floor(GX/2)+9;
rectangle2 = newim(g2);
rectangle2(rect_x0:rect_x1,rect_y0:rect_y1,rect_z2)=1;

hollow_sphere = 0.0 + (.3<rr(g2,'freq') & rr(g2,'freq')<.4);

S = 12 * lineseg + 4 * (rectangle1 +rectangle2) + hollow_sphere;
[unused1,unused2,S] = bbox(S>0,S); clear g2;
```



With the following code I determine the generalized McCutchen aperture for a lens with a given numerical aperture NA. For this I calculate a spherical shell that touches all sides of the auxiliary array  $a(:,:,,:)$  (Vembu 1961).

The size of the array  $\text{calotte}(:,:,,:)$  is calculated using the numerical aperture, so that it contains only the McCutchen Aperture (the amplitude point spread function  $a(v)$  in section 1.3.2). In order to enable convolutions without aliasing artifacts when using fast Fourier transforms, I choose the size of the array  $\text{otf}(:,:,,:)$  for the optical transfer function twice as big as  $\text{calotte}(:,:,,:)$ . If the object in S is bigger, then I increase the size of  $\text{otf}(:,:,,:)$  to encompass

## B. Optical sectioning by structured illumination using the HiLo method

this also. According to equation (1.16) on page 26 the  $z$ -sampling is

$$\delta z = \frac{\lambda_0}{n(1 - \cos \alpha)} \kappa \quad (\text{B.1})$$

with  $\kappa = 2 * \text{size(calotte}, 3) / \text{size(psf}, 3)$ . Figure a) shows a  $xz$ -cross section through the three-dimensional point spread function, and Figure b) is the cross section through the three-dimensional optical transfer function.

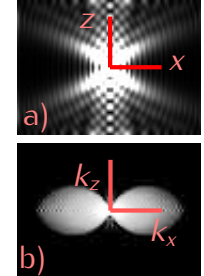
Matlab

```
n = 1.52; % refractive index
NA = 1.4; % numerical aperture of the lens
alpha = asin(NA/n); % acceptance half-angle of lens
X = 37; g = newim(X,X,X); % X should be odd, so that g has a center pixel
a=fft(sinc(rr(g)*pi)); % draw sphere that fills g exactly
zpos = floor(X/2) + round(.5*X*cos(alpha));
xpos1 = floor(X/2) - round(.5*X*sin(alpha));
xpos2 = floor(X/2) + round(.5*X*sin(alpha));
% cut out part of the sphere depending on lenses aperture:
calotte = a(xpos1:xpos2,xpos1:xpos2,zpos:end);
clear g a;

center_ref = @a a(floor(size(a,1)/2),floor(size(a,2)/2),floor(size(a,3)/2));
otf=extract(calotte,max(size(S),size(calotte)*2));
psf = ift(otf);
psf = psf*conj(psf);
otf = real(ft(psf));
otf = otf / center_ref(otf);
psf = psf / center_ref(otf);

psf2d = abs(ft(extract(calotte,size(calotte)*2)))^2;
psf2d = psf2d(:,:,floor(size(psf2d,3)/2));
otf2d = real(ft(psf2d));

otf2dcorr = DampEdge(rr(otf2d,'freq')<.49,.03,2,0);
otf2dcorr = otf2dcorr/otf2d;
otf2dcorr = otf2dcorr / center_ref(otf2dcorr);
% ensure the array the same 2d extent as the 3d otf
otf2dcorr = squeeze(extract(otf2dcorr,[size(psf,1) size(psf,2)]));
```



Images on the camera are obtained according to equation (1.13) on page 25 by a convolution of the three-dimensional fluorophore distribution  $S$  with the point spread function  $\text{psf}(:,:,:$ ). In the case of uniform widefield illumination this is possible using just two three-dimensional Fourier transforms.

Matlab

```
WF = real(ift(ft(extract(S,size(psf))) * otf));
phases = 4; % must be even, so that pi is sampled for HiLo
struc = newim(size(otf,1),size(otf,2),size(S,3),phases);
for slice = 0:size(S,3)-1
    struc(:,:,:,slice,:) = create_structured_slice(S,otf,phases,slice);
end
```

## B. Optical sectioning by structured illumination using the HiLo method

For structured illumination, four three-dimensional Fourier transforms are necessary for each slice and phase of the projected grating. The following function calculates images of one slice for all grating phases. I use `dip_fouriertransform` to exclude the array dimension containing the phase from the transformation. With a  $70 \times 70 \times 51$  sized point spread function, a single call to the following function takes 1.4 s per slice on one Intel i5-2430M core.

Figure a) shows the sinusoidal grating before imaging by the lens. Figure b) shows the simulated in-focus light distribution for incoherent illumination. According to this, the contrast in the image is less than in the original grating. The  $xz$ -cross section in Figure c) shows that the modulation occurs only in a narrow range around the focal plane. The scalebars correspond to a wavelength of  $\lambda_0 = 500$  nm.

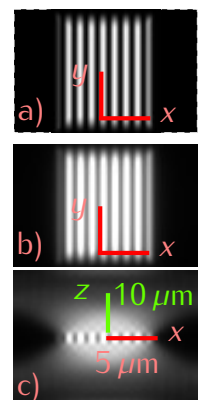
Matlab

```
function Struc = create_structured_slice(S,otf,phases,slice)
% generate 'phases' different sine gratings
% I use DampEdge to ensure a smooth transition to zero at the edges
G=newim([size(S) phases]);
tilt = 2*pi*xx(size(S,1),size(S,2))/64*12;
G(:,:,slice,:) = DampEdge(.5*(1+sin(repmat(tilt,[1 1 1 phases])+ramp([size(tilt),1,
phases],4)*2*pi/phases)),.18,2);

% generate the three-dimensional light distribution in the sample
WF_z = floor(size(otf,3)/2)-floor(size(S,3)/2)+slice;
kG = dip_fouriertransform(extract(G,size(otf)),'forward',[1 1 1 0]);
kG = kG*repmat(otf,[1 1 1 phases]);
Illum = real(dip_fouriertransform(kG,'inverse',[1 1 1 0]));

% multiply fluorophore distribution S with the light distribution
kG = Illum * repmat(extract(S,size(otf)),[1 1 1 phases]);
kG = dip_fouriertransform(kG,'forward',[1 1 1 0]);
kG = kG * repmat(otf,[1 1 1 phases]);
kG = dip_fouriertransform(kG,'inverse',[1 1 1 0]);

% return a 2D slice for each grating phase
Struc = real(kG(:,:,WF_z,:));
```



The following code adds photon noise to the image data, so that the brightest pixel corresponds to a signal of 60000 photons, and reconstructs optical sections with three different algorithms. The code to implement equations (4.19) and (4.20) on page 82 fits into a single line. Reconstructed sections are shown in Figure 4.14 on page 82 and cross sections along z in Figure B.1 in this section.

Matlab

```
section_max_min = @(a) squeeze(max(a,[],4)-min(a,[],4))
section_homodyne = @(a) squeeze(abs(a(:,:,:,:,0)+a(:,:,:,:,1)*exp(i*2*pi*1/4)+a(:,:,:,:,2)*
exp(i*2*pi*2/4)+a(:,:,:,:,3)*exp(i*2*pi*3/4)))
```

## B. Optical sectioning by structured illumination using the HiLo method

```

noise_struc=noise(struc/max(struc)*60000,'poisson'); % reconstruct from noisy images
maxmin=section_max_min(noise_struc);
homodyne=section_homodyne(noise_struc);
hilo=section_hilo(noise_struc,.13,otf2d,otf2dcorr);

```

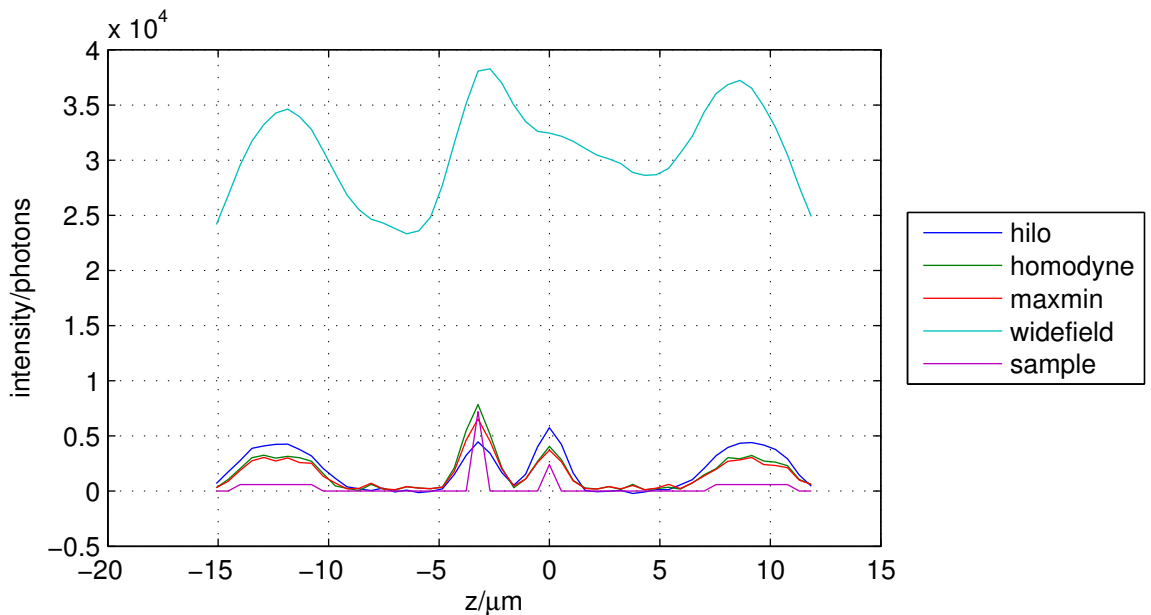


Figure B.1.: Cross sections along  $z$  through the reconstructed focal stack for different sectioning algorithms. The violet line depicts the fluorophore distribution in the sample and the cyan colored line is a section through the widefield stack.

The following function implements the HiLo algorithm as described on page 84. Variables with the digit '3' at the end are two-dimensional array that have been extended to three dimensions by copying.

Matlab

```

function [sec uni nonuni] = section_hilo(struc,filter_fwhm,otf2d,otf2dcorr)
    otf2dcorr3 = repmat(otf2dcorr,[1 1 size(struc,3)]);
    uni = otf2dcorr3*squeeze(dip_fouriertransform(struc,:,:,:,0)+struc,:,:,:,2),'forward'
        ,[1 1 0 0]);
    nonuni_unshifted = otf2dcorr3*squeeze(dip_fouriertransform(struc,:,:,:,0)-struc
       ,:,:,:,2),'forward',[1 1 0 0]);
    tiltbig = 2*pi*xx(size(uni,1),size(uni,2))/GX*12;
    tilt3=repmat(exp(-i*tiltbig),[1 1 size(struc,3)])
    nonuni = dip_fouriertransform(tilt3*dip_fouriertransform(nonuni_unshifted),'inverse'
        ,[1 1 0]),'forward',[1 1 0]);

    filter_sigma = filter_fwhm/sqrt(log(2));
    lowpass = extract(DampEdge(exp(-rr(otf2d)^2/(filter_sigma*size(otf2d,1))^2),.2,2,0),
        [size(uni,1) size(uni,2)]);
    hipass = 1-lowpass;

```

## B. Optical sectioning by structured illumination using the HiLo method

```
ring = rr(otf2d) < filter_fwhm*size(otf2d,1);
ring = extract(bdilation(ring)-ring,[size(uni,1) size(uni,2)]);

ring3 = repmat(ring,[1 1 size(uni,3)]);
lowpass3 = repmat(lowpass,[1 1 size(uni,3)]);
hipass3 = repmat(hipass,[1 1 size(uni,3)]);

ringhi = mean(ring3*abs(hipass3*uni)^2,[],[1 2]);
ringlo = mean(ring3*abs(lowpass3*nonuni)^2,[],[1 2]);
eta = ringhi/ringlo; % one value per slice
eta_median=median(eta);

image_lo = imag(dip_fouriertransform(lowpass3 * nonuni,'inverse',[1 1 0]));
image_hi = real(dip_fouriertransform(hipass3 * uni,'inverse',[1 1 0]));
sec = image_lo+image_hi/eta_median;
```

## C. Mapping between focal plane SLM and camera

### C.1. Rigid coordinate transformation

The equation for the least squares problem in equation 4.18 on 78 can be expressed componentwise:

$$\mathcal{Q} = \sum_i^n |s(\cos \phi r_{ix}^c + q \sin \phi r_{iy}^c) + t_x - r_{ix}^d|^2 + |s(-\sin \phi r_{ix}^c + q \cos \phi r_{iy}^c) + t_y - r_{iy}^d|^2 \quad (\text{C.1})$$

Maxima

The following Maxima code will find the solution to the least squares problem:

Maxima

```
load(minpack)$
q:-1;
g(s,p,tx,ty):=[s*( cos(p)*<cx>+q*sin(p)*<cy>)+tx-<dx>,
                s*(-sin(p)*<cx>+q*cos(p)*<cy>)+ty-<dy>, ... ]$ 
minpack_lsquares(g(s,p,tx,ty), [s,p,tx,ty], [0.88,-3.1,1200,-20]);
```

Where  $g$  is a vector function, which contains two entries for each pair of points of the focal plane SLM and camera coordinates. I computationally construct the lines according to the given pattern, replacing  $\langle cx \rangle$ ,  $\langle cy \rangle$  with measured camera coordinates and  $\langle dx \rangle$ ,  $\langle dy \rangle$  with display coordinates (see the Matlab code in the next section).

The function `minpack_lsquares` calls the subroutine `lmder` which was originally developed for the Fortran package `minpack`.

Fortran

```
c      subroutine lmder (http://www.netlib.org/minpack/lmder.f)
c      the purpose of lmder is to minimize the sum of the squares of
c      m nonlinear functions in n variables by a modification of
c      the levenberg-marquardt algorithm. the user must provide a
c      subroutine which calculates the functions and the jacobian.
c      the subroutine statement is
c          subroutine lmder(fcn,m,n,x,fvec,fjac,ldfjac,ftol,xtol,gtol,
c                           maxfev,diag,mode,factor,nprint,info,nfev,
c                           njev,ipvt,qltf,wa1,wa2,wa3,wa4)
```

## C. Mapping between focal plane SLM and camera

Maxima automatically calculates the symbolic Jacobian and thereby removes an error-prone part of the programmer's work for such optimization problems. This code could easily be modified for more complicated transformations, e.g. including distortion. Because of this flexibility, I decided to use Maxima.

### C.1.1. Application of the rigid transform in OpenGL

The results of the parameter optimization can then be used to adjust the displayed SLM patterns to object positions on earlier camera images. In particular, it is straight forward, to implement the rigid transform using OpenGL's transform primitives (OpenGL is the graphics library, that I usually use).

There are two possibilities of applying the transform: On the one hand, geometrical primitives might be displayed on the focal plane SLM, so that particular areas on the camera are illuminated. On the other hand, a camera image which was acquired earlier can be displayed as texture on the focal plane SLM.

Uploading camera images to the focal plane SLM is too slow in our final system to use the latter method<sup>1</sup>

For this reason, I have mainly used the first method and transform the geometric primitives before I display them on the focal plane SLM.

Here is the corresponding Common Lisp code to initialize the OpenGL modelview matrix with the rigid transform, so that drawn objects will appear at the given positions on the camera.

Common Lisp

```
(defun load-cam-to-lcos-matrix (&optional (x 0s0) (y 0s0))
  (let* ((s 0.82833873909549) (sx s) (sy (- s))
         (phi -3.102) (sp (sin phi)) (cp (cos phi))
         (tx 608.433) (ty 168.918)
         (a (make-array (list 4 4) :element-type 'single-float
                        :initial-contents
                        (list (list (* sx cp) (* sy sp) .0 (+ x tx))
                              (list (* -1 sx sp) (* sy cp) .0 (+ y ty))
                              (list .0 .0 1.0 .0)
                              (list .0 .0 .0 1.0))))))
  (gl:load-transpose-matrix (sb-ext:array-storage-vector a))))
```

C language

Alternatively, here is the equivalent code in C (with different parameters):

C language

```
float m[4*4]; // OpenGL Modelview Matrix
float s=-.8749328910202312,
      sx=s, sy=-s, phi=-.8052030670943575,
```

<sup>1</sup>However, I obtained interesting results with 30 Hz frame rate of the camera and fast feedback to an LCoS controller that was directly connected to a graphics card.

## C. Mapping between focal plane SLM and camera

```

cp=cos(phi),sp=sin(phi),
tx=1456.71806436377,
ty=910.4787738693659;
m[0]= sx*cp; m[4]=sy*sp; m[8] =0; m[12]=tx;
m[1]=-1*sx*sp; m[5]=sy*cp; m[9] =0; m[13]=ty;
m[2]=0; m[6]=0.; m[10]=1; m[14]=0;
m[3]=0; m[7]=0.; m[11]=0; m[15]=1;
glMatrixMode(GL_MODELVIEW);
glLoadMatrixf(m);

```

## C.2. Image processing: Localizing bright spots on the camera

Here I show Matlab/DIPimage code (Diplib.org 2012) to localize individual spots on the camera images, prepare the input for Maxima, read back the fitted parameter values and superimpose the transformed coordinate system of the camera pixels on the the grid of the focal plane SLM in order to estimate the quality of the fit.

The software development kit of the Andor cameras provides functions to store image data along with acquisition parameters in the FITS file format. This can be loaded into Matlab using the function `readim` from the DIPimage toolbox.

### Matlab

```

%% load the files
% 0 .. 99 spot images
% only 10..99 usable because the first are on border and not illuminated
a = newim(1392,1040,103);
for i=0:102
% Andor's FITS format isn't read correctly correct this by adding 2^15
a(:,:,i) = 2^15 + readim(sprintf('0%03d.fits',i));
end

```

Unfortunately, DIPimage's `readim` function seems to have a bug and loads the data as negative values. I manually correct this.

In this particular experiment, the first ten spots on the focal plane were not illuminated. Therefore, these images are excluded from the following processing. Notable is image 102 because it contains an image with uniform illumination. From its histogram I estimated a threshold value of 800 ADU to find a mask that corresponds to the illuminated region.

The uniformly illuminated image is displayed in Figure 4.10 left on page 79. I utilize this image for normalization, so that spots in each image have the same values in each image `corr` regardless of the number of layers of beads in the spots position. I also subtract a background value of 510 ADU, which I have derived from non-illuminated pixels of the images.

### C. Mapping between focal plane SLM and camera

Matlab

```

bg = 510;
bright = squeeze(a(:,:,102));
mask = gaussf(bright,8) > 800; % create mask with illuminated area

posmax = newim(100,2);
for i = 10:99
    corr = (squeeze(a(:,:,i)) - bg) / bright * mask; % correct for sample non-uniformity
    [coords,vals] = findmaxima(gaussf(corr,32)); % find coordinates of maximum
    [valss,valsind] = sort(vals); % sort coordinates by intensity
    tmp = coords(valsind,:); % collect the maximum with highest
    posmax(i,:) = tmp(end,:); % intensity into result
end

```

The DIPimage toolbox provides the function `findmaxima`, that locates all local maxima in an image with subpixel accuracy. I sort the result by grey value and only use the largest. The measured 90 coordinates in `posmax` correspond to  $r_i^c$  in equation 4.18.

The following Matlab code generates and executes code in Maxima to determine the parameters of the transformation, as I explained in the previous section.

The programmatically generated Maxima batch program is stored in the file `fit.max`. After a successful run Maxima returns the transform parameters in the file `max.out`.

Matlab

```

c = double(posmax)';
cmd = ''; % collect equations in maxima format
for i=10:99
    dx = num2str(400+50*mod(i,10));
    dy = num2str(500+50*floor(i./10));
    cx = num2str(c(i+1,1));
    cy = num2str(c(i+1,2));
    cmd=[cmd ' s*( cos(p)*' cx '+q*sin(p)*' cy')+tx-' dx ', ...
          ' s*(-sin(p)*cx '+q*cos(p)*' cy )+ty-' dy ','];
end
cmd(:,end) = []; % delete last comma

% load the fitting package and start defining the merit function g
pre = 'load(minpack)$ q:-1; g(s,p,tx,ty):=[';
% now put cmd between
% call the fitting function and store the parameters into max.out
cod = [']$ fit:minpack_lsquares(g(s,p,x,y),[s,p,x,y],[.88,-1.3,1200,-20]);'...
        'write_data(fit[1],"max.out");'
fid = fopen('fit.max','w'); % write maxima commands into file
fwrite(fid,[pre cmd cod]);
fclose(fid);
[max_status,max_result]=system('maxima -b fit.max'); % execute maxima

```

I load the transformation parameters back into Matlab and create the a diagram (shown in Figure 4.11 in the main text on page 79) to visualize, how well the transform matches camera and display coordinates.

### C. Mapping between focal plane SLM and camera

#### Matlab

```
% load rigid transformation parameters from the file into matlab
params = load('max.out');
scale  = params(1);
phi    = params(2);
tx     = params(3);
ty     = params(4);
mirr   = -1;
R      = [ cos(phi), mirr*sin(phi); ...
           -sin(phi), mirr*cos(phi)];
T      = [tx ty]';

%% plot the two grids on top of each other
mapped = zeros(100,2);
for i=11:100 % camera coordinates into display coordinates
    mapped(i,:) = (scale*R*q(i,:)'+T)';
end

dpos = zeros(100,2);
for i=0:99 % calculate display points
    dpos(i+1,1) = 400+50*mod(i,10);
    dpos(i+1,2) = 500+50*floor(i./10);
end

hold off; plot(dpos(:,1),dpos(:,2),'.'); hold on;
plot(mapped(11:end,1),mapped(11:end,2),'r+'');
```

# Bibliography

- M. D. Abràmoff, I. Hospitals, P. J. Magalhães, and M. Abràmoff. Image Processing with ImageJ. *Biophotonics International*, 2004. 5
- A. Adams, M. Horowitz, S. H. Park, N. Gelfand, J. Baek, W. Matusik, M. Levoy, D. E. Jacobs, J. Dolson, M. Tico, K. Pulli, E.-V. Talvala, B. Ajdin, D. Vaquero, and H. P. a. Lensch. The Frankencamera. *ACM Transactions on Graphics*, 29(4):1, July 2010. ISSN 07300301. doi: 10.1145/1778765.1778766. URL <http://portal.acm.org/citation.cfm?doid=1778765.1778766>. 114
- W. B. Amos, J. G. White, and M. Fordham. Use of confocal imaging in the study of biological structures. *Applied Optics*, 26:3239–3243, 1987. doi: doi:10.1364/AO.26.003239. URL <http://www.opticsinfobase.org/abstract.cfm?URI=ao-26-16-3239>. 28
- N. Aulner, A. Danckaert, E. Rouault-Hardoin, J. Desrivot, O. Helynck, P.-H. Commere, H. Munier-Lehmann, G. F. Späth, S. L. Shorte, G. Milon, and E. Prina. High Content Analysis of Primary Macrophages Hosting Proliferating Leishmania Amastigotes: Application to Anti-leishmanial Drug Discovery. *PLoS neglected tropical diseases*, 7(4):e2154, Apr. 2013. ISSN 1935-2735. doi: 10.1371/journal.pntd.0002154. URL <http://www.ncbi.nlm.nih.gov/article/fcgi?artid=3617141&tool=pmcentrez&rendertype=abstract>. 13
- P. A. Benedetti, V. Evangelista, D. Guidarini, and S. Vestri. Method for Acquisition of Images by Confocal, US Patent 6,016,367, 1997. 81
- T. Bernas, M. Zarebski, R. R. Cook, and J. W. Dobrucki. Minimizing photobleaching during confocal microscopy of fluorescent probes bound to chromatin: role of anoxia and photon flux. *Journal of microscopy*, 215(September):281–296, 2004. 19
- D. Berndt. *Software fuer die zeitoptimierte Kalibrierung von Mikrokippsspiegeln*. PhD thesis, Dresden, 2007. 67

## Bibliography

- D. Berndt, J. Heber, S. Sinning, D. Kunze, J. Knobbe, J.-U. Schmidt, M. Bring, D. Rudloff, M. Friedrichs, J. Roessler, M. Eckert, W. Kluge, H. Neumann, M. Wagner, and H. Lakner. Multispectral characterization of diffractive micromirror arrays. In *Proc. SPIE*, volume 7718, 2010. 67
- D. Berndt, J. Heber, S. Sinning, and D. Rudloff. Calibration of diffractive micromirror arrays for microscopy applications. In *Proc. SPIE*, volume 81910O, 2011. doi: <http://dx.doi.org/10.1117/12.899881>. 67
- Blender.org. Blender, 3D creation software 2.62., 2012. URL <http://www.blender.org/>. 5
- E. E. J. Botcherby, C. W. C. Smith, M. M. Kohl, D. Débarre, M. J. Booth, R. Juškaitis, O. Paulsen, and T. Wilson. Aberration-free three-dimensional multiphoton imaging of neuronal activity at kHz rates. *Proceedings of the National Academy of Sciences*, 109(8):2919–2924, 2012. doi: 10.1073/pnas.1111662109. URL <http://buonmathuot.vn/ws/r/www.pnas.org/content/109/8/2919.full>. 47
- E. J. Botcherby, R. R. Juškaitis, M. J. Booth, and T. Wilson. Abberation-free optical refocusing in high numerical aperture microscopy. *Optics Letters*, 32(14):2007–2009, 2007. 47
- E. S. Boyden, F. Zhang, E. Bamberg, G. Nagel, and K. Deisseroth. Millisecond-timescale, genetically targeted optical control of neural activity. *Nature neuroscience*, 8(9):1263–8, Sept. 2005. ISSN 1097-6256. doi: 10.1038/nn1525. URL <http://www.ncbi.nlm.nih.gov/pubmed/16116447>. 13
- N. Bozinovic, C. Ventalon, T. Ford, and J. Mertz. Fluorescence endomicroscopy with structured illumination. *Opt. Express*, 16(11):4603–4610, 2008. URL [http://nanoscience.bu.edu/papers/Mertz\\_OE\\_2008.pdf](http://nanoscience.bu.edu/papers/Mertz_OE_2008.pdf). 83
- T. Branco, B. A. Clark, and M. Häusser. Dendritic discrimination of temporal input sequences in cortical neurons. *Science (New York, N.Y.)*, 329(5999):1671–5, Sept. 2010. ISSN 1095-9203. doi: 10.1126/science.1189664. URL <http://www.ncbi.nlm.nih.gov/pubmed/20705816>. 115
- W. Caarls, B. Rieger, A. H. B. De Vries, D. J. Arndt-Jovin, and T. M. Jovin. Minimizing light exposure with the programmable array microscope. *Journal of microscopy*, 241(1):101–110, Jan. 2011. ISSN 1365-2818. doi: 10.1111/j.1365-2818.2010.03413.x. URL <http://www.ncbi.nlm.nih.gov/pubmed/21118211>. 48

## Bibliography

- K. K. Chu, D. Lim, and J. Mertz. Enhanced weak-signal sensitivity in two-photon microscopy by adaptive illumination. *Opt. Lett.*, 32(19):2846–2848, Oct. 2007. doi: 10.1364/OL.32.002846. URL <http://ol.osa.org/abstract.cfm?URI=ol-32-19-2846>. 45
- P. Davidovits and M. D. Egger. Scanning laser microscope for biological investigations. *Applied Optics*, 10(7):1615–1619, 1971. 28
- W. Denk, J. H. Strickler, and W. W. Webb. Two-photon laser scanning fluorescence microscopy. *Science*, 245, 1990. 44
- L. Deschenes and D. V. Bout. Single molecule photobleaching: increasing photon yield and survival time through suppression of two-step photolysis. *Chemical physics letters*, 365:387–395, 2002. URL <http://www.sciencedirect.com/science/article/pii/S0009261402014902>. 19
- Diplib.org. DIPimage, a MATLAB toolbox for scientific image processing and analysis 2.4.1., 2012. URL <http://www.diplib.org/>. 5, 78, 123, 131
- R. Dixit and R. Cyr. Cell damage and reactive oxygen species production induced by fluorescence microscopy: effect on mitosis and guidelines for non-invasive fluorescence microscopy. *The Plant Journal*, 36(2):280–290, Oct. 2003. ISSN 09607412. doi: 10.1046/j.1365-313X.2003.01868.x. URL <http://doi.wiley.com/10.1046/j.1365-313X.2003.01868.x>. 17
- C. Dunsby. Optically sectioned imaging by oblique plane microscopy. *Optics Express*, 16, 2008. 42
- R. M. Durbin. *Studies on the development and organisation of the nervous system of caenorhabditis elegans*. PhD thesis, Cambridge, 1987. 14
- A. Edelstein, N. Amodaj, K. Hoover, R. Vale, and N. Stuurman. Computer Control of Microscopes Using  $\mu$ Manager. In *Current Protocols in Molecular Biology*, number October, pages 14.20.1–14.20.17. John Wiley & Sons, Inc., 2010. ISBN 9780471142720. doi: 10.1002/0471142727.mb1420s92. 5
- C. M. Gallo, E. Munro, D. Rasoloson, C. Merritt, and G. Seydoux. Processing bodies and germ granules are distinct RNA granules that interact in *C. elegans* embryos. *Developmental Biology*, 323(1):76–87, 2008. ISSN 0012-1606. doi: 10.1016/j.ydbio.2008.07.008. URL <http://dx.doi.org/10.1016/j.ydbio.2008.07.008>. 14

## Bibliography

- A. E. Gamal and H. Eltoukhy. CMOS image sensors. *Circuits and Devices Magazine, IEEE*, (June), 2005. URL [http://ieeexplore.ieee.org/xpls/abs\\_all.jsp?arnumber=1438751](http://ieeexplore.ieee.org/xpls/abs_all.jsp?arnumber=1438751). 36
- Gimp.org. GNU Image Manipulation Program, 2.7., 2011. URL <http://www.gimp.org/>. 5
- J. W. Goodman. *Introduction to Fourier optics*, volume 2. McGraw-Hill, New York, 1968. 25
- M. Göppert-Mayer. Über Elementarakte mit zwei Quantensprüngen. *Annalen der Physik*, 401(3):273–294, 1931. 44
- H. Gross, W. Singer, M. Totzeck, F. Blechinger, and B. Achtner. *Handbook of optical systems*. Wiley-VCH, physical i edition, 2005. ISBN 9783527606689. URL <http://onlinelibrary.wiley.com/doi/10.1002/3527606688.fmatter/summary>. 21
- N. Grossman, V. Poher, M. S. Grubb, G. T. Kennedy, K. Nikolic, B. McGovern, R. B. Palmini, Z. Gong, E. M. Drakakis, M. A. A. Neil, M. D. Dawson, J. Burrone, and P. Degenaar. Multi-site optical excitation using ChR2 and micro-LED array. *Journal of Neural Engineering*, 7(1):16004, 2010. URL <http://stacks.iop.org/1741-2552/7/i=1/a=016004>. 49
- M. G. L. Gustafsson, D. A. Agard, and J. W. Sedat. Sevenfold improvement of axial resolution in 3D wide-field microscopy using two objective lenses. *Proceedings of SPIE*, 2412:147–156, 1995. URL <http://scholar.google.com/scholar?hl=en&btnG=Search&q=intitle:Sevenfold+improvement+of+axial+resolution+in+3D+widefield+microscopy+using+two+objective+lenses#0>. 26, 27
- M. G. L. Gustafsson, D. A. Agard, and J. W. Sedat. I5M: 3D widefield light microscopy with better than 100 nm axial resolution. *Journal of Microscopy*, 195(July):10–16, 1999. 27
- H. Haferkorn and W. Richter. *Synthese optischer Systeme*. Dt. Verl. der Wiss., Berlin, 1984. 21
- H. Haken and H. C. Wolf. *Molekülphysik und Quantenchemie*. Springer, fifth edition, 2006. doi: 10.1007/3-540-30315-4. 18, 19
- Hamamatsu. Scientific images are more than just pictures. A camera should be more than just a sensor. Technical report, Hamamatsu, 2012a. 34, 36

## Bibliography

- Hamamatsu. Digital Camera C11440-22CU Instruction manual. Technical Report September, 2012b. 36
- R. Heintzmann and K. Wicker. Optical devices and Methods, Patent application WO 2010/089548 A1, 2010. 112
- R. Heintzmann, Q. S. Hanley, D. Arndt-Jovin, and T. M. Jovin. A dual path programmable array microscope (PAM): simultaneous acquisition of conjugate and non-conjugate images. *Journal of microscopy*, 204(Pt 2):119–35, Nov. 2001. ISSN 0022-2720. URL <http://www.ncbi.nlm.nih.gov/pubmed/11737545>. 47
- R. A. Hoebe, C. H. Van Oven, T. W. J. Gadella Jr., P. B. Dholukshe, C. J. F. Van Noorden, and E. M. M. Manders. Controlled light-exposure microscopy reduces photobleaching and phototoxicity in fluorescence live-cell imaging. *Nature Biotechnology*, 25(2):249–253, Feb. 2007. ISSN 1087-0156. doi: 10.1038/nbt1278. 45
- I. Hope. *C. elegans: a practical approach*. Oxford University Press, Oxford, 1999. URL [http://books.google.com/books?hl=en&lr=&id=B5JJaHa3JlgC&oi=fnd&pg=PR17&dq=C.+elegans:+A+Practical+Approach&ots=\\_FyXstupGY&sig=QIIY3tSNFRugKG002T91Fp6ZsOY](http://books.google.com/books?hl=en&lr=&id=B5JJaHa3JlgC&oi=fnd&pg=PR17&dq=C.+elegans:+A+Practical+Approach&ots=_FyXstupGY&sig=QIIY3tSNFRugKG002T91Fp6ZsOY). 58
- J. Huisken, J. Swoger, F. Del Bene, J. Wittbrodt, and E. H. K. Stelzer. Optical Sectioning Deep Inside Live Embryos by Selective Plane Illumination Microscopy. *Science*, 305(5686):1007–1009, Aug. 2004. ISSN 0036-8075. doi: 10.1126/science.1100035. URL <http://www.lmg.embl.de/pdf/huisken04.pdf>. 40, 41, 54
- J. D. Hunter. Matplotlib: A 2D graphics environment. *Computing In Science & Engineering*, 9(3):90–95, 2007. 120
- S.-u. Hwang and Y.-g. Lee. Simulation of an oil immersion objective lens : A simplified ray-optics model considering Abbe's sine condition. *Optics Express*, 16(26):363–370, 2008. 90, 91, 92
- Inkscape.org. Inkscape, a vector graphics editor 0.48.2., 2012. URL <http://inkscape.org/>. 5
- T. Instruments. LightCrafter DM365 Command Interface Guide. Technical Report January, 2012. 114

## Bibliography

- E. Ipp, J. Wenisch, and A. Jacobsen. Deliverable 8.04 Initial MMA/Optics evaluation system (refractive) v1.2. Technical report, In-Vision, 2009. 65
- E. Jones, T. Oliphant, P. Peterson, and Others. SciPy: Open source scientific tools for Python. URL <http://www.scipy.org/>. 120
- C. A. Konopka and S. Y. Bednarek. Variable-angle epifluorescence microscopy: a new way to look at protein dynamics in the plant cell cortex. *The Plant Journal*, 53:186–196, 2008. URL <http://www.biochem.wisc.edu/faculty/bednarek/lab/publications/Konopka2007PlantJ.pdf>. 42
- R. Koshel. *Illumination Engineering: Design with Nonimaging Optics*. Wiley, 2012. ISBN 9781118462492. URL [http://books.google.com/books?hl=en&lr=&id=WpL2SQoJCXYC&oi=fnd&pg=PR2&dq=Illumination+Engineering:+Design+with+Nonimaging+Optics&ots=7gJQ4QgdFp&sig=sTUpKAHR-GEA\\_d5BpVuGoZgNdAc](http://books.google.com/books?hl=en&lr=&id=WpL2SQoJCXYC&oi=fnd&pg=PR2&dq=Illumination+Engineering:+Design+with+Nonimaging+Optics&ots=7gJQ4QgdFp&sig=sTUpKAHR-GEA_d5BpVuGoZgNdAc). 66
- M. Levoy, R. Ng, A. Adams, M. Footer, and M. Horowitz. Light field microscopy. *ACM Trans. Graph.*, 25(3):924–934, July 2006. ISSN 0730-0301. doi: <http://doi.acm.org/10.1145/1141911.1141976>. URL <http://doi.acm.org/10.1145/1141911.1141976>. 49, 50, 54
- M. Levoy, Z. Zhang, and I. McDowall. Recording and controlling the 4D light field in a microscope using microlens arrays. *Journal of Microscopy*, 235(2):144–162, 2009. ISSN 1365-2818. doi: [10.1111/j.1365-2818.2009.03195.x](https://doi.org/10.1111/j.1365-2818.2009.03195.x). URL <http://dx.doi.org/10.1111/j.1365-2818.2009.03195.x>. 49
- K. A. Lidke, B. Rieger, D. S. Lidke, and T. M. Jovin. The Role of Photon Statistics in Fluorescence Anisotropy Imaging. *IEEE Transactions on Image Processing*, 14(9):1237–1245, 2005. 33
- D. Lim, T. Ford, K. Chu, and J. Mertz. Optically sectioned in vivo imaging with speckle illumination HiLo microscopy. *Journal of ...*, 16(January):1–8, 2011. doi: [10.1117/1.3528656](https://doi.org/10.1117/1.3528656). URL <http://biomedicaloptics.spiedigitallibrary.org/article.aspx?articleid=1166622>. 83
- G. Lippmann. Epreuves reversibles. Photographies intégrals. *Comptes-Rendus Académie des Sciences*, 146:446–451, 1908. URL <http://ci.nii.ac.jp/naid/10019520779/en/>. 49

## Bibliography

- C. Lutz, T. S. Otis, V. DeSars, S. Charpak, D. A. DiGregorio, and V. Emiliani. Holographic photolysis of caged neurotransmitters. *Nat. Methods*, 5:821–827, Sept. 2008. URL <http://www.ncbi.nlm.nih.gov/pmc/articles/PMC2711023/>. 51
- C. D. Mackay, R. N. Tubbs, R. Bell, D. Burt, and I. Moody. Sub-Electron Read Noise at MHz Pixel Rates. *SPIE*, 2001. 33
- A. Martínez-García, I. Moreno, M. M. Sánchez-López, and P. García-Martínez. Operational modes of a ferroelectric LCoS modulator for displaying binary polarization, amplitude, and phase diffraction gratings. *Applied optics*, 48(15):2903–14, May 2009. ISSN 1539-4522. URL <http://www.ncbi.nlm.nih.gov/pubmed/19458742>. 74
- M. Matthaе, L. Schreiber, and W. Faulstich, Andreas Kleinschmidt. High Aperture Objective Lens, Patent US 6,504,653 B2, 2003. 4
- Maxima.sourceforge.net. Maxima, a Computer Algebra System. Version 5.28.0., 2012. URL <http://maxima.sourceforge.net/>. 5, 78
- S. C. McClain, L. W. Hillman, and R. A. Chipman. Polarization ray tracing in anisotropic optically active media. I. Algorithms. *J. Opt. Soc. Am. A*, 10, 1993. 87
- C. McCutchen. Generalized aperture and the three-dimensional diffraction image. *JOSA*, 54(2):240–244, 1964. ISSN 1084-7529. doi: 10.1364/JOSA.54.000240. URL <http://www.opticsinfobase.org/abstract.cfm?URI=JOSAA-19-8-1721><http://www.opticsinfobase.org/abstract.cfm?id=52274>. 24
- J. Mertz and J. Kim. Scanning light-sheet microscopy in the whole mouse brain with HiLo background rejection. *Journal of biomedical optics*, 15(1):016027, 2010. ISSN 1560-2281. doi: 10.1117/1.3324890. URL <http://www.ncbi.nlm.nih.gov/articlerender.fcgi?artid=2917465&tool=pmcentrez&rendertype=abstract>. 81, 83, 113
- M. Minsky. Microscopy Apparatus 3,013,461, Dec. 1961. URL [http://www.google.co.uk/patents/download/3013467\\_MICROSCOPY\\_APPARATUS.pdf?id=G01yAAAAEBAJ&output=pdf&sig=ACfU3U0d8iodFNpESGFd41qzyoJL3sDHxQ](http://www.google.co.uk/patents/download/3013467_MICROSCOPY_APPARATUS.pdf?id=G01yAAAAEBAJ&output=pdf&sig=ACfU3U0d8iodFNpESGFd41qzyoJL3sDHxQ). 28
- J. I. Murray, Z. Bao, T. J. Boyle, and R. H. Waterston. The lineage of fluorescently-labeled *Caenorhabditis elegans* embryos with StarryNite and AceTree. *Nature protocols*, 1(3):1468–76, Jan. 2006. ISSN 1750-2799. doi: 10.1038/nprot.2006.222. URL <http://www.ncbi.nlm.nih.gov/pubmed/17406437>. 58

## Bibliography

- M. A. A. Neil, R. Juškaitis, and T. Wilson. Method of obtaining optical sectioning by using structured light in a conventional microscope. *Optics Letters*, 22:1905–1907, 1997. 27, 28, 82
- V. Nikolenko, B. O. Watson, R. Araya, A. Woodruff, D. S. Peterka, and R. Yuste. SLM Microscopy: Scanless Two-Photon Imaging and Photostimulation with Spatial Light Modulators. *Front Neural Circuits*, 2:5, 2008. URL <http://www.ncbi.nlm.nih.gov/pmc/articles/PMC2614319/>. 52
- D. Oron, E. Tal, and Y. Silberberg. Scanningless depth-resolved microscopy. *Opt Express*, 13:1468–1476, Mar. 2005. URL <http://www.weizmann.ac.il/home/feyaron/microscope/scanningless.pdf>. 50, 51
- Y. Otsu, V. Bormuth, J. Wong, B. Mathieu, G. P. Dugue, A. Feltz, and S. Dieudonne. Optical monitoring of neuronal activity at high frame rate with a digital random-access multiphoton (RAMP) microscope. *J. Neurosci. Methods*, 173:259–270, Aug. 2008. URL [http://cnp.igc.gulbenkian.pt/\\_media/research/mainen/ghyomm/otsu\\_2008.pdf](http://cnp.igc.gulbenkian.pt/_media/research/mainen/ghyomm/otsu_2008.pdf). 46
- E. Papagiakoumou, F. Anselmi, A. Begue, V. de Sars, J. Gluckstad, E. Y. Isacoff, and V. Emiliani. Scanless two-photon excitation of channelrhodopsin-2. *Nat. Methods*, 7:848–854, Oct. 2010. 53
- J. B. Pawley. More Than You Ever Really Wanted to Know About Charge-Coupled Devices. In J. B. Pawley, editor, *Handbook of biological confocal microscopy*, chapter Appendix 3, pages 918–931. Springer, third edition, 2006. 31, 33
- D. L. Pettit, S. S. Wang, K. R. Gee, G. J. Augustine, and N. Carolina. Chemical Two-Photon Uncaging: a Novel Approach to Mapping Glutamate Receptors. *Neuron*, 19:465–471, 1997. 13
- V. Praitis, E. Casey, D. Collar, and J. Austin. Creation of low-copy integrated transgenic lines in *Caenorhabditis elegans*. *Genetics*, 157(3):1217–26, Mar. 2001. ISSN 0016-6731. URL <http://www.pubmedcentral.nih.gov/articlerender.fcgi?artid=1461581&tool=pmcentrez&rendertype=abstract>. 14
- W. H. Press, S. A. Teukolsky, W. T. Vetterling, and B. P. Flannery. *Numerical Recipes in C*. Cambridge University Press, Cambridge, second edition, 1997. ISBN 0521431085. 87

## Bibliography

- D. G. Reddy, K. Kelleher, R. Fink, and P. Saggau. Three-dimensional random access multiphoton microscopy for functional imaging of neuronal activity. *Nat. Neurosci.*, 11:713–720, June 2008. URL <http://www.ncbi.nlm.nih.gov/pmc/articles/PMC2747788/pdf/nihms129126.pdf>. 46
- C. Rhodes. SBCL: A Sanely-Bootstrappable Common Lisp. In R. Hirschfeld and K. Rose, editors, *Self-Sustaining Systems*, pages 74–86. Springer Berlin / Heidelberg, 2008. 5
- M. S. Robbins, S. Member, and B. J. Hadwen. The Noise Performance of Electron Multiplying Charge-Coupled Devices. *IEEE Transactions on Electron Devices*, 50(5):1227–1232, 2003. 34
- P. J. Rodrigo, D. Palima, and J. Glückstad. Accurate quantitative phase imaging using generalized phase contrast. *Optics Express*, 16:2740–2751, 2008. URL <http://www.opticsinfobase.org/abstract.cfm?URI=oe-16-4-2740>. 52
- F. Rückerl, M. Kielhorn, J.-y. Tinevez, J. Heber, R. Heintzmann, and S. Shorte. Micro mirror arrays as high-resolution , spatial light modulators for photoactivation and optogenetics. In *SPIE*, volume 8586, 2013. 101
- A. Santella, Z. Du, S. Nowotschin, A.-K. A. Hadjantonakis, and Z. Bao. A hybrid blob-slice model for accurate and efficient detection of fluorescence labeled nuclei in 3D. *BMC bioinformatics*, 11(1):580, 2010. ISSN 1471-2105. doi: 10.1186/1471-2105-11-580. URL <http://www.biomedcentral.com/1471-2105/11/580>. 4, 60
- P. A. Santi. Light Sheet Fluorescence Microscopy. *Journal of Histochemistry and Cytochemistry*, 59:129–138, 2011. doi: doi:10.1369/0022155410394857. 40
- M. Sauer, J. Hofkens, and Joerg Enderlein. *Handbook of Fluorescence Spectroscopy and Imaging*. Wiley-VCH, Weinheim, 2011. ISBN 978-3-527-31669-4. 18, 20
- J. Schindelin, I. Arganda-carreras, E. Frise, V. Kaynig, M. Longair, T. Pietzsch, S. Preibisch, C. Rueden, S. Saalfeld, B. Schmid, J.-y. Tinevez, D. J. White, V. Hartenstein, K. Eliceiri, P. Tomancak, and A. Cardona. Fiji: an open-source platform for biological-image analysis. *Nature Methods*, 9(7), 2012. doi: 10.1038/nmeth.2019. 5
- J. U. Schmidt, M. Bring, J. Heber, M. Friedrichs, D. Rudloff, J. Rossler, D. Berndt, H. Neumann, W. Kluge, M. Eckert, M. List, M. Mueller, and M. Wagner. Technology development of diffractive micromirror arrays for the deep ultraviolet to the

## Bibliography

- near-infrared spectral range. In H. Thienpont, P. V. Daele, J. Mohr, and H. Zappe, editors, *MICRO-OPTICS 2010*, volume 7716 of *Proceedings of SPIE-The International Society for Optical Engineering*, 2010. ISBN 978-0-8194-8189-4. doi: 10.1117/12.855750. 67
- C. J. R. Sheppard, X. Gan, M. Gu, and M. Roy. Signal-to-Noise Ratio in Confocal Microscopy. In J. B. Pawley, editor, *Handbook of biological confocal microscopy*, chapter 22, pages 442–452. Springer, third edition, 2006. 34
- H. Siedentopf and R. Zsigmondy. Über Sichtbarmachung und Größenbestimmung ultramikroskopischer Teilchen, mit besonderer Anwendung auf Goldrubingläser. *Annalen der Physik*, 315:1–39, 1903. doi: DOI:10.1002/andp.19023150102. URL <http://onlinelibrary.wiley.com/doi/10.1002/andp.19023150102/abstract>. 40, 54
- W. J. Smith. *Modern optical engineering*. McGraw-Hill, 3 edition, 2000. ISBN 0-07-136360-2. 89
- T. Stiernagle. Maintenance of *C. elegans*. In C. e. R. Community, editor, *WormBook*, number 1999, pages 1–11. Jan. 2006. doi: 10.1895/wormbook.1.101.1. URL <http://www.ncbi.nlm.nih.gov/pubmed/18050451>. 14
- P. Stokseth. Properties of a defocused optical system. *JOSA*, 1002(1957):1314–1321, 1969. URL <http://www.opticsinfobase.org/abstract.cfm?&id=53819>. 55
- N. Streibl. Depth transfer by an imaging system. *Journal of Modern Optics*, 31(11): 1233–1241, 1984. URL <http://www.tandfonline.com/doi/abs/10.1080/713821435.27>
- J. E. Sulston and H. R. Horvitz. Post-embryonic cell lineages of the nematode, *Caenorhabditis elegans*. *Developmental biology*, 56(1):110–56, Mar. 1977. ISSN 0012-1606. URL <http://www.ncbi.nlm.nih.gov/pubmed/838129>. 14
- J.-Y. Tinevez, J. Dragavon, L. Baba-Aissa, P. Roux, E. Perret, A. Canivet, V. Galy, and S. Shorte. *A quantitative method for measuring phototoxicity of a live cell imaging microscope.*, volume 506. Elsevier Inc., 1 edition, Jan. 2012. ISBN 9780123918567. doi: 10.1016/B978-0-12-391856-7.00039-1. URL <http://www.ncbi.nlm.nih.gov/pubmed/22341230>. 14, 16
- M. Tokunaga, N. Imamoto, and K. Sakata-Sogawa. Highly inclined thin illumination enables clear single-molecule imaging in cells. *Nature Methods*, 5(2):159–161, Feb. 2008. ISSN 1548-7091. doi: 10.1038/NMETH.

## Bibliography

1171. URL <http://www.ncbi.nlm.nih.gov/pubmed/18176568>[http://www.riken.jp/ExtremePhotonics/realtime/s\\_no2.pdf](http://www.riken.jp/ExtremePhotonics/realtime/s_no2.pdf). 42, 43, 61
- S. van de Linde. *Photoswitching of organic dyes and single molecule based super resolution imaging*. PhD thesis, Bielefeld, 2011. URL <http://pub.uni-bielefeld.de/publication/2436869>. 19
- S. Vembu. Fourier transformation of the n-dimensional radial delta function. *Quart. J. Math. Oxford (2)*, 12(September 1960):165–168, 1961. 124
- C. Ventalon and J. Mertz. Quasi-confocal fluorescence sectioning with dynamic speckle illumination. *Optics letters*, 30(24):3350–3352, 2005. URL <http://www.opticsinfobase.org/abstract.cfm?id=86570>. 83
- C. Ventalon, R. Heintzmann, and J. Mertz. Dynamic speckle illumination microscopy with wavelet prefiltering. *Optics letters*, 32(11):1417–1419, 2007. URL <http://www.opticsinfobase.org/abstract.cfm?id=133456>. 83
- P. J. Verveer, Q. S. Hanley, P. W. Verbeek, L. J. van Vliet, and T. M. Jovin. Theory of confocal fluorescence imaging in the programmable array microscope (PAM). *Journal of Microscopy*, 189(March):192–198, 1998. 48
- J. Vogelsang, R. Kasper, C. Steinhauer, B. Person, M. Heilemann, M. Sauer, and P. Tinnefeld. A Reducing and Oxidizing System Minimizes Photobleaching and Blinking of Fluorescent Dyes. *Angew. Chem. Int. Ed.*, 47, 2008. doi: 10.1002/anie.200801518. 20
- A. H. Voie, D. H. Burns, and F. A. Spelman. Orthogonal-plane fluorescence optical sectioning: three-dimensional imaging of macroscopic biological specimens. *Journal of Microscopy*, 1993. 40
- P. Vu, B. Fowler, S. Mims, C. Liu, J. Balicki, and H. Do. Low Noise High Dynamic Range 2.3 Mpixel CMOS Image Sensor Capable of 100Hz Frame Rate at Full HD Resolution. *imagesensors.org*, pages 3–6, 2011. URL [http://www.imagesensors.org/PastWorkshops/2011Workshop/2011Papers/P35\\_Fowler\\_HDR.pdf](http://www.imagesensors.org/PastWorkshops/2011Workshop/2011Papers/P35_Fowler_HDR.pdf). 36
- Wireshark.org. Wireshark, a network protocol analyzer 1.7.1., 2012. URL <http://www.wireshark.org/>. 5
- M. Zahid, M. Vélez-Fort, E. Papagiakoumou, C. Ventalon, M. C. Angulo, and V. Emiliani. Holographic Photolysis for Multiple Cell Stimulation in Mouse

## Bibliography

- Hippocampal Slices. *PLoS ONE*, 5(2):e9431, 2010. doi: 10.1371/journal.pone.0009431. URL <http://dx.doi.org/10.1371/journal.pone.0009431>. 51
- Z. Zhang and M. Levoy. Wigner distributions and how they relate to the light field. In *Computational Photography (ICCP), 2009 IEEE International Conference on*, pages 1–10, Apr. 2009. doi: 10.1109/ICCPHOT.2009.5559007. 49